AD-A122 393 AERODYNAMIC EFFECTS ON AIRBORNE OPTICAL SYSTEMS(U) 1/2
MCDONNELL AIRCRAFT CO ST LOUIS MO D J WOLTERS
14 DEC 73 MDC-A2582
UNCLASSIFIED F/G 20/6 NL

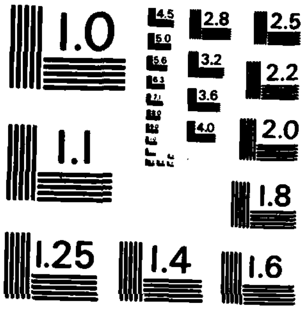

MICROCOPY RESOLUTION TEST CHART
NATIONAL BUREAU OF STANDARDS-1963-A

Defense Logistics Agency

DISTRIBUTION STATEMENT A
Approved for public release;
Distribution Unlimited

MCDONNELL DOUGLAS
CORPORATION

82 12 13 003

REPORT MDC A2582
14 DECEMBER 1973
COPY NO. 92

②

AERODYNAMIC EFFECTS ON AIRBORNE OPTICAL SYSTEMS

PREPARED BY

D.J. WOLTERS
ELECTRONIC SYSTEMS TECHNOLOGY

MCDONNELL AIRCRAFT COMPANY
Box 516, Saint Louis, Missouri 63166 · Tel. (314)232-0232

MCDONNELL DOUGLAS
CORPORATION

ACKNOWLEDGEMENTS

The author wishes to express his thanks to Ralph Fisher, Ron LaVallee of the Advanced Systems Concepts group, and Sterling Littlepage of the Advanced Design group, Aerodynamics Department whose interest prompted the aerodynamic effects study. Special acknowledgement is due Ralph Fisher for his help in all phases of the study. The author also wishes to thank Donald Groening of the Air Force Avionics Laboratory for providing test data from the RF-4C wind tunnel experiment and Dr. Dennis Kelsall of the Lincoln Laboratory, Massachusetts Institute of Technology for providing information on his work with shearing interferometers.

[Typist: If abstract is too [illegible] leave – chopped at the [illegible]]

REPORT MDC A2582
14 DECEMBER 1973

Abstract

micron

A first-order determination of the effects of boundary flow of high-speed aircraft on the transmission of 0.2μ to 20μ radiation is presented. The four types of boundary flow considered are: main flow, shock wave, turbulent boundary layer (TBL), and separated flow. The potential-flow velocity field provides a means for computing wavefront aberation caused by curved density contours in the main-flow region. An example problem is worked out for a collimated beam emerging from a sphere. The density jump across a shock wave generally causes both beam refraction and beam degradation. The special case of refraction by a plane shock wave is computed. Estimates of the average modulation transfer function (MTF) for the TBL and separated flow are made from experimental data. From the wavefront aberation of main flow and the average MTF's for the TBL and separated flow, the effect of boundary flow on both propagating and imaging systems is analyzed. The effect is presented in terms of power density at the focus point for propagating systems and in terms of resolution for imaging systems. The effect of shock waves is not considered in the analysis because the only quantitative work in that area concerns beam direction only, not beam quality. In general boundary flow has only a slight effect on long wavelength (10.6μ) radiation. The only exception is the effect of main flow at low altitude in which case power density at focus may drop to less than one percent of the diffraction limit. A similar power loss may be caused by both main flow and separated flow when the wavelength is short (0.55μ). Only the TBL effect is not drastic. Finally, the scaling rules for predicting boundary-flow optical effects of a body from a similar body of different scale is derived. Adjustment of wavelength and/or density is required to compensate for the change in scale.

TABLE OF CONTENTS

TABLE OF CONTENTS (CONTINUED)

TABLE OF CONTENTS (CONTINUED)

List of Pages

Title Page
ii to ix
1 to 140

LIST OF FIGURES

LIST OF FIGURES (CONTINUED)

LIST OF FIGURES (CONTINUED)

I. Introduction

The quality of an optical beam which passes through the boundary flow of a transonic or supersonic aircraft can be drastically reduced. Camera resolution dropped from 164 lines/mm to 30 lines/mm in a wind tunnel test of the RF-4C aircraft.[1] When a lower acuity system was flight tested in the RF-4C, resolution dropped from 35 lines/mm to 20 lines/mm.[2] The reason for the resolution loss was that the optical path from the target passed through a separated flow region behind the nose chin as shown in Figure 1. Density fluctuations in this region caused random wavefront errors, and resolution was thus reduced. When the aircraft nose was refaired, the resolution loses did not occur.[3,4] Random density fluctuations are not the only source of aerodynamically induced optical degradation. It will be shown that the curved air density contours in the main flow region of a blunt body, as shown in Figure 2, produce wavefront aberrations which, if uncorrected, may completely destroy the optical quality of an incoming or propagated beam.

These examples show that an understanding of boundary flow effects is necessary if airborne optical systems are to achieve optimal results.

Purpose of this Report

The purpose of this report is to present a first-order determination of the effects of boundary flow on the transmission of 0.2μ to 20μ radiation. This approach establishes the significance of the aerodynamic effect and hopefully will lead to more rigorous analytical and experimental studies.

Types of Boundary Flow

Boundary flow may be divided into two classes, random and controlled. In addition to separated flow, random flow includes the turbulent boundary layer (TBL), which forms on the skin of all aircraft. The TBL causes a degradation similar to, but weaker than that caused by separated flow. Stine and Winovich have shown that TBL's as thin as one inch may cause significant degradation.[5] Unlike the random flow, controlled flow has density gradients which are constant in time. Also wavefront deviations caused by controlled flow generally have a larger spatial scale than those caused by random flow as shown in Figure 3. Both main flow and shock waves are types of controlled flow. The shock wave occurs whenever some part of the flow field outside an aircraft has a speed greater than the speed of sound relative to the aircraft. The shock wave is a very thin pressure jump and therefore a very thin density jump. In the simplest kind of wavefront deviation, the shock wave is a plane interface between media of different refractive indices, and a beam passing through the shock will behave according to Snell's law as shown in Figure 4. All four types of boundary flow (separated flow, TBL, main flow, and shock wave) are shown in Figure 5 for an RF-4C at Mach .93.

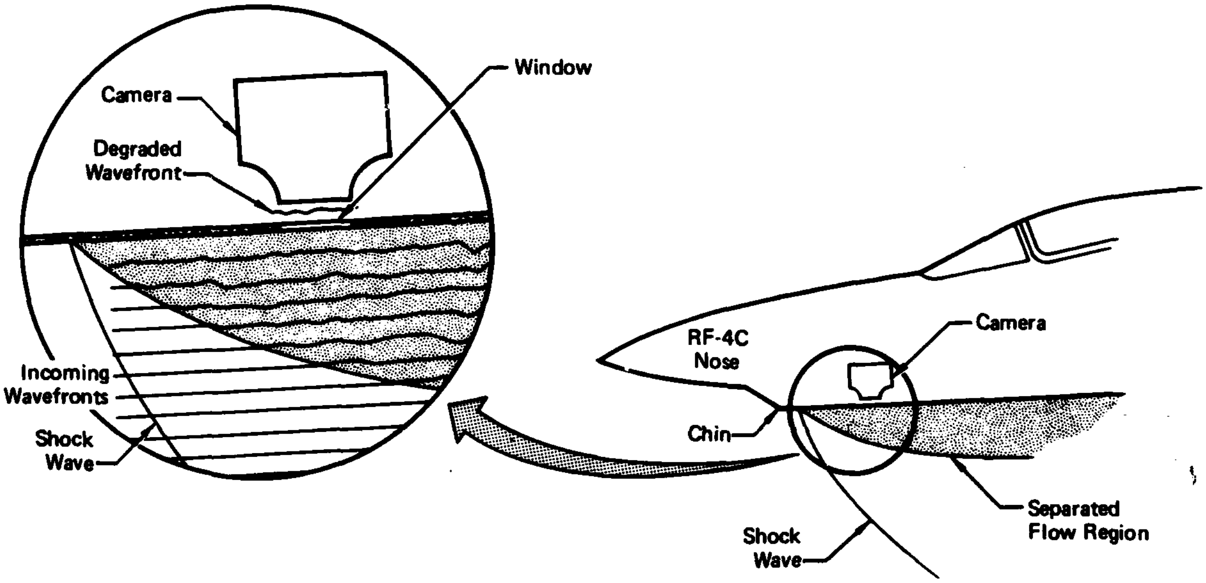

FIGURE 1
WAVEFRONT DEGRADATION CAUSED BY FLOW SEPARATION
BEHIND RF-4C NOSE CHIN

GP74-0200-1

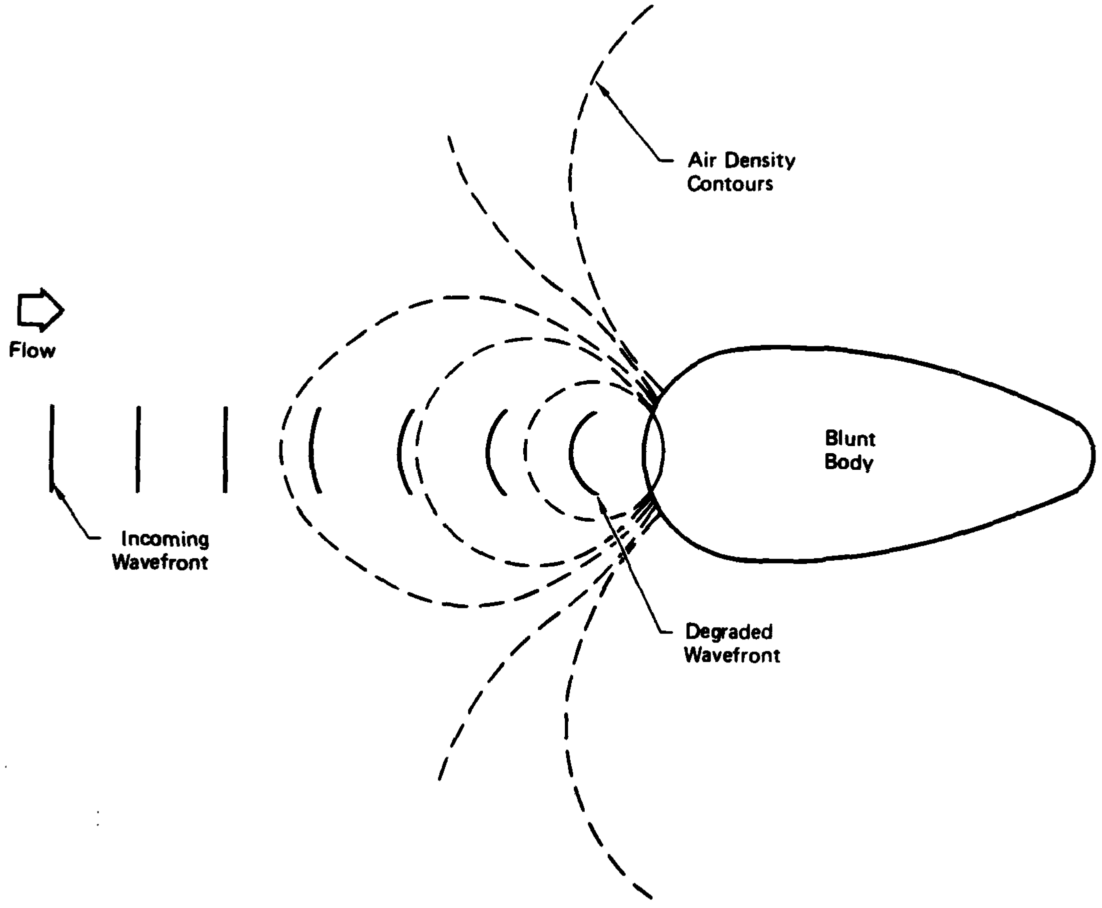

GP74-0200-2

FIGURE 2
WAVEFRONT DEGRADATION CAUSED BY CURVED AIR-DENSITY CONTOURS IN THE MAIN-FLOW REGION OF A BLUNT BODY

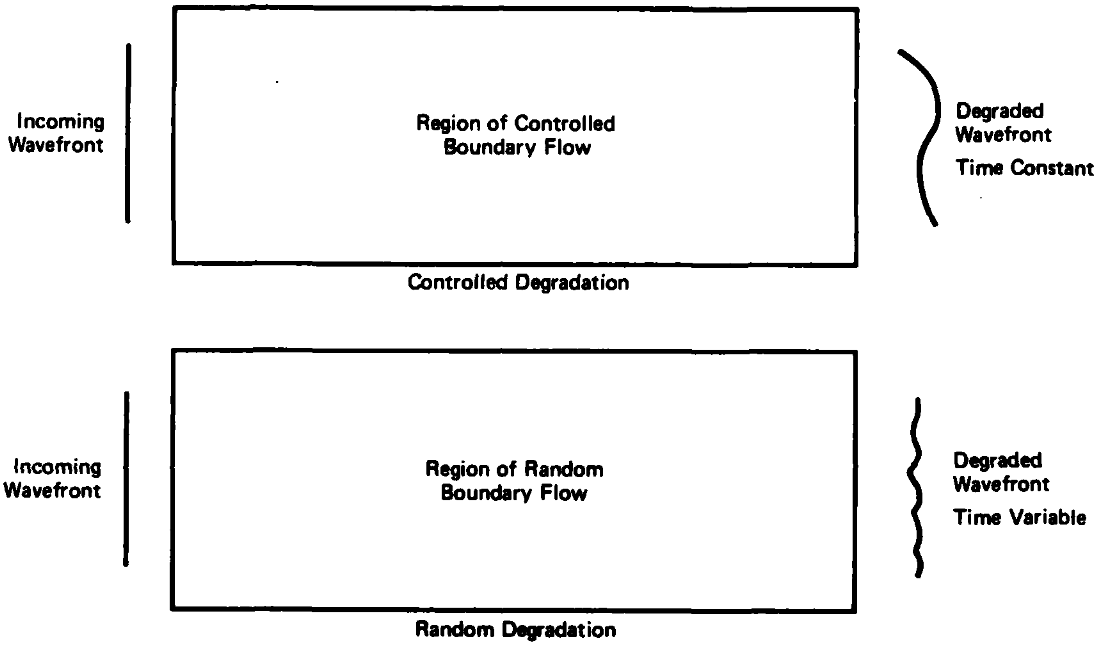

FIGURE 3
COMPARISON OF CONTROLLED- AND RANDOM-WAVEFRONT DEGRADATION

GP74-0200-3

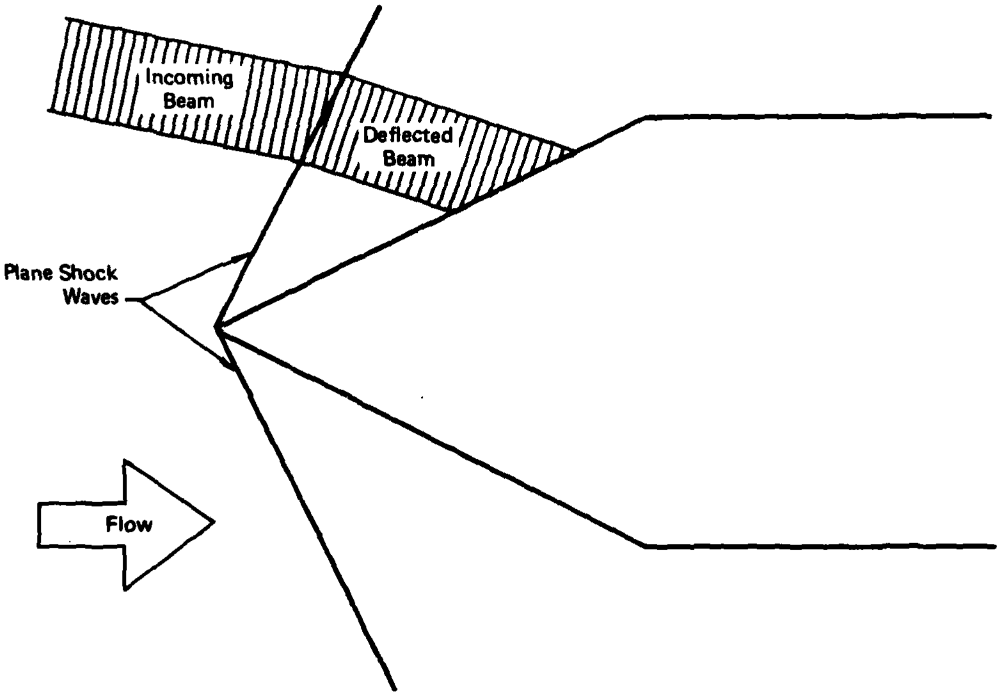

FIGURE 4
OPTICAL EFFECT OF A PLANE SHOCK WAVE

GP74-0200-4

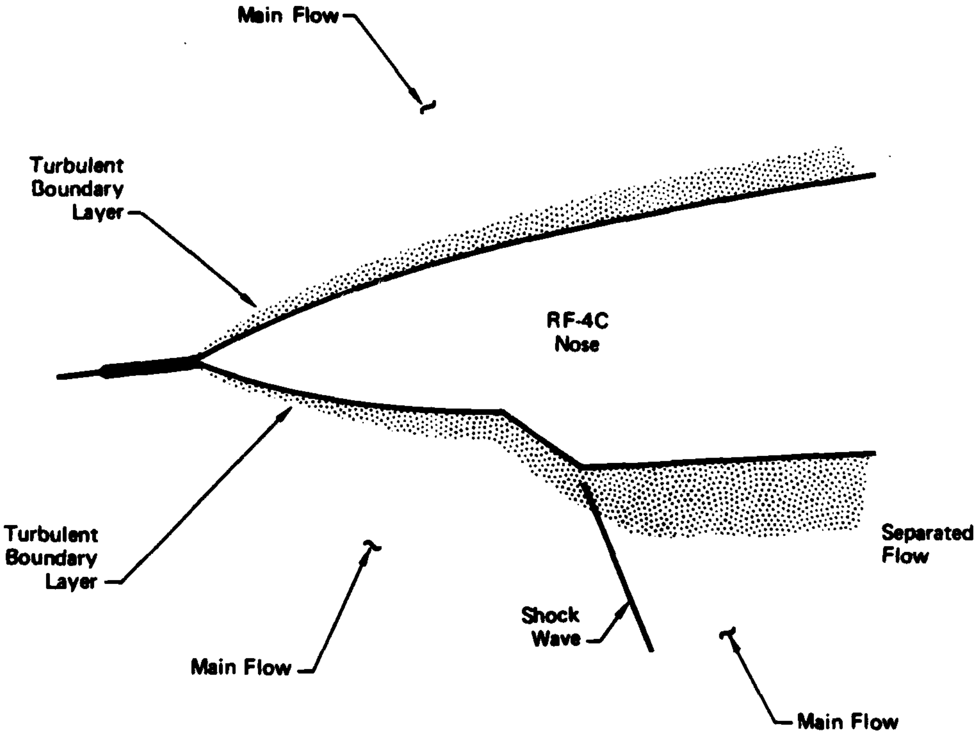

FIGURE 5
POSITIONS OF MAIN FLOW, SHOCK WAVE, TURBULENT BOUNDARY LAYER, AND SEPARATED FLOW FOR AN RF-4C AT MACH 0.93

Summary

This report considers the optical effects of the four types of boundary flow: main flow, shock wave, TBL, and separated flow. The next section presents the basic aerodynamics and optics theory used in the rest of the report.

Controlled wavefront deviations are discussed in Section III. Wavefront aberration cuased by curved density contours in the main-flow region are computed from the potential-flow velocity field. An example problem is worked out for a collimated beam emerging from a sphere. This section also includes a qualitative description of degradation caused by shock waves. The special case of refraction by a plane shock wave is computed.

In Section IV the Stine-Winovich experiment data and the RF-4C wind tunnel data are used to estimate average modulation transfer functions (MTF's) for TBL's and separated flow respectively. A recent experiment by Kelsall is also described.[6] Although several complications make it impossible to properly analyze the resultant data, this experiment is important because the average boundary flow MTF was measured directly using a shearing interferometer. Hopefully this new technique, which produces more reliable MTF measurements than any other method, will be used in controlled experiments to measure boundary flow MTF's.

From the results of the previous sections, Section V analyzes the optical effect of boundary flow on both propagating and imaging systems. The effect is presented in terms of power density at the focus point for propagating systems and in terms of resolution for imaging systems. In addition to main flow, turbulent boundary layers, and separated flow, wake flow is also considered. Wake flow is simply separated flow which occurs behind a blunt body as shown in Figure 6. In Section V wake flow is treated as a special case of separated flow. Shock waves are not considered because the only quantitative work done in that area concerns beam direction only, not beam quality. Finally, Section V derives the scaling rules for predicting boundary-flow optical effects of a body from a similar body of different scale.

Notation, Symbols, and Important Equations

Appendix A contains a summary of important equations as well as a list of notations and symbols.

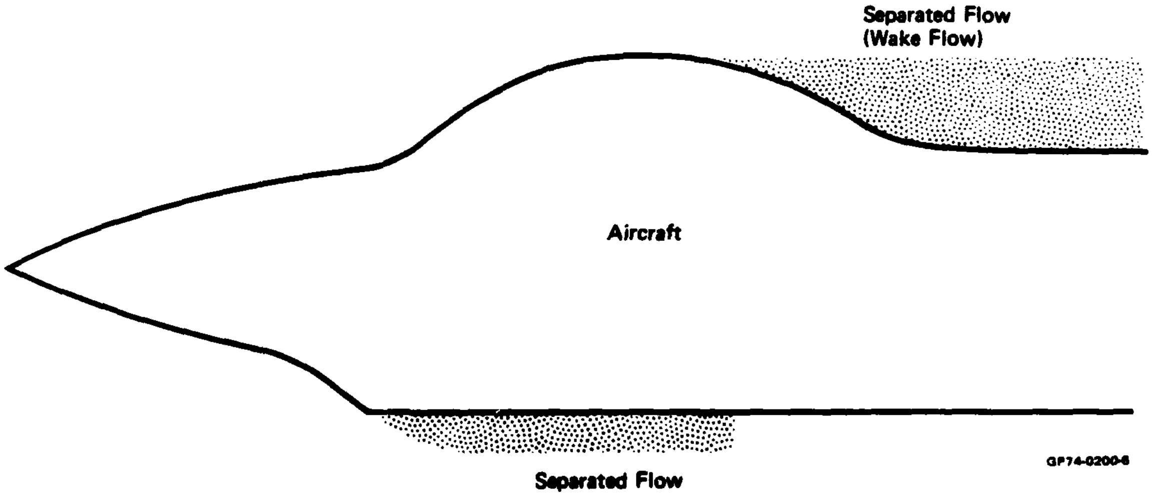

FIGURE 6
WAKE FLOW AS A SPECIAL CASE OF SEPARATED FLOW

II. Basic Theory

The purpose of this section is to present the basic aerodynamic and optics theory used in the rest of the report. The topics discussed here are the relationship between refractive index and density for air, the optical phase, the optical transfer function (OTF), power density in the focal plane, and the aerodynamic similarity rules.

Relationship Between Refractive Index and Density for Air

Because the refractive index n of air is very close to unity, it is convenient to define the refractive modulus

$$N = (n-1) \times 10^6. \tag{2-1}$$

At normal temperatures and pressures N is of the order of 300. A formula which gives N to within ± 1 for dry air in the 0.2μ to 20μ wavelength region is

$$N = 0.776 \frac{P}{T} \left(1 + \frac{7.52 \times 10^{-15}}{\lambda^2}\right) \tag{2-2}$$

where

P = pressure in nt/m^2
T = temperature in °K
λ = wavelength in meters.[7]

A correction factor for water vapor, which may subtract as much as 3 from N, is given by

$$- 0.6 \times 10^{-3} P_{wv}$$

where P_{wv} is the water vapor pressure in nt/m^2. For the accuracy required in this paper, however, the correction factor will not be required. Using the perfect gas law,

$$P = 287 \rho T \tag{2-3}$$

where ρ is density in kg/m^3, Equation (2-2) may be written

$$N = 223 \rho \left(1 + \frac{7.52 \times 10^{-15}}{\lambda^2}\right) \tag{2-4}$$

The refractive index may now be written

$$n = 1 + K\rho \tag{2-5}$$

where the Gladstone-Dale constant K is given by

$$K = 0.223 \times 10^{-3} \left(1 + \frac{7.52 \times 10^{-15}}{\lambda 2}\right) \text{m}^3/\text{kg}. \tag{2-6}$$

The wavelength term is negligible for wavelengths longer than 10μ so that

$$K = 0.223 \times 10^{-3}\ m^3/kg \qquad (2\text{-}7)$$

for long wavelengths. Even for shorter wavelengths, the wavelength term may have little effect; for example, when $\lambda = 0.55\mu$ K increases to only 0.228×10^{-3} m^3/kg. For most purposes, therefore, Equations (2-5) and (2-7) may be used to calculate n. Otherwise Equations (2-5) and (2-6) may be used.

Optical Phase

For our purposes we may represent a general optical wave as a scalar given by

$$F(x,y,z,t) = A(x,y,z,t)\ \exp\{-i[\omega t - k\Delta(x,y,z,t)]\} \qquad (2\text{-}8)$$

where

x,y,z = Cartesian coordinates in space
t = time
F = wave function (generally complex)
A = wave amplitude (generally complex)
Δ = wave phase
ω = angular frequency $(2\pi c/\lambda)$
k = wave number $(2\pi/\lambda)$
c = speed of light
λ = optical wavelength.

The function F gives a complete description of the optical wave in space and time. In this subsection we will show that for our case the quotient Δ/λ completely describes the optical wave. The relationship between Δ and the refractive index n of the medium is given. Finally, it will be shown that Δ and the wavefront W are equal in magnitude and opposite in sign.

First Equation (2-8) is simplified. Since our medium is not lossy and since the wavefront is essentially plane, not spherical, A is a constant. The term

$$e^{-iwt}$$

in Equation (2-8) is left to be understood. The time dependence of Δ is also left to be understood, and Equation (2-8) becomes

$$F(x,y,z) = Ae^{ik\Delta(x,y,z)} \qquad (2\text{-}9)$$

This equation shows that at a fixed time and amplitude F depends on Δ/λ only.

Let us examine a beam which traverses a medium of varying refractive index. A plane parallel, monochromatic beam emerges from the $x'y'$-plane of a Cartesian coordinate system with its direction of propagation parallel to the z'-axis as shown in Figure 7. At some distance $L >> \lambda$ from the $x'y'$-plane we examine the wave.

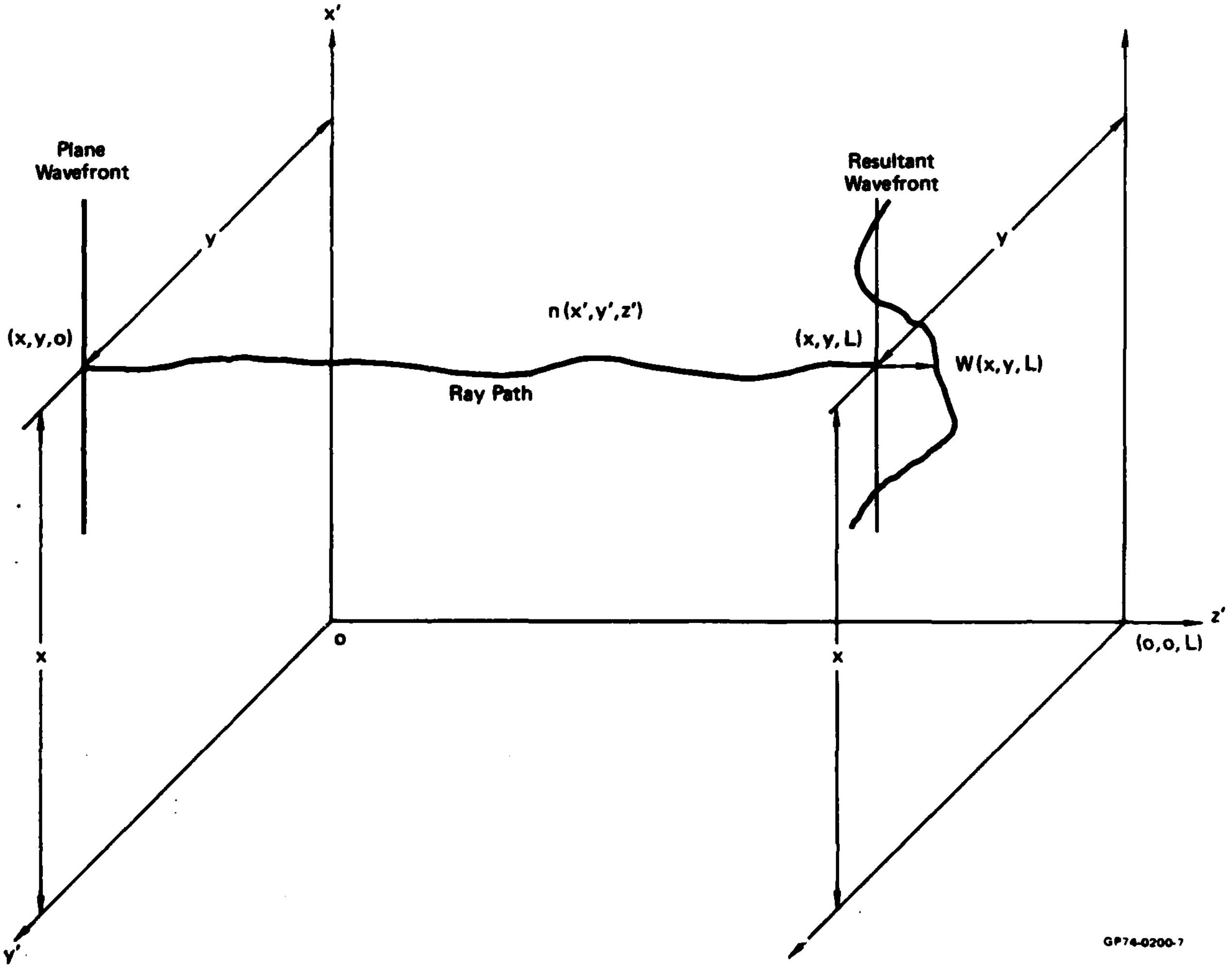

FIGURE 7
BEAM TRAVERSING MEDIUM OF VARYING REFRACTIVE INDEX

$$F(x,y,L) = Ae^{ik\Delta(x,y,L)} \tag{2-10}$$

The phase is found by integrating the refractive index n over the optical path.

The phase is given by

$$\Delta(x,y,L) = \int_{(x,y,0)}^{(x,y,L)} n(x',y',z')\, ds \pm m\,\lambda \tag{2-11}$$

where ds is an increment along the ray path from (x,y,0) to (x,y,L) and m is any convenient integer. For the boundary flow problem the refractive index changes are small, so the ray path will be very close to parallel to the z′-axis. The variations of the ray from the z′-axis in Figure 7 are greatly exagerated.

$$ds = dz' \tag{2-12}$$

and

$$\Delta(x,y,L) = \int_0^L n(x,y,z')\, dz' \pm m\,\lambda. \tag{2-13}$$

We now look at the wavefront W(x,y,L) at z′ = L as shown in Figure 7. It is defined by specifying that the phase at the wavefront is equal to some arbitrary constant.

$$\Delta[x,y,W(x,y,L)] = \text{const} = \int_0^{W(x,y,L)} n(x,y,z')\, dz' \pm m\,\lambda \tag{2-14}$$

or

$$\text{const} = \int_0^L n(x,y,z')\, dz' \pm m\,\lambda + \int_L^{W(x,y,L)} n(x,y,z')\, dz' \tag{2-15}$$

Using Equation (2-13) and the fact that n is constant over distances of several wavelengths, Equation (2-15) becomes

$$\text{const} = \Delta(x,y,L) + n(x,y,L)\, W(x,y,L) \tag{2-16}$$

Choosing zero for the value of the arbitrary constant and noting that n is very close to unity, we have

$$W(x,y,L) = -\Delta(x,y,L). \tag{2-17}$$

Equation (2-17) shows that Δ and W have the same magnitude but opposite signs.

Optical Transfer Function

In the case of turbulent boundary layers and separated flow, Δ is a random variable which in practice cannot be measured. However, the average OTF, which is a function of Δ, can often be measured or computed.

Definition. If in Figure 7 a perfect lens is placed perpendicular to the z'-axis at $z' = L$, an image is formed in the focal plane. A screen with an aperture Σ is placed adjacent to the lens as shown in Figure 8 so that all light passing through the aperture must also pass through the lens. The pupil function G is defined in terms of the wave F at the aperture as follows.

$$G(x,y) = \begin{cases} F(x,y) = Ae^{ik\Delta(x,y)}, & (x,y)\in\Sigma \\ 0, & (x,y)\notin\Sigma \end{cases} \tag{2-18}$$

In words, the pupil function G is identical to the wave function F inside the aperture but vanishes outside the aperture. The dependence of F and Δ on L is left to be understood. The wave amplitude U in the focal plane is the inverse Fourier transform of G,

$$U(X,Y) = \frac{1}{\lambda f}\iint_{-\infty}^{\infty} G(x,y)\ \exp\left[\frac{-ik}{f}(xX + yY)\right] dx\ dy \tag{2-19}$$

where X and Y are the coordinates in the focal plane and f is the focal length. The image irradiance I is then given by

$$I(X,Y) = U^*(X,Y)\ U(X,Y). \tag{2-20}$$

The asterisk denotes complex conjugate. The optical transfer function τ of the wave passing through the aperture is defined to be the normalized Fourier transform of I,

$$\tau\left(\frac{x}{\lambda f},\frac{y}{\lambda f}\right) = \frac{1}{C}\iint_{-\infty}^{\infty} I(X,Y)\ \exp\left[\frac{ik}{f}(xX + yY)\right] dX\ dY \tag{2-21}$$

where

$$C = \iint_{-\infty}^{\infty} I(X,Y)\ dX\ dY \tag{2-22}$$

Using Parseval's theorem from Fourier analysis in conjunction with Equations (2-19), (2-20), and (2-22) we have

$$C = \iint_{-\infty}^{\infty} U^*(X,Y)\ U(X,Y)\ dX\ dY = \iint_{-\infty}^{\infty} G^*(x,y)\ G(x,y)\ dx\ dy \tag{2-23}$$

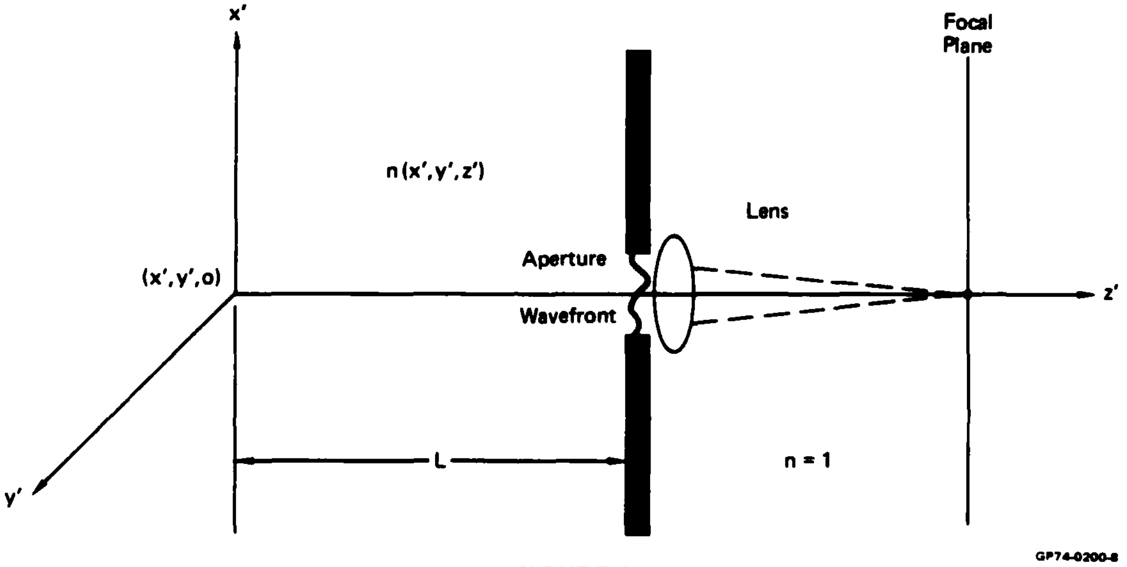

FIGURE 8
GEOMETRY FOR DEFINING OPTICAL TRANSFER FUNCTION

or using Equation (2-18), we have

$$C = A^* A \Sigma . \tag{2-24}$$

Equations (2-22) through (2-24) each imply that C is the radiant power which passes through the aperture and lens to the focal plane.

The spatial frequencies defined by

$$\nu_x = \frac{x}{\lambda f} \text{ and } \nu_y = \frac{y}{\lambda f} \tag{2-25}$$

allow Equation (2-21) to be written

$$\tau\left(\nu_x, \nu_y\right) = \frac{1}{C} \iint_{-\infty}^{\infty} I(X,Y) \exp\left[i2\pi\left(X\nu_x + Y\nu_y\right)\right] dX\, dY . \tag{2-26}$$

The quantities ν_x and ν_y have units of cycles per unit distance. Since τ is the Fourier transform of a real function, it is Hermition; the real part of τ is an even function, and the imaginary part is odd. If I is even, τ is real. The MTF can now be defined simply as the absolute value of the OTF.

<u>Autocorrelation</u> <u>Function</u> <u>of</u> <u>Pupil</u> <u>Function</u>. Although the OTF is defined by Equation (2-21), it is often convenient to express τ as a function of the pupil function rather than the focal plane intensity. Specifically, it can be shown that the OTF is equal to the normalized autocorrelation function of the pupil function by using a theorem from Fourier analysis,[8]

$$\tau\left(\frac{x}{\lambda f}, \frac{y}{\lambda f}\right) = \frac{1}{C} \iint_{-\infty}^{\infty} G^*(x', y')\, G(x'+x, y'+y)\, dx'dy' . \tag{2-27}$$

The OTF may be expressed in terms of Δ by using Equations (2-18) and (2-24),

$$\tau\left(\frac{x}{\lambda f}, \frac{y}{\lambda f}\right) = \frac{1}{\Sigma} \iint_{-\infty}^{\infty} G_0(x', y')\, G_0(x'+x, y'+y) \times \exp\{ik[\Delta(x'+x, y'+y) - \Delta(x', y')]\}\, dx'dy' \tag{2-28}$$

where

$$G_0(x,y) = \begin{cases} 1, & (x,y) \in \Sigma \\ 0, & (x,y) \notin \Sigma \end{cases} \tag{2-29}$$

<u>Diffraction</u> <u>OTF</u>. A special case occurs when the wave front entering the aperture is plane, in which case Δ is constant. Equation (2-28) becomes the diffraction-limit OTF (or MTF, since the OTF is real) of the aperture.

$$\tau_0\left(\frac{x}{\lambda f},\frac{y}{\lambda f}\right) = \frac{1}{\Sigma}\iint_{-\infty}^{\infty} G_0(x',y')\ G_0(x'+x,y'+y)\ dx'dy' \qquad (2\text{-}30)$$

Two aperture shapes which are often used are the rectangle and the circle. For a retangular aperture with dimensions $D_x \times D_y$ the pupil function is

$$G_0(x,y) = \begin{cases} 1, & 0 \le x \le D_x,\ 0 \le y \le Dy \\ 0 \text{ otherwise} \end{cases} \qquad (2\text{-}31)$$

and the diffraction OTF is

$$\tau_0\left(\frac{x}{\lambda f},\frac{y}{\lambda f}\right) = \begin{cases} \left(1 - \frac{|x|}{D_x}\right)\left(1 - \frac{|y|}{D_y}\right); & -D_x \le x \le D_x,\ -D_y \le y \le D_y \\ 0 \text{ otherwise} \end{cases} \qquad (2\text{-}32)$$

For a circular aperture of diameter D the pupil function is

$$G_0(r) = \begin{cases} 1, & 0 \le r \le D/2 \\ 0 \text{ otherwise} \end{cases} \qquad (2\text{-}34)$$

where

$$r = \sqrt{x^2 + y^2}. \qquad (2\text{-}34)$$

The diffraction OTF is

$$\tau_0\left(\frac{r}{\lambda f}\right) = \begin{cases} \frac{2}{\pi}\left[\cos^{-1}\left(\frac{r}{D}\right) - \left(\frac{r}{D}\right)\sqrt{1 - \left(\frac{r}{D}\right)^2}\right], & 0 < r < D \\ 0 \text{ otherwise} \end{cases} \qquad (2\text{-}35)$$

Figure 9 is a plot of the diffraction OTF's for rectangular and circular apertures. Notice that only positive spatial frequencies are used since all diffraction OTF's are even functions.

Examination of Equation (2-28) reveals that any aberation in the wavefront at the aperture can only serve to decrease the MTF below the diffraction value. That is

$$\left|\tau\left(\frac{x}{\lambda f},\frac{y}{\lambda f}\right)\right| \le \left|\tau_0\left(\frac{x}{\lambda f},\frac{y}{\lambda f}\right)\right|. \qquad (2\text{-}36)$$

A comparison of τ with τ_0 is often used as a measure of the seriousness of the aberation.

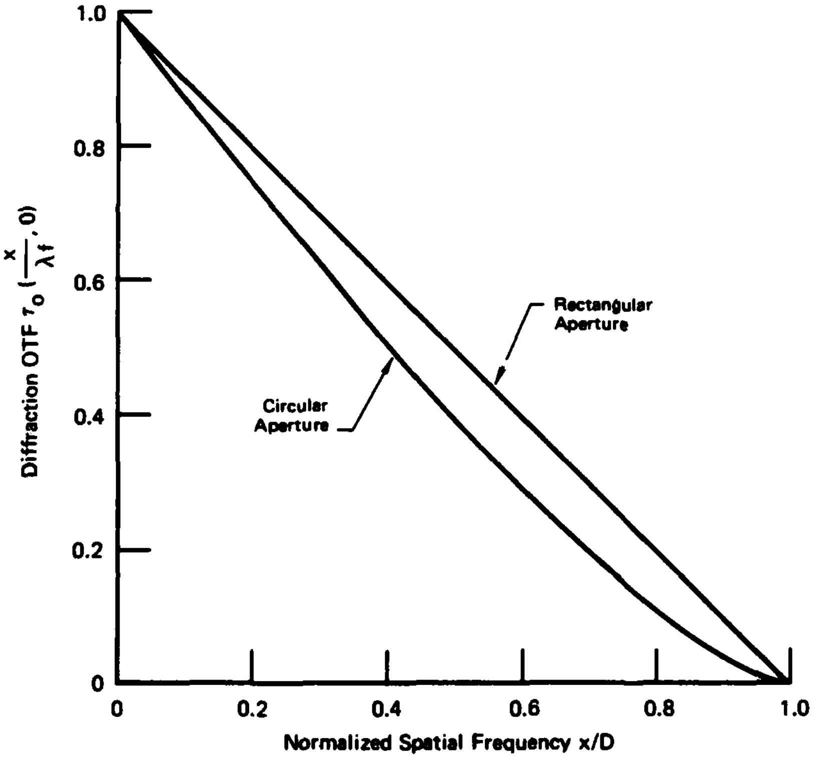

FIGURE 9
DIFFRACTION OTF FOR RECTANGULAR AND CIRCULAR APERTURES

GP74-0200-9

Sine-Wave Response Function. For an imaging system the MTF is the sine-wave response function of the system. Consider the imaging system geometry shown in Figure 10. An incremental area $dX'dY'$ located at (X',Y') in the object plane produces an image on the image plane. We assume that light from the object plane is incoherent, and for simplicity we assume that the magnification is unity. The radiant power reaching the image plane from our incremental area is proportional to $O(X',Y')\ dX'dY'$ where $O(X',Y')$ is the object radiance at (X',Y'). We now wish to find the resulting image irradiance at (X,Y). In defining the OTF, $I(X,Y)$ was the image irradiance resulting from a wave which, except for boundary flow effects, was plane at the lens aperture. We may also take $I(X,Y)$ as the image irradiance resulting from a point object far to the left of the lens. In this sense we now define the point spread function $p(X,Y)$ as the normalized image irradiance corresponding to a point object. The OTF is now taken as the Fourier transform of $p(X,Y)$. In the present context $I(X,Y)$ results, not from a point, but from a finite object. It is this image irradiance which we are trying to find. Since the incremental area may be considered a point, the incremental contribution to $I(X,Y)$ is

$$dI(X,Y) = O(X',Y')\ dX'dY'\ p(X-X',Y-Y'). \qquad (2\text{-}37)$$

We assume that $p(X,Y)$ is constant for object points throughout the object plane. $I(X,Y)$ is found by integrating Equation (2-37) over the object plane.

$$I(X,Y) = \iint_{-\infty}^{\infty} O(X',Y')\ p(X-X',Y-Y')\ dX'dY' \qquad (2\text{-}38)$$

The integral is called the convolution of O and p. By applying the convolution theorem from Fourier analysis to Equation (2-38) we have

$$S_i\left(\nu_x,\nu_y\right) = S_o\left(\nu_x,\nu_y\right)\ \tau\left(\nu_x,\nu_y\right) \qquad (2\text{-}39)$$

where S_i, S_o, and τ are the Fourier transforms of I, O, and p respectively. Equation (2-39) shows that the OTF is the spatial frequency response of the system.

We now let the object be a sinusoid of frequency ν,

$$O(X',Y') = C_0 \sin(2\pi\nu X' + \phi) + 1,\ 0 \le C_0 \le 1 \qquad (2\text{-}40$$

where ϕ is a phase factor and C_0 is a constant which we call the object modulation. Taking the Fourier transform we have

$$S_o\left(\nu_x,0\right) = C_0\ \delta\left(\nu_x - \nu\right) + \delta\left(\nu_x\right) \qquad (2\text{-}41)$$

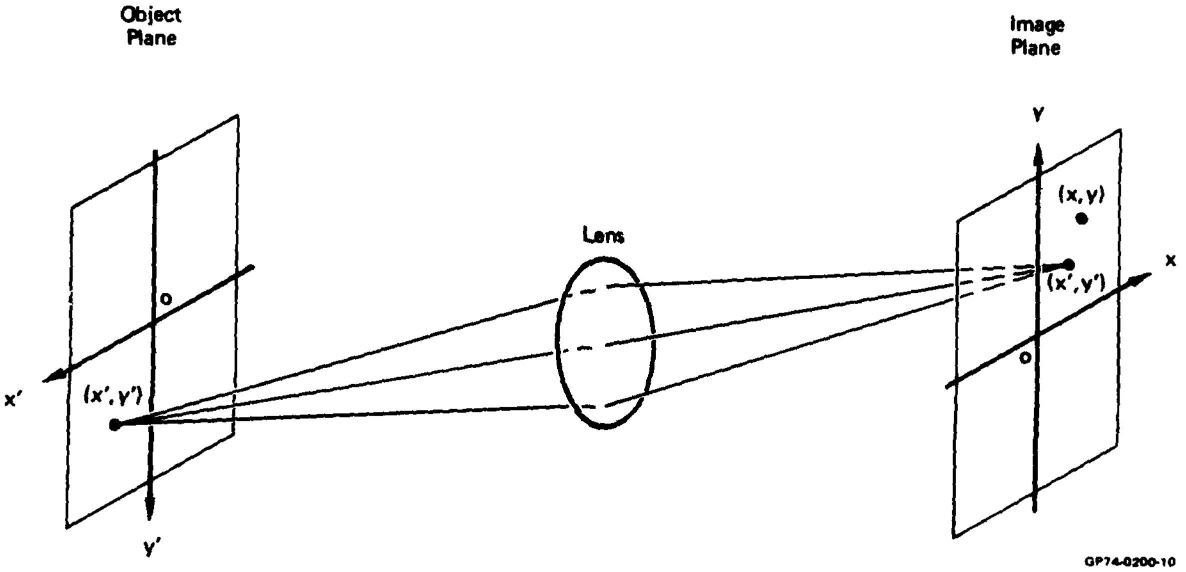

FIGURE 10
IMAGING SYSTEM GEOMETRY

where δ is the delta function. Substituting Equation (2-41) into Equation (2-39), we have

$$\begin{aligned} |S_i(\nu_x,0)| &= |\tau(\nu_x,0)|C_0\ \delta(\nu_x-\nu) + |\tau(\nu_x,0)|\delta(\nu_x) \\ &= |\tau(\nu,0)|C_0\delta(\nu_x-\nu) + \delta(\nu_x). \end{aligned} \tag{2-42}$$

This equation shows that the image of a sinusoid of frequency ν is also a sinusoid of frequency ν, the modulation of which is reduced by a factor of $|\tau(\nu,0)|$. In other words, the MTF is the sine-wave response function of an imaging system as illustrated in Figure 11.

Power Density in Focal Plane

Suppose a beam of light emerging from and aircraft is focussed at some distant point as shown in Figure 12. Diffraction and the boundary flow will cause the point image to be spread over the focal plane. In this type of problem the image irradiance or power density I(X,Y) is sought. The problem geometry here is somewhat different than that used earlier. Here the optical distrubance caused by boundary flow occurs between the lens and the focus point.

The mathematics developed for the geometry in which the lens is between the disturbance and the focus point is still valid, however, as long as the distance between the lens and the disturbance is much less than the focal length.

One way to attack this problem would be to use Equations (2-19) and (2-20). Unfortunately the pupil function G is often unknown. Since the average OTF may be known, however, we look for a way to compute I from τ. This is easily found since Equation (2-21) shows that I and τ are Fourier transform pairs.

$$I(X,Y) = \frac{C}{(\lambda f)^2} \iint_{-\infty}^{\infty} \tau\left(\frac{x}{\lambda f},\frac{y}{\lambda f}\right) \exp\left[-\frac{ik}{f}(xX + yY)\right]\, dx\, dy \tag{2-43}$$

In polar coordinates with rotational symmetry we have

$$I(R) = \frac{2\pi C}{(\lambda f)^2} \int_0^D \tau\left(\frac{r}{\lambda f}\right) J_0\left(\frac{2\pi rR}{\lambda f}\right) r\, dr, \tag{2-44}$$

where

$$R = \sqrt{X^2 + Y^2}, \tag{2-45}$$

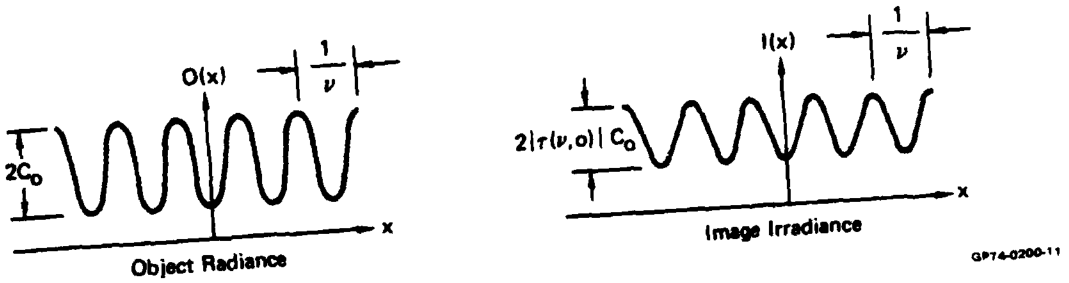

FIGURE 11
MODULATION TRANSFER FUNCTION AS THE SINE-WAVE RESPONSE FUNCTION OF AN IMAGING SYSTEM

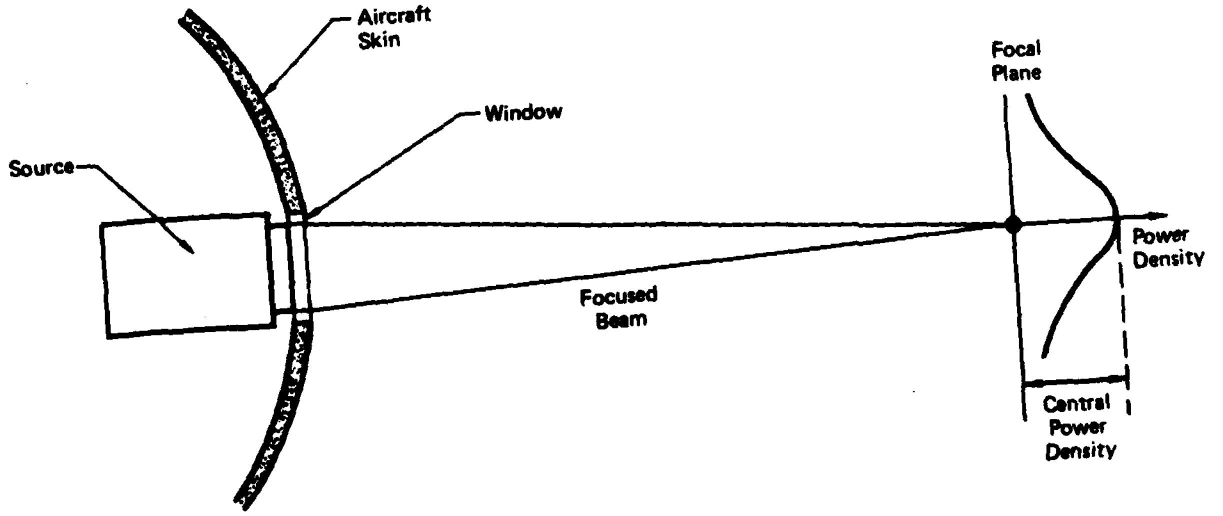

FIGURE 12
POWER DENSITY FOR A BEAM EMERGING FROM AN AIRCRAFT AND FOCUSED AT A DISTANT POINT

C

D is the aperture diameter, and J_0 is the zero order Bessel function of the first kind. Since integration is a linear process, τ and I may be replaced by their averages in Equations (2-43) and (2-44).

Often the average power density at the beam center is of particular interest. From Equations (2-43) and (2-44) we have

$$I(0,0) = \frac{C}{(\lambda f)^2} \iint_{-\infty}^{\infty} \tau\left(\frac{x}{\lambda f}, \frac{y}{\lambda f}\right) dx\, dy \tag{2-46}$$

and

$$I(0) = \frac{2\pi C}{(\lambda f)^2} \int_0^D \tau\left(\frac{r}{\lambda f}\right) r\, dr. \tag{2-47}$$

In Section V we use the ratio of I(0,0) to the central power density achieved in the diffraction limit, $I_0(0,0)$. By substituting Equation (2-30) into Equation (2-46), we find that

$$I_0(0,0) = \frac{C\Sigma}{(\lambda f)^2}. \tag{2-48}$$

The ratio is then

$$\frac{I(0,0)}{I_0(0,0)} = \frac{1}{\Sigma} \iint_{-\infty}^{\infty} \tau\left(\frac{x}{\lambda f}, \frac{y}{\lambda f}\right) dx\, dy \tag{2-48}$$

or

$$\frac{I(0)}{I_0(0)} = \frac{8}{D^2} \int_0^D \tau\left(\frac{r}{\lambda f}\right) r\, dr. \tag{2-50}$$

In this report the ratio above is called the normalized central power density (NCPD).

The NCPD can also be expressed in terms of the optical phase Δ by using Equations (2-18), (2-19), (2-20), (2-24) and (2-48).

$$\text{NCPD} = \frac{1}{\Sigma^2} \left| \iint_{-\infty}^{\infty} G_0(x,y)\, e^{ik\Delta(x,y)} dx\, dy \right|^2 \tag{2-51}$$

If we have polar coordinates with rotational symmetry, Equation (2-51) becomes

$$\text{NCPD} = \frac{64}{D^4} \left| \int_0^{D/2} e^{ik\Delta(r)} r\, dr \right|^2. \tag{2-52}$$

Aerodynamic Similarity Rule

The aerodynamic similarity rule, which is taken from fluid flow theory,* states that two similar models of different scale will produce similar flow if certain conditions are met.[9] This rule is used in developing optical scaling rules in Section V.

In general, the fluids for the two models are different, and there are six conditions that must be met. Before these conditions are presented it is necessary to introduce some notation. Let us define the following terms for any model.

X	characteristic linear dimension (for instance, the distance between two given points on the model)
t	characteristic time (for example, the time it takes for a fluid molecule to travel along the model surface from one given point to another)
V	fluid speed
c_p	fluid specific heat at constant pressure
c_v	fluid specific heat at constant volume
a	speed of sound in the fluid
g	gravitational acceleration
ρ	fluid density
μ	fluid coefficient of viscoisty
κ	fluid coefficient of thermal conductivity

General Conditions. Two similar models of different scale will produce similar flows if the following conditions are met.

1. Corresponding values of the time scale (X/tV) are equal
2. Corresponding values of the ratio of specific heats ($\gamma = c_p/c_v$) are equal
3. Corresponding values of the mach number ($M = V/a$) are equal
4. When gravitational body forces on the fluid are important, corresponding values of the Froede number (gX/V^2) are equal.
5. Corresponding values of the Reynolds number ($R_x = \rho VX/\mu$) are equal
6. Corresponding values of the Prandtl number ($\mu cp/\kappa$) are equal.

Although there are six conditions which generally must be met, only three are important with respect to high speed aircraft.

Pertinent Conditions. Because the change in gravitational acceleration is negligible over the entire region near the aircraft, gravitational body forces on the fluid are not important and Condition 4 can be neglected. Condition 2 can be neglected because the fluid under consideration is always air which has a constant

---

* We refer here to the differential equations of motion of a viscous, compressible, heat conducting fluid. Because some of these equations are nonlinear partial differential equations, a general solution has never been found. The interested reader is referred to a text on fluid mechanics such as References 9 and 10.

γ of 1.4. Finally Condition 6 may be neglected because a constant γ implies a constant Prandtl number.[9] The remaining Conditions 1, 3, and 5 which are pertinent to high speed aircraft state that corresponding values of

Time scale (X/tV)
Mach Number (V/a)
Reynolds number ($\rho VX/\mu$)

are equal for the two models. The values of a and μ, which are functions of temperature only, are given by

$$a = \sqrt{\frac{\gamma P}{\rho}} = \sqrt{287\ \gamma T}\ \text{m/sec} \tag{2-53}$$

and

$$\mu = 17.89 \times 10^{-6}\left(\frac{T}{288.15}\right)^{3/4}\ \text{kg/m-sec} \tag{2-54}$$

where T is temperature in °K. Consider now two models, 1 and 2. To meet Conditions 1, 3, and 5 we require

$$X_1/t_1V_1 = X_2/t_2V_2 \tag{2-55}$$

$$V_1/a_1 = V_2/a_2 \tag{2-56}$$

$$\rho_1V_1X_1/\mu_1 = \rho_2V_2X_2/\mu_2 \tag{2-57}$$

If the temperatures for the two models are equal, then $a_1 = a_2$, $\mu_1 = \mu_2$, and Equations (2-55), (2-56), and (2-57) imply

$$V_2 = V_1 \text{ or } M_1 = M_2 \tag{2-58}$$

$$t_2 = t_1 \frac{X_2}{X_1} \tag{2-59}$$

and

$$\rho_2 = \rho_1 \frac{X_1}{X_2} \tag{2-60}$$

This means that if we wish a one-fifth scale model (Model 2) to produce a flow similar to that of a full size airplane (Model 1), then the speed must be kept the same, and the density must be increased by a factor of five. The characteristic time of the flow will decrease by a factor of five.

III. Controlled Effects

This section presents a discussion of the controlled wavefront deviations caused by the main-flow region and by shock waves.

Main Flow

This subsection presents a general method for predicting the optical phase disturbance $\Delta(x,y)$ caused by density variation in the main-flow region of a subsonic body. This method is then applied to the main-flow field about a sphere.

General Method. Figure 13(a) demonstrates the problem. A beam emerges from an aircraft, traverses the main-flow region, and is focused at a point very far away. The wavefront emerging from the aperture is assumed to be plane parallel. We wish to predict the wave phase $\Delta(x,y)$ at a distance L from the aircraft such that density beyond L is essentially equal to freestream density. The solution to this problem is also the solution to the problem represented by Figure 13(b). We are given a plane parallel wavefront at L moving toward the aircraft, and we wish to know $\Delta(x,y)$ at the aircraft.

We begin by stipulating that

$$\Delta(0,0) = 0 \tag{3-1}$$

where the origin is taken as the center of the outgoing wavefront. The phase may then be expressed as

$$\Delta(x,y) = \int_0^L [n(x,y,z) - n(0,0,z)]\, dz \tag{3-2}$$

where n is refractive index. Substituting Equation (2-5) into Equation (3-2), we have

$$\Delta(x,y) = K \int_0^L [\rho(x,y,z) - \rho(0,0,z)]\, dz \tag{3-3}$$

where ρ is density and K is a constant given by Equation (2-6) or approximately by Equation (2-7). In order to solve Equation (3-3) it is necessary to find the density field about the aircraft (neglecting the boundary-layer and separated-flow regions). This can be done by first finding the velocity field for an incompressible fluid using potential flow theory and then applying the Karman-Tsien hodograph method as presented by Liepman and Puckett.[11]

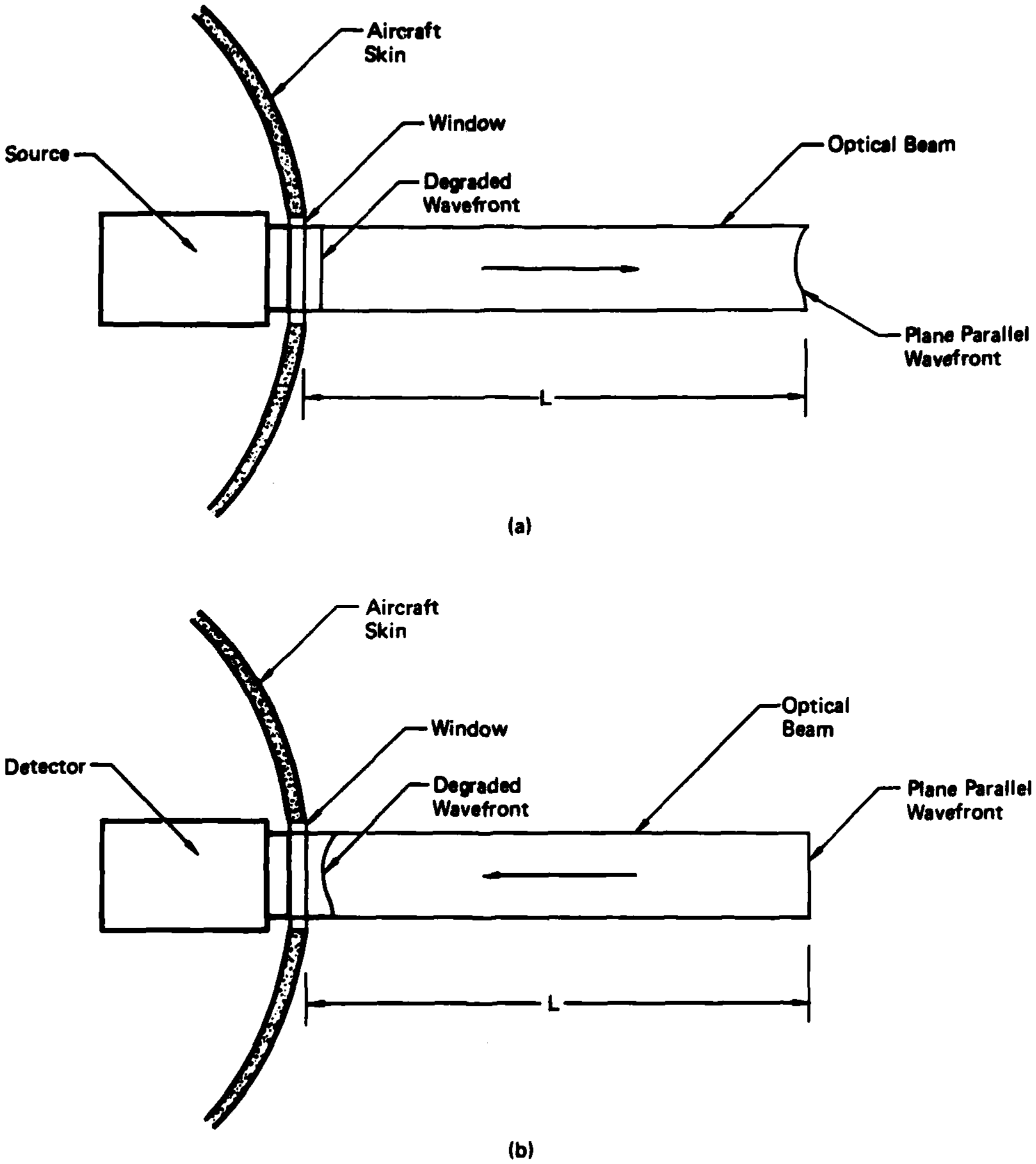

FIGURE 13
WAVEFRONT ERROR CAUSED B Y MAIN F LOW

GP74-0200-13

In working this type of problem it is helpful to use the reference system shown in Figure 14. The aircraft is stationary as is a very large fictitious reservoir of compressed air. A large hole in the reservoir allows air to escape and pass by the aircraft at a free stream speed U. We let a_0 and a_∞ represent the speed of sound in the reservoir and in the freestream respectively, and we let ρ_0 and ρ_∞ represent the air density in the reservoir and in the freestream respectively. The quantities U, a_∞, and ρ_∞ are given.

Using the shape of the aircraft and the given value of U, the velocity square field $V^2(x,y,z)$ for an incompressible fluid is found from potential flow theory. General methods for calculating V^2 are not considered here, except for the following comment. The field V^2 can be easily found for some simple shapes such as for a sphere. For more complicated shapes, solutions can be found by superimposing the velocity potentials of simple shapes.[10]

Once $V^2(x,y,z)$ is found, the density field $\rho(x,y,z)$ can be found by the following approximation from the Karman-Tsien hodograph method.[11]

$$\rho(x,y,z) = \rho_0 \frac{4a_0^2 - V^2(x,y,z)}{4a_0^2 + V^2(x,y,z)} \tag{3-4}$$

This equation may be rewritten in terms of ρ_∞ and a_∞ instead of ρ_0 and a_0 by applying the equalities[11]

$$a_0^2 = \frac{\gamma-1}{2} U^2 + a_\infty^2 \tag{3-5}$$

and

$$\rho_0 = \rho_\infty \left(1 + \frac{\gamma-1}{2} \frac{U^2}{a_\infty^2}\right)^{\frac{1}{\gamma-1}} \tag{3-6}$$

where γ is the ratio of specific heats. For air $\gamma = 1.4$. Using Equations (3-4), (3-5), and (3-6), Equation (3-3) may be expressed as

$$\Delta(x,y) = H \int_0^L \frac{1 - w'(x,y,z)}{1 + w'(x,y,z)} - \frac{1 - w'(0,0,z)}{1 + w'(0,0,z)}\, dz \tag{3-7}$$

where

$$H = K\rho_\infty \left[1 + \frac{\gamma-1}{2} M_\infty^2\right], \tag{3-8}$$

$$M_\infty = U/a_\infty = \text{freestream Mach number}, \tag{3-9}$$

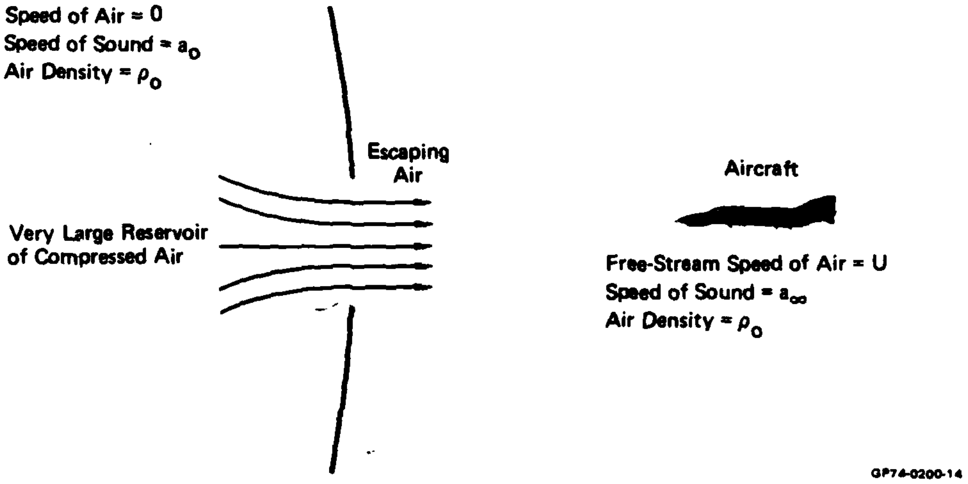

FIGURE 14
REFERENCE SYSTEM FOR MAIN-FLOW PROBLEM

and

$$w'(x,y,z) = \frac{V^2(x,y,z)/a_\infty^2}{2(\gamma-1)M_\infty^2 + 4} . \tag{3-10}$$

Equations (3-7) through (3-10) provide a method for estimating $\Delta(x,y)$ provided

$$V^2(x,y,z) < a_\infty^2 \tag{3-11}$$

for all space. The speed a_∞ is given by[10]

$$a_\infty = \sqrt{\frac{\gamma P_\infty}{\rho_\infty}} = \sqrt{287\gamma T_\infty} \tag{3-12}$$

where T_∞ is the freestream temperature in °K and a_∞ is in meters/sec.

Main Flow for Sphere. To find $\Delta(x,y)$ for a sphere the coordinate system shown in Figure 15 is used. The polar axis points into the flow, and the center of the beam defines the z-axis. The angle between the polar axis and the z-axis is θ_0. The y-axis lies perpendicular to the z-axis in the plane defined by the polar and z axes. The x-axis is perpendicular to both the y and z axes. The beam emerging from the sphere is taken to be plane parallel, lying paralled to the x,y-plane, at $z=R$ where R is the sphere radius. To simplify the problem the following normalized variables are introduced.

$$\zeta = x/R \qquad \eta = y/R \qquad \xi = z/R \tag{3-13}$$

$$\psi^2 = \zeta^2 + \eta^2 + \xi^2 \qquad \ell = L/R \tag{3-14}$$

The derivation in Appendix B shows that wave phase is given by

$$\Delta(x,y) = \Delta'(\zeta,\eta) = K\rho_\infty R c_2 \int_1^\ell \frac{c_1 - q(\theta,\psi)}{c_1 + q(\theta,\psi)} - \frac{c_1 - q(\theta_0,\xi)}{c_1 + q(\theta_0,\xi)} \, d\xi \tag{3-15}$$

where

$$c_1 = [2(\gamma-1)M_\infty^2 + 4]/M_\infty^2 \tag{3-16}$$

$$c_2 = (1 + \frac{\gamma-1}{2} M_\infty^2)^{\frac{1}{\gamma-1}} \tag{3-17}$$

$$q(\theta,\psi) = 1 + (1 - 3\cos^2\theta)/\psi^3 + 1/4(1 + 3\cos^2\theta)/\psi^6 \tag{3-18}$$

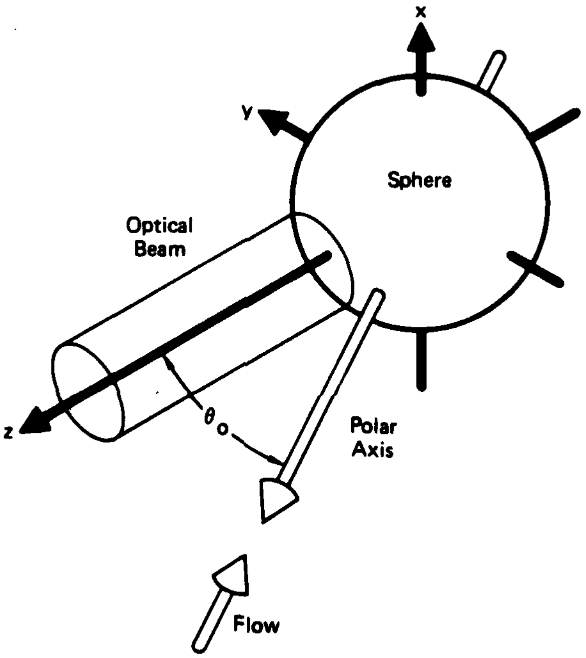

GP74-0200-15

FIGURE 15
COORDINATE SYSTEM FOR MAIN-FLOW SPHERE PROBLEM

and

$$\cos\theta = (\xi \cos\theta_0 - \eta \sin\theta_0)/\psi. \tag{3-19}$$

Equation (3-15) is not valid if at any point in space $V^2 = U^2 q \geq a_\infty$. Since the maximum value of q is 9/4 as shown in Appendix B, we must have

$$M_\infty^2 < \frac{4}{9} \text{ or } M_\infty < \frac{2}{3} \tag{3-20}$$

If M_∞ exceeds this limit, V will reach the speed of sound, and a shock wave will form.

Figure 16 shows plots of $\Delta'(0,\eta)/\rho_\infty R$ at Mach 0.6 for several values of θ_0. The plots were obtained by evaluating Equation (3-15) numerically. The upper limit used was $\ell = 50$, which effectively is the same as $\ell = \infty$.

These calculations of Δ are based on a compressible but nonviscous fluid. A real fluid such as air would produce a flow separation aft of the sphere at very low Mach numbers, and calculated values of Δ for paths traversing the flow separation are not valid. However, the calculations do provide good estimates for forward-looking paths. In fact the estimate is reasonable for forward-looking paths even if M > 2/3 since the shock wave will occur at polar angles of about 90°.

Although Δ gives a complete description of the optical degradation, the main-flow OTF may also be required. The OTF can be obtained simply by applying Equation (2-27) to Δ. The term Σ in Equation (2-27) refers to the beam cross section. Aircraft are streamlined, and therefore do not have as severe a main-flow optical effect as the sphere. The fact that the sphere does produce a large effect, however, indicates that the main-flow effect should always be considered as a possible source of optical degradation.

Shock Waves

In this subsection a very brief qualitative description of the optical effect of shock waves is presented, and the refraction caused by a plane oblique shock wave is computed.

Qualitative Description. Shock waves are very thin pressure gradients in aircraft boundary flow. They occur only when some part of the flow field has a speed relative to the aircraft greater than the speed of sound. The shock wave thickness is only a small fraction of a centimeter,[12] so that for our purposes the shock wave may be considered a line separating two regions of different pressures, velocities, and densities. Since refractive index is a linear function of density, the shock wave is also the interface between regions of different refractive indices. Light passing through a shock wave will be refracted according to Snell's law. This effect is generally unimportant in aerial photography, since the image is not degraded but only displaced slightly. An unusual exception is the case of the Refaired Nose RF-4C flying at high subsonic Mach numbers. As air moves past the nose it is accelerated to a speed greater than the speed of sound. Under certain conditions a shock wave forms at the camera window as shown in Figure 17. When this happens a fuzzy band appears on the image format as shown in the figure.[4]

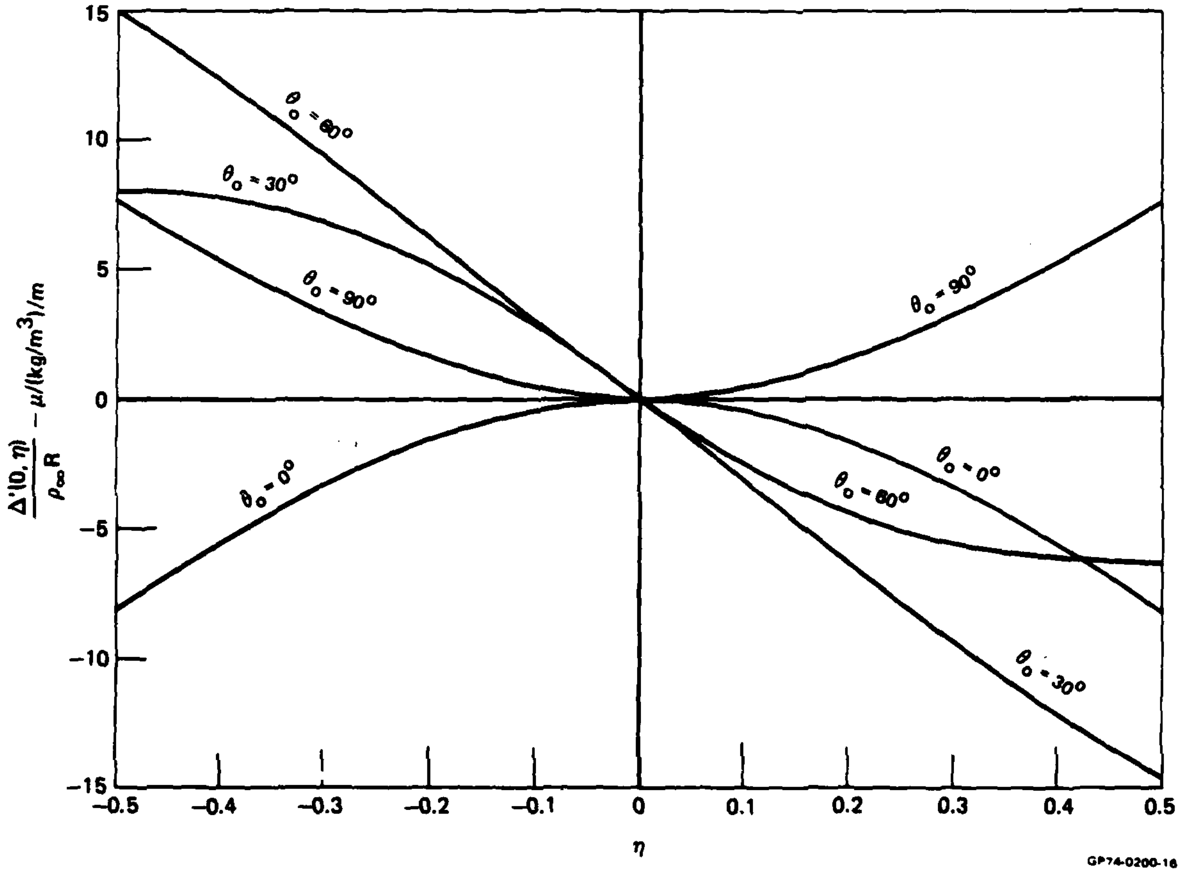

FIGURE 16
NORMALIZED WAVE PHASE [$\Delta'(0,\eta)/\rho_\infty R$] vs NORMALIZED DISPLACEMENT (η)
FOR THE MAIN-FLOW SPHERE PROBLEM

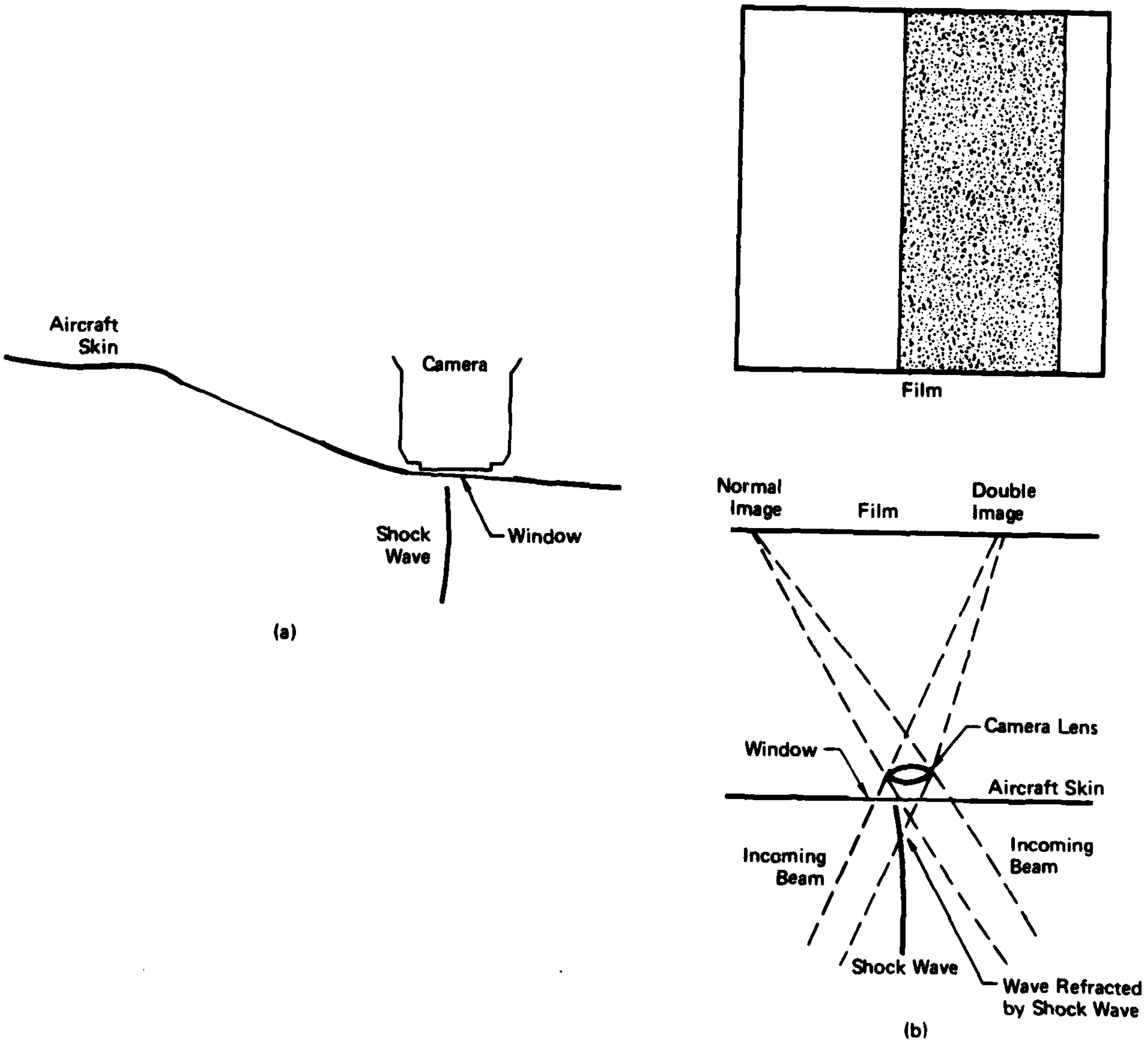

FIGURE 17
FORMATION OF SHOCK WAVE ON CAMERA WINDOW OF THE REFAIRED-NOSE RF-4C AIRCRAFT AND ITS EFFECT ON THE IMAGING SYSTEM

GP74-0200-17

Light from the ground area corresponding to the fuzzy band arrives at the camera with an angle such that part of the light does not cross the shock wave but the rest does cross and is therefore refracted. The result is a double image which is the fuzzy band.

The description of the shock wave as the interface between media of different refractive indices is somewhat oversimplified. In general shock waves are curved, and the refractive index on either side varies continuously along the shock wave. This complication causes the shock wave to not only refract light passing through it, but also to distort the optical wavefront. No attempt is made here to analyze such a distortion. The angular deviation caused by refraction for a plane wave is analyzed, however, in the next subsection.

Refraction by a Plane Shock Wave. Although refraction is usually not a problem in aerial photography, it is important in optical systems for which the target must be accurately located. Here we derive the angular refraction caused by the plane shock wave which is produced by the geometry shown in Figure 18. Air travels at some supersonic speed u_1 parallel to the horizontal surface. When the air reaches the ramp inclined at an angle θ, the air is turned parallel to the ramp and a shock wave is formed. We define the angle of the shock wave to be β and the horizontal and vertical components of the deflected stream of air to be u_2 and v_2 respectively. The air densities to the left and to the right of the shock wave are ρ_1 and ρ_2 respectively. The temperature and speed of sound to the left are T_∞ and a_∞ respectively.

We will show how ρ_2 can be found from a knowledge of u_1, ρ_1, T_∞, and either θ or β. Once ρ_1 and ρ_2 are known it is a simple matter to find their corresponding refractive indices n_1 and n_2. Snell's law then gives the angle of refraction for light crossing the shock wave.

Before going into the derivation it is necessary to define the critical speed of sound a_c. Going back to the reference system of Figure 13, a_c is defined as the freestream speed U when U is equal to the freestream speed of sound a_∞. In other words, when the freestream Mach number is unity ($M_\infty = U/a_\infty = 1$), then we have $a_c = U = a_\infty$. The speed a_c may be expressed in terms of U and M_∞ by[11]

$$a_c^2 = U^2 \frac{\gamma - 1 + 2/M_\infty^2}{\gamma + 1} . \qquad (3\text{-}21)$$

Notice that when $M_\infty = 1$, Equation (3-21) reduces to $a_c = U$ as expected.

Going back to Figure 18, we see that simple geometry provides the relationship

$$\tan \theta = \frac{v_2}{u_2} . \qquad (3\text{-}22)$$

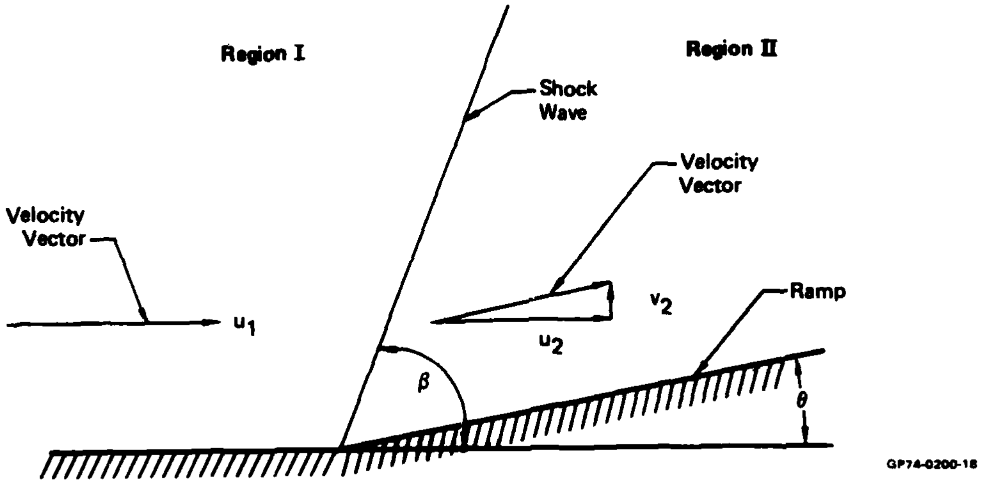

FIGURE 18
FORMATION OF A PLANE OBLIQUE SHOCK WAVE

By using the laws of conservation of mass, momentum, and energy, it can be shown that u_2 and v_2 must also satisfy the following equation.[11]

$$v_2^2 = \frac{(u_1 - u_2)^2 \, (u_1 u_2 - a_c^2)}{\frac{2}{\gamma+1} u_1^2 - u_1 u_2 + a_c^2} \tag{3-23}$$

Equations (3-22) and (3-23) may be rewritten as

$$\tan \theta = \frac{v_2'}{u_2'} \tag{3-24}$$

and

$$(v_2')^2 = \frac{(u_1' - u_2')^2 \, (u_1' u_2' - 1)}{\frac{2}{\gamma+1}(u_1')^2 - u_1' u_2' + 1} \tag{3-25}$$

where

$$u_1' = \frac{u_1}{a_c}, \quad u_2' = \frac{u_2}{a_c}, \quad v_2' = \frac{v_2}{a_c} \, . \tag{3-26}$$

Figure 19 plots v_2' versus u_2' for both Equations (3-24) and (3-25). The values of θ and u_1' for this figure are respectively 15° and 2. The two curves intersect at three points C, D, and E. Values of u_2' and v_2' corresponding to these points satisfy both equations. The value of u_2' at point A on the u_2'-axis is equal to u_1'. Therefore values of (u_2', v_2') to the right of point A require that the flow increase speed as it passes through the shock wave. Such an increase can be shown to be physically impossible since entropy would be required to decrease.[11] We may therefore eliminate the values of u_2' and v_2' at point E from our set of solutions. The remaining two points, C and D, represent the possible velocity components for the flow to the right of the shock wave. Point C is said to represent the solution for a weak shock wave and D a strong shock wave, since the velocity change through the two shock waves are respectively small and large. Generally the shock wave produced experimentally will be the weak shock wave.[11]

Figure 19 can be used to find not only u_2' and v_2' but also the shock wave angle β. Again by using the conservation laws, it can be shown that[11]

$$\tan \beta = \frac{u_1 - u_2}{v_2} \tag{3-27}$$

or

$$\tan \beta = \frac{u_1' - u_2'}{v_2'} . \tag{3-28}$$

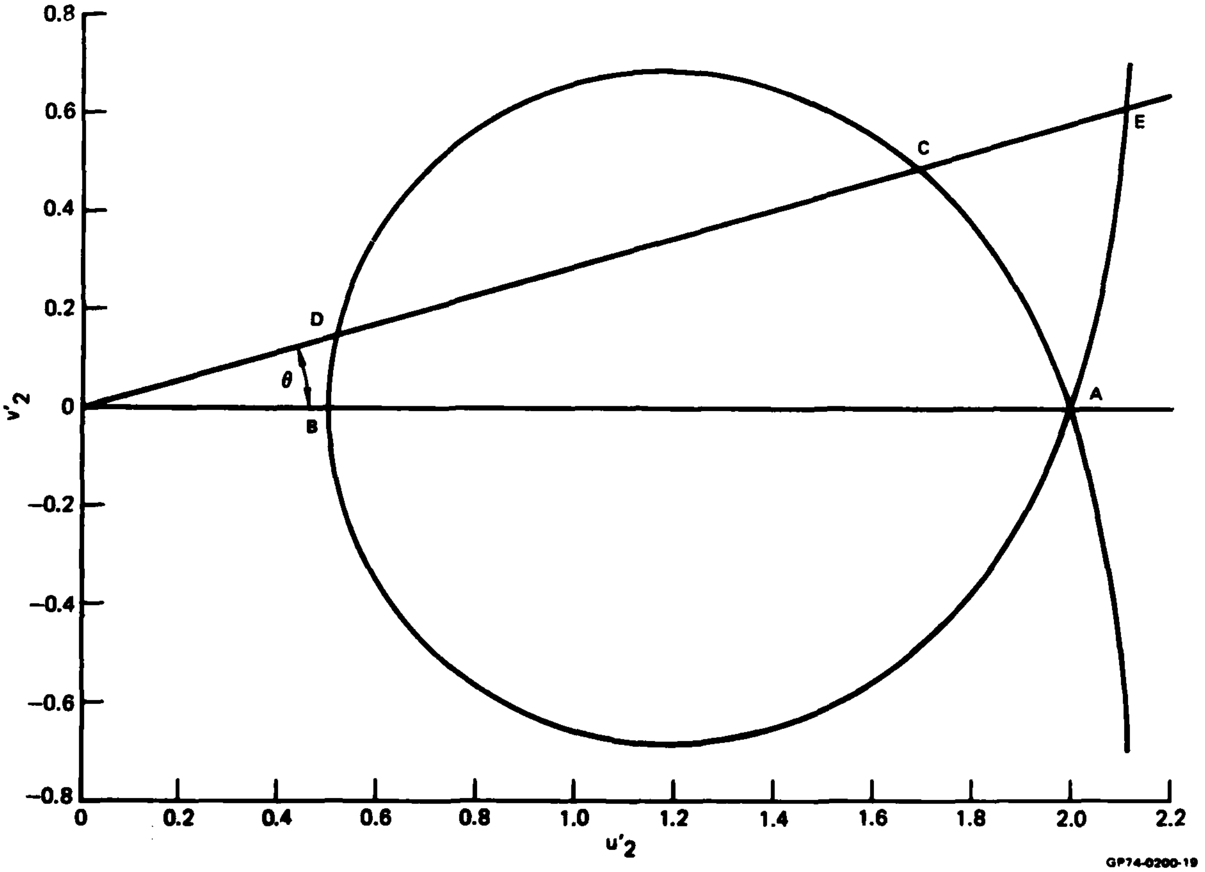

FIGURE 19
GRAPHICAL SOLUTION OF NORMALIZED VELOCITY COMPONENTS (u'_2, v'_2) FOR THE PLANE-SHOCK-WAVE PROBLEM

To find the angle β of the weak shock wave, a vertical line is drawn through point C as shown in Figure 20. This line intersects the u_2'-axis at point F. Since the lengths of the line segments $\overline{FA}$ and $\overline{CF}$ are $u_1' - u_2'$ and v_2' respectively, the angle FCA is equal to β. Going a little further, a perpendicular to the line defined by A and C can be drawn through the origin O. The angle between this perpendicular and the u_2'-axis is also equal to β. Figure 20 is now a construction of the actual ramp and the weak shock wave. A similar construction for the strong shock wave would show that the strong shock wave has a larger shock wave angle. In the limit as the ramp angle θ approaches zero, the strong shock wave angle approaches 90°. On the other hand, the weak shock wave angle approaches a value given by

$$\sin \beta = \frac{1}{M_\infty} \tag{3-29}$$

where $M_\infty = U/a_\infty = u_1/a_\infty$. Equation (3-29) can be derived by combining Equations (3-21), (3-23) and (3-27) and taking the limit $u_2' \rightarrow u_1'$. The value of a_∞ can be found by using Equation (3-12).

Figure 21 shows that as the ramp angle θ increases, points C and D approach each other until they coincide at the maximum ramp angle θ_{max}. If the flow deflection produced by an obstacle is greater than θ_{max}, a plane shock wave cannot be formed; there is no real solution to the set of equations, (3-24) and (3-25). Instead a curved detached bow wave is formed as shown in Figure 22.

After the values of u_2', v_2', and β have been obtained, the density change across the shock wave can be found by using the equation for mass conservation,[11]

$$\rho_1 u_1 \sin \beta = \rho_2 (u_2 \sin \beta - v_2 \cos \beta) \tag{3-30}$$

or

$$\rho_2 = \rho_1 \frac{u_1' \sin \beta}{u_2' \sin \beta - v_2' \cos \beta} . \tag{3-31}$$

We see now that the density ρ_2 can be obtained by finding u_2', v_2', and β using Equations (3-24) and (3-25) and then by applying Equation (3-31). If the angle β is known a priori, however, ρ_2 can be found without solving for u_2' and v_2' first. As shown in Appendix C, the density ρ_2 may also be expressed as

$$\rho_2 = \rho_1 \frac{(\gamma+1) M_\infty^2 \sin^2 \beta}{(\gamma-1) M_\infty^2 \sin^2 \beta + 2} . \tag{3-32}$$

The density change is

$$\Delta\rho = \rho_2 - \rho_1 = \rho_1 \frac{2M_\infty^2 \sin^2 \beta - 2}{(\gamma-1) M_\infty^2 \sin^2 \beta + 2} , \tag{3-33}$$

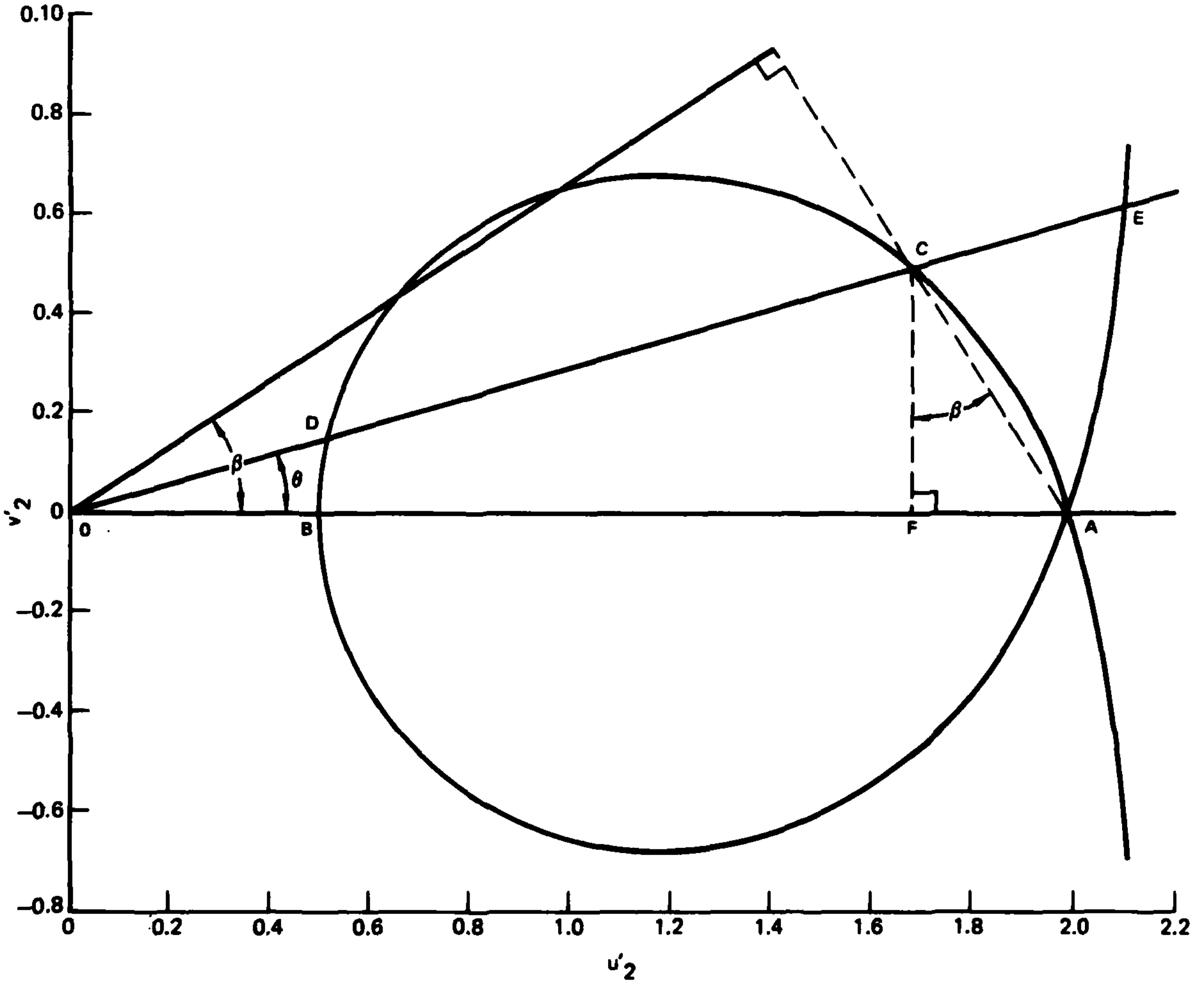

GP74-0200-20

FIGURE 20
GRAPHICAL SOLUTION OF SHOCK-WAVE ANGLE β FOR THE PLANE-SHOCK-WAVE PROBLEM

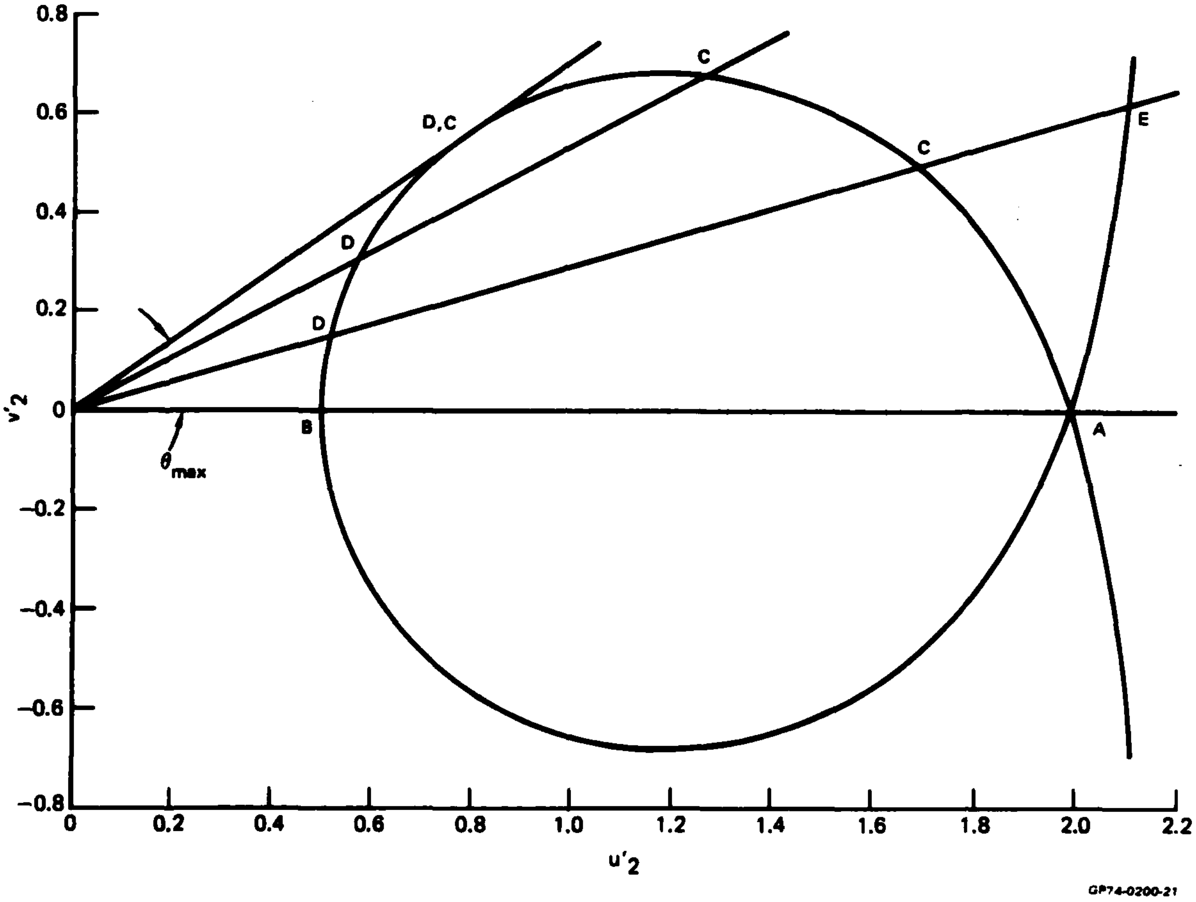

FIGURE 21
UPPER LIMIT OF RAMP ANGLE θ_{MAX} FOR A PLANE SHOCK WAVE

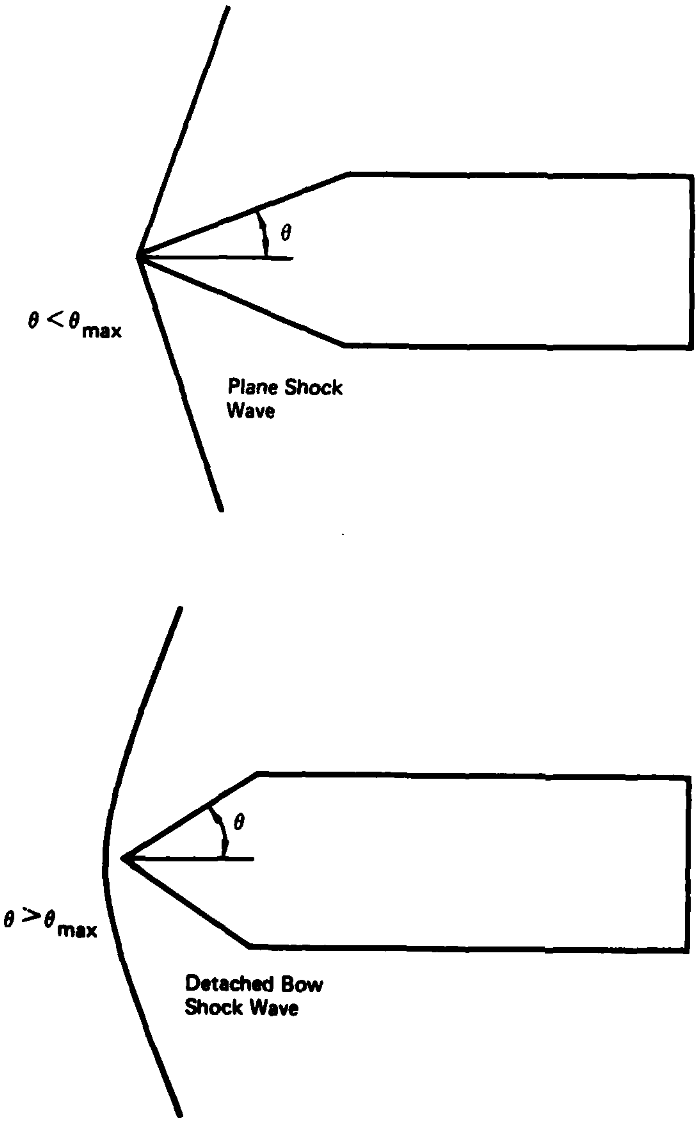

GP74-0200-22

FIGURE 22
DETACHED BOW SHOCK WAVE

and the refractive index change is

$$\Delta n = n_2 - n_1 = (1 + K\rho_1) - (1 + K\rho_2) = K\Delta\rho \tag{3-34}$$

or

$$\Delta n = 2K\rho_1 \frac{M_\infty^2 \sin^2 \beta - 1}{(\gamma-1)M_\infty^2 \sin^2 \beta + 2} \tag{3-35}$$

where K is given by Equation (2-6) or approximately by $K = 0.223 \times 10^{-3}$ m^3/kg. We now wish to find the refraction angle $\Delta\phi$ for a beam intersecting the shock wave. We let ϕ be the angle between the beam and the normal to the shock wave as shown in Figure 23. Snell's law, $n \sin \phi$ = const., is differentiated,

$$dn \sin \phi + n \cos \phi \, d\phi = 0 \tag{3-36}$$

or

$$d\phi = - \tan \phi \, dn. \tag{3-37}$$

Since Δn is very small, Equation (3-37) may be written as a difference equation,

$$\Delta\phi = - \tan \phi \, \Delta n. \tag{3-38}$$

Finally, Equation (3-35) is substituted in Equation (3-38).

$$\Delta\phi = - 2K\rho_1 \frac{M_\infty^2 \sin^2 \beta - 1}{(\gamma-1)M_\infty^2 \sin^2 \beta + 2} \tan \phi \tag{3-39}$$

The minus sign indicates that when the beam crosses the shock wave from Region I (lower density) to Region II (higher density), the beam is refracted toward the shock wave normal as shown in Figure 23. Figure 24 shows $\Delta\phi/\rho_1 \tan \phi$ plotted as a function of β for various Mach numbers. The dotted line divides the plot into strong and weak shock waves. Figure 25 shows $\Delta\phi/\rho_1 \tan \phi$ plotted as a function of M_∞ for both the strong normal shock wave ($\theta = 0°$, $\beta = 90°$) and for the shock wave at $\theta = \theta_{max}$. Since strong attached shock waves generally do not occur in practice, the curve for $\theta = \theta_{max}$ represents the maximum angular deviation that is likely to occur. The curve for $\theta = 0°$ and $\beta = 90°$ represents the maximum angular deviation that can occur under any circumstance.

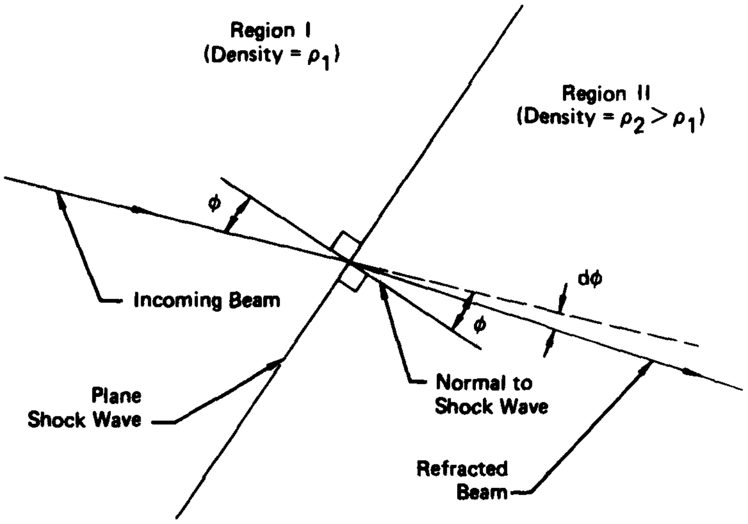

FIGURE 23
REFRACTION OF A BEAM BY A PLANE SHOCK WAVE

GP74-0200-23

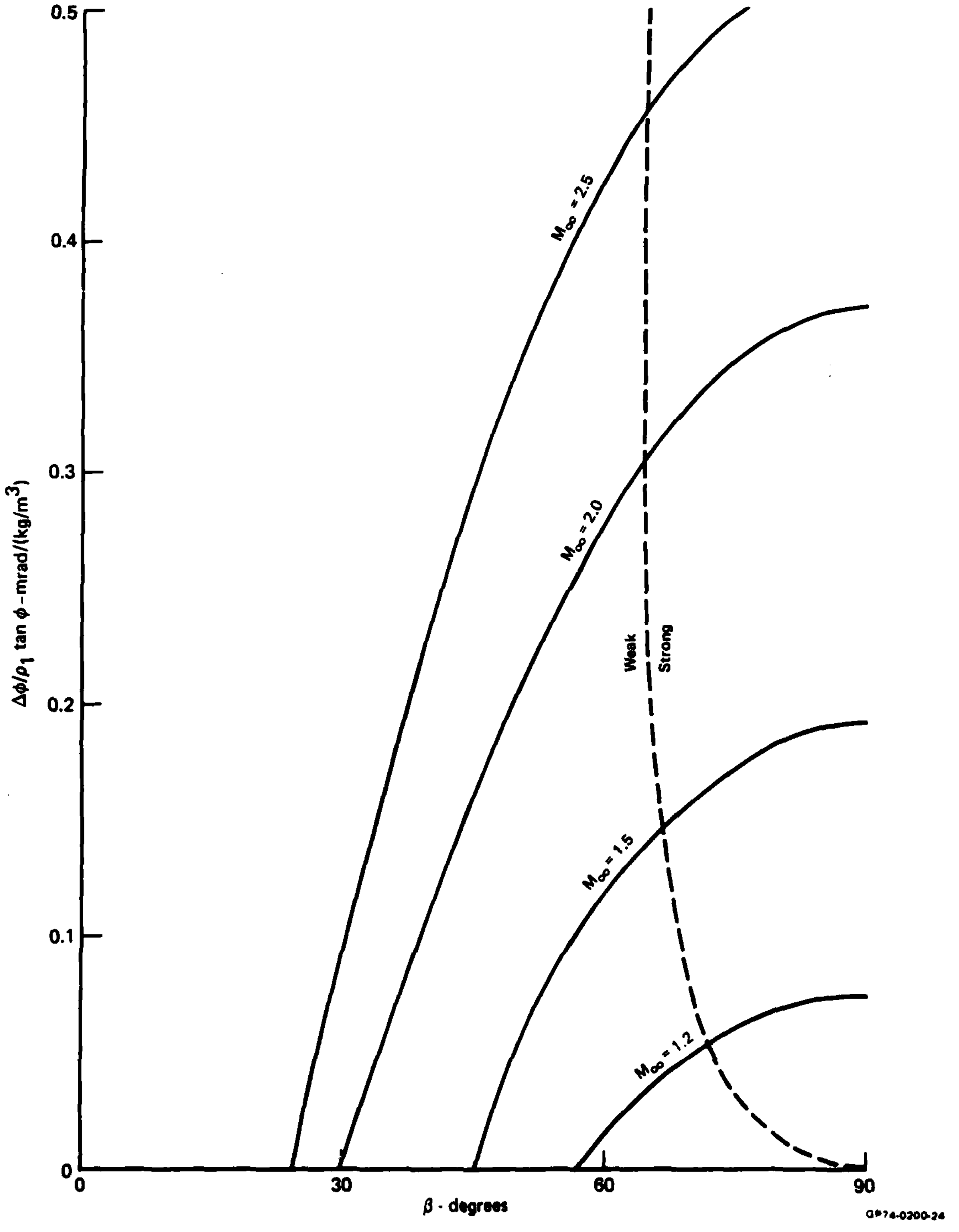

FIGURE 24
NORMALIZED REFRACTION ANGLE ($\Delta\phi/\rho_1$ TAN ϕ) vs SHOCK-WAVE ANGLE β FOR VARIOUS FREE-STREAM MACH NUMBERS M_∞

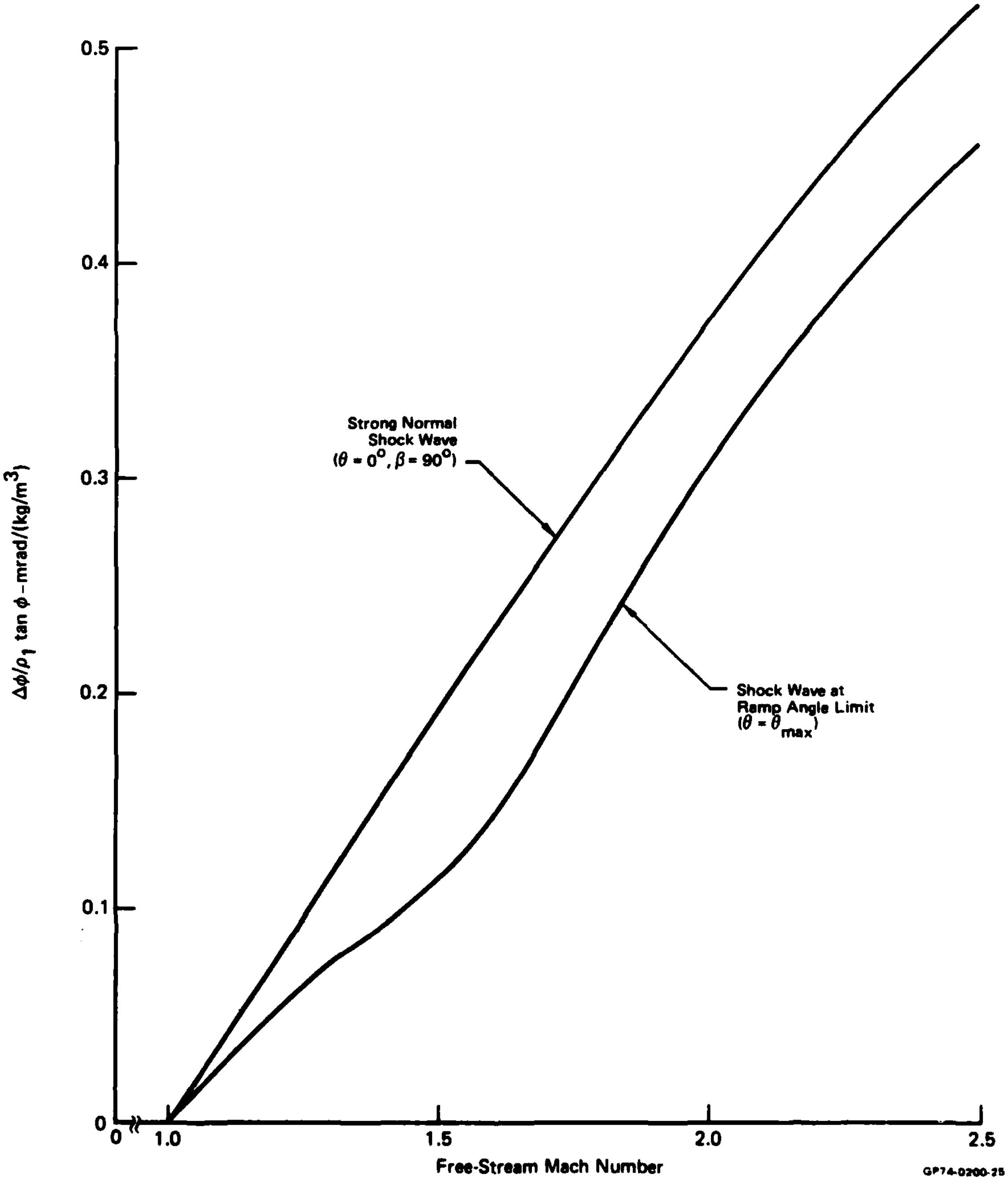

FIGURE 25
NORMALIZED REFRACTION ANGLE ($\Delta\phi/\rho_1$ TAN ϕ) vs FREE-STREAM MACH NUMBER FOR THE STRONG NORMAL SHOCK WAVE AND THE SHOCK WAVE AT THE RAMP-ANGLE LIMIT ($\theta = \theta_{MAX}$)

IV. Random Effects

The purpose of this section is to present imperical methods for estimating the optical effects of turbulent boundary layers and separated flow. First analytic equations for the average OTF and the variance of the wavefront phase σ^2 are presented. After a general description of the turbulent boundary layer, the Stine-Winovich experiment is described. The results of the experiment are used to evaluate σ^2 and the average OTF for a TBL. Separated flow is presented in a similar way. After a general description of separated flow, data from the RF-4C wind tunnel test is used to evaluate σ^2 and the average OTF. Finally, Kelsall's experiment with a shearing interferometer is described. This experiment is important because the shearing interferometer technique is capable of measuring MTF's directly.

Equations for Average OTF and σ^2

The purpose of this subsection is to present analytic equations for the average OTF and for σ^2.

Equation for Average OTF. Because the aperture wave phase Δ is an unknown random variable, the OTF is also an unknown random variable. It is possible, however, to derive a model for the average OTF based on the stochastic properties of Δ. The derivation of the model is given by O'Neill[8] and, in more complete form, by Barakat.[13] Since both of these derivations make use of rather advanced theorems from probability theory, a third simplified derivation is given in Appendix D. All of these derivations assume that Δ defines a spatially stationary Gaussian random process.

As stated by Barakat:

> "This is purely a working hypothesis backed in part by a central limit theorem argument. The spatial stationarity condition ... is mainly one of convenience and can be relaxed at the cost of more encumbering mathematics."

The derivations show that the expected value of the OTF is

$$E\left[\tau\left(\frac{x}{\lambda f},\frac{y}{\lambda f}\right)\right] = \tau_C\left(\frac{x}{\lambda f},\frac{y}{\lambda f}\right) \exp\left\{-k^2[\sigma^2-\Phi(x,y)]\right\} \tag{4-1}$$

where $\Phi(x,y)$ and σ^2 are respectively the covariance function and variance of Δ. The function τ_C is the OTF which would result if there were controlled aberrations only. If there are no controlled aberrations, τ_C becomes the diffraction OTF, and Equation (4-1) becomes

$$E\left[\tau\left(\frac{x}{\lambda f},\frac{y}{\lambda f}\right)\right] = \tau_0\left(\frac{x}{\lambda f},\frac{y}{\lambda f}\right) \exp\left\{-k^2[\sigma^2-\Phi(x,y)]\right\} . \tag{4-2}$$

Throughout this section, only random aberrations are considered, and Equation (4-2) is used instead of Equation (4-1).

If we define the ratio of τ to τ_0 (or τ_C) as the OTF of the random fluctuations only, then the expected value of the random OTF, τ_R, is

$$E\left[\tau_R\left(\frac{x}{\lambda f},\frac{y}{\lambda f}\right)\right] = \exp\left\{-k^2[\sigma^2-\Phi(x,y)]\right\}. \tag{4-3}$$

By definition we have

$$\Phi = E[\Delta(x',y')\Delta(x'+x,\ y'+y)] - E[\Delta(x',y')]E[\Delta(x'+x,\ y'+y)] \tag{4-4}$$

and

$$\sigma^2 = E\left[\{\Delta(x',y') - E[\Delta(x',y')]\}^2\right]. \tag{4-5}$$

Expanding Equation (4-5) yields

$$\sigma^2 = E[\Delta^2(x',y')] - \{E[\Delta(x',y')]\}^2 = \Phi(0,0). \tag{4-6}$$

Because spatial stationarity is assumed, Φ is a function of x and y only, $E(\Delta)$ is constant, and σ^2 is constant. Without loss of generality we take the expected value of Δ to be zero. We now have

$$\Phi(x,y) = E[\Delta(x',y')\Delta(x'+x,y'+y)] \tag{4-7}$$

and

$$\sigma^2 = E[\Delta^2(x',y')] = \Phi(0,0). \tag{4-8}$$

Since obtaining averages from an ensemble is impractical, time averages are used under the assumption that time and ensemble averages are equal. Equations (4-2), (4-3), (4-4), and (4-8) become

$$\overline{\tau}\left(\frac{x}{\lambda f},\frac{y}{\lambda f}\right) = \tau_0\left(\frac{x}{\lambda f},\frac{y}{\lambda f}\right)\tau_R\left(\frac{x}{\lambda f},\frac{y}{\lambda f}\right) \tag{4-9}$$

$$\overline{\tau}_R\left(\frac{x}{\lambda f},\frac{y}{\lambda f}\right) = \exp\left\{-k^2[\sigma^2-\Phi(x,y)]\right\} \tag{4-10}$$

$$\Phi(x,y) = \overline{\Delta(x',y')\Delta(x'+x,y'+y)} \tag{4-11}$$

and

$$\sigma^2 = \Phi(0,0) = \overline{\Delta^2(x',y')} \tag{4-12}$$

where the overbar indicates time average. Since $\overline{\tau}_R$ and τ_0 are both real, $\overline{\tau}_R$ and $\overline{\tau}$ are average MTF's as well as average OTF's.

It is still necessary to find a functional form for Φ. Again we adopt the attitude of Barakat. (Barakat's R_z is equivalent to Φ).

> "...in lieu of any contrary evidence R_z is taken to be Gaussian as a mathematical convenience rather than because it has a physical foundation. I have reason to believe that the actual shape of R_z (provided it be a smooth function) is less important than its spatial spread."

The function $\Phi(x,y)$ can now be written

$$\Phi(x,y) = \sigma^2 \exp\left[-\left(\frac{x^2}{a_x{}^2} + \frac{y^2}{a_y{}^2}\right)\right] \tag{4-13}$$

where a_x and a_y are the correlation lengths in the x and y directions respectively. Throughout the rest of this report, the random wavefront aberrations are assumed to be isotropic, that is,

$$a_x = a_y = a. \tag{4-14}$$

Equation (3-12) may now be written

$$\Phi(x,y) = \Phi(r) = \sigma^2 e^{-(r/a)^2}. \tag{4-15}$$

The average random OTF becomes

$$\overline{\tau}_R\left(\frac{r}{\lambda f}\right) = \exp\left\{-k^2\sigma^2\left[1-e^{-(r/a)^2}\right]\right\} \tag{4-16}$$

or

$$\overline{\tau}_R(\nu) = \exp\left\{-k^2\sigma^2\left[1-e^{-(\lambda f\nu/a)^2}\right]\right\} \tag{4-17}$$

where

$$\nu = \frac{r}{\lambda f}. \tag{4-18}$$

We now have a two parameter (σ^2 and a) model for the time average OTF. Notice that $\overline{\tau}_R$ never falls to zero but has a minimum value given by

$$\tau_{min} = e^{-k^2\sigma^2}. \tag{4-19}$$

Equation (4-16) is plotted in Figure 26 for different values of σ/λ and a. The σ^2 parameter determines how low $\overline{\tau}_R$ will drop, and the correlation length a is a scale factor for the spatial frequency ν. Usually σ^2 and a must be found experimentally; however, the following analytic development does show the dependence of σ^2 on such parameters as density and velocity.

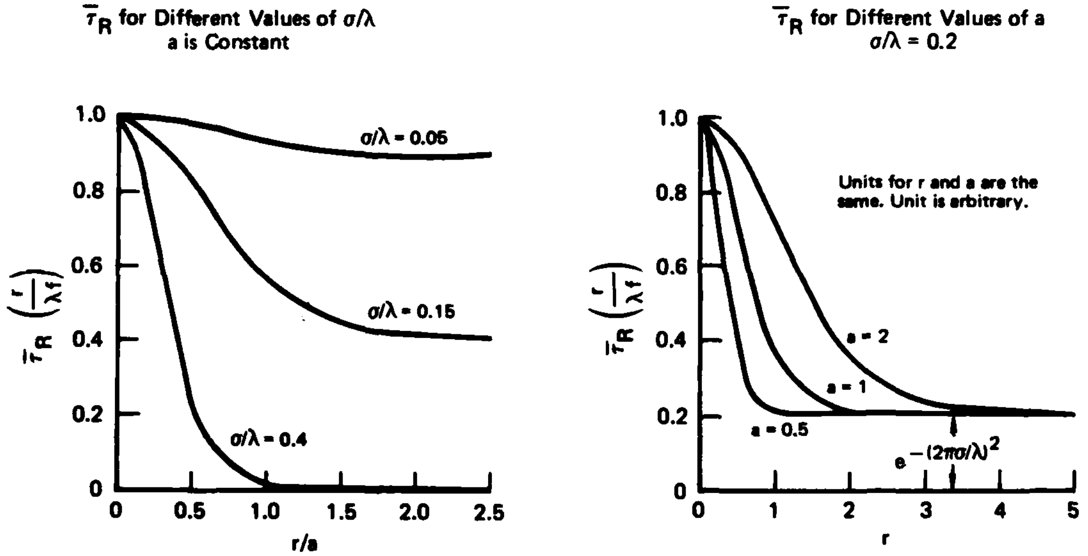

$\bar{\tau}_R$ for Different Values of σ/λ
a is Constant

$\bar{\tau}_R$ for Different Values of a
$\sigma/\lambda = 0.2$

Units for r and a are the same. Unit is arbitrary.

GP74-0200-26

FIGURE 26
AVERAGE RANDOM OTF, $\bar{\tau}_R$, FOR VARIOUS VALUES OF σ/λ AND a

Equation for σ^2. Both Chernov[14] and Tatarski[15] have derived an equation for σ^2 in terms of the variance of the refractive index as a special case of a more general problem. Chernov has also used a simple and direct approach, but has omitted some of the steps. For this reason, a complete direct derivation is given in Appendix E. The equation for σ^2 is found to be

$$\sigma^2 = \sqrt{\pi}\, a\, L\, \overline{\mu^2} \tag{4-20}$$

where a is wavefront correlation length, L is optical path length through the medium, and $\overline{\mu^2}$ is the variance of the refractive index. The definition of μ is

$$\mu = n - \bar{n}, \tag{4-21}$$

so that

$$\overline{\mu^2} = \overline{(n-\bar{n})^2} = \overline{n^2} - \bar{n}^2. \tag{4-22}$$

The assumptions made in the derivation are that $\mu \ll 1$ and that μ has a Gaussian covariance function,

$$\overline{\mu(x',y',z')\mu(x'+x,y'+y,z'+z)} = \overline{\mu^2}\exp[-(x^2+y^2+z^2)/a^2] \tag{4-23}$$

where $a \ll L$. The parameter a in Equation (4-23) is the same as the wavefront correlation length. In fact, it is shown in Appendix E, that Equation (4-15), which gives the functional form for Φ, is implied by Equation (4-23).

One way of estimating $\overline{\mu^2}$ is to relate the refractive index fluctuation to density fluctuations and then the density fluctuations to pressure fluctuations, which can be measured at the airplane skin. The transfer from density to pressure fluctuation is made by assuming that the pressure changes are adiabatic. We start by substituting Equation (2-5) into Equation (4-22)

$$\overline{\mu^2} = \overline{n^2} - \bar{n}^2 = \overline{(1+K\rho)^2} - \overline{1+K\rho}^{\,2} \tag{4-24}$$

$$\overline{\mu^2} = 1 + 2K\bar{\rho} + K^2\overline{\rho^2} - (1 + 2K\bar{\rho} + K^2\bar{\rho}^2) \tag{4-25}$$

$$\overline{\mu^2} = K^2(\overline{\rho^2} - \bar{\rho}^2) = K^2\overline{(\rho-\bar{\rho})^2} = K^2\overline{(\Delta\rho)^2} \tag{4-26}$$

where ρ is density and K is a constant given by Equation (2-6) or approximately by $K = 0.223 \times 10^{-3}\ \mathrm{m^3/kg}$. The term $\Delta\rho$ represents density variation from the mean. The adiabatic law,

$$P\rho^{-\gamma} = \text{const} \tag{4-27}$$

where P is pressure and γ is the ratio of specific heats (=1.4), is differentiated to give

$$\rho^{-\gamma}dP - \gamma P\rho^{-(\gamma+1)}d\rho = 0. \tag{4-28}$$

Since we are working with small changes in pressure and density, we can write this differential equation as a difference equation. Substituting ΔP and $\Delta\rho$ for dP and $d\rho$ respectively and rearranging, Equation (4-28) becomes

$$\Delta\rho = \frac{\rho}{\gamma P}\,\Delta P. \qquad (4\text{-}29)$$

Generally pressure fluctuation data are given in terms of the fluctuating pressure coefficient, which is defined by

$$C_p = \frac{\sqrt{\overline{\Delta P^2}}}{\frac{1}{2}\rho_\infty U^2} \qquad (4\text{-}30)$$

where U is the airplane speed and ρ_∞ is the freestream density. Combining Equations (4-20), (4-26), (4-29), and (4-30) we have

$$\sigma^2 = \frac{\sqrt{\pi}}{4}\,\frac{K^2}{\gamma^2}\,aL\,\frac{\rho_\infty{}^4 U^4}{P_\infty{}^2}\,C_p{}^2 \qquad (4\text{-}31)$$

where P_∞ is the free-stream pressure. This equation can be simplified by using mach number instead of speed,

$$M_\infty = U/a_\infty. \qquad (4\text{-}32)$$

The speed of sound a_∞ is given by Equation (3-12)

$$a_\infty = \sqrt{\frac{\gamma P_\infty}{\rho_\infty}} = \sqrt{287\gamma T_\infty} \qquad (4\text{-}33)$$

where T_∞ is freestream temperature and all units are MKS.

Substituting Equations (4-32) and (4-33) into Equation (4-31) yields

$$\sigma^2 = \frac{\sqrt{\pi}}{4}\,K^2\rho_\infty{}^2 aLM_\infty{}^4 C_p{}^2. \qquad (4\text{-}34)$$

Equation (4-34) predicts the wavefront variance when the fluctuating pressure coefficient Cp is known. It will be shown shortly how this equation can be applied to the TBL problem.

Turbulent Boundary Layer

The purpose of this subsection is to present a brief description of the turbulent boundary layer and then to apply the Stine-Winovich experimental data to the average OTF and σ^2 models (Equations (4-17) and (4-34)).

Description. Consider a thin flat plat immersed in a fluid moving parallel to the plate surface at speed U as shown in Figure 27. A Cartesian coordinate system is defined by letting the x-axis lie along the top of the plate in the direction of

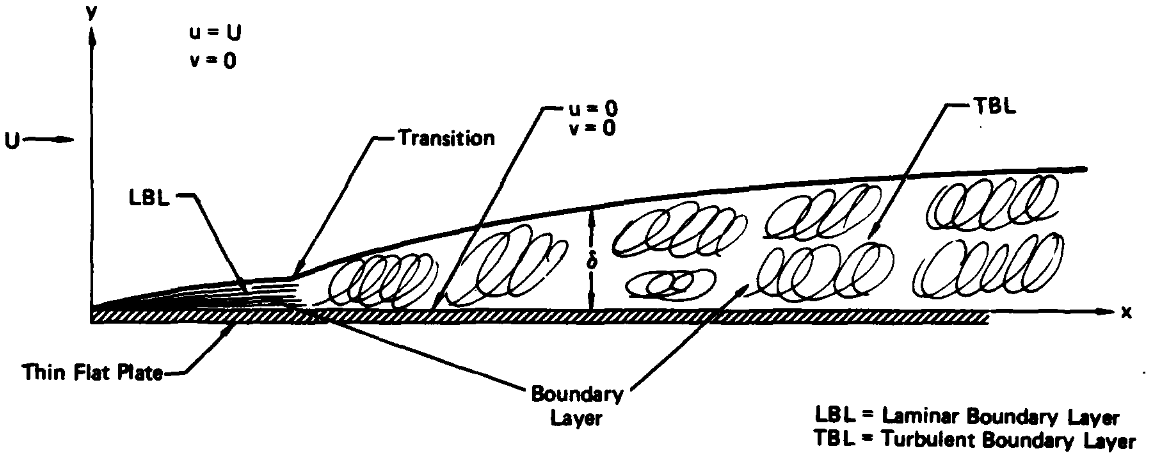

FIGURE 27
TURBULENT BOUNDARY LAYER ON A FLAT PLATE

GP74-0200-27

the fluid flow and by letting the y-axis be perpendicular to the plate, intersecting the x-axis at the leading edge. We let u and v represent the x and y fluid velocity components respectively. From the definition of the problem the velocity components have the values

$$u = U \quad \text{and} \quad v = 0 \tag{4-35}$$

at large distances from the plate. On the surface of the plate, however, friction imposes the "no slip" condition on the fluid,

$$u = v = 0. \tag{4-36}$$

Most of the necessary velocity change takes place in a very narrow region just outside the plate surface. This region is called the boundary layer. In Figure 27 the thickness of the boundary layer is greatly exaggerated and the boundary layer on the bottom of the plate is not shown. Near the leading edge of the plate, the velocity change is smooth with distance away from the plate, and the vertical velocity component is negligible. Under these conditions we say that the boundary layer is laminar. This laminar boundary layer gradually increases in thickness with distance from the leading edge. At some point behind the leading edge, the boundary layer may become turbulent. Random variations occur in the velocity components u and v and in the density ρ. In addition the rate of thickness increase with distance from the leading edge is larger than that of the laminar boundary layer.

The transition from laminar to turbulent occurs at a position corresponding to a Reynolds number in the range

$$3 \times 10^5 < R_x < 3 \times 10^6 \tag{4-37}$$

where the characteristic length associated with the Reynolds number is the distance from the leading edge.[10] All other parameters associated with the Reynolds number are taken at freestream. The Reynolds number is given by

$$R_x = \frac{\rho_\infty U X}{\mu_\infty} \tag{4-38}$$

where X is distance from the leading edge and μ_∞ is the freestream coefficient of viscosity. Since transonic aircraft have Reynolds numbers on the order of 1×10^8 per meter, the boundary layer will be turbulent almost everywhere.

The effect of friction on the speed of the air is greatest at the interface between the plate and the air, and this effect decreases rapidly with distance from the plate. The question arises as to how to define the boundary layer thickness δ. The general practice is to define δ as that distance from the plate at which the average horizontal velocity component is equal to 99% of the main-stream speed. That is,

$$\bar{u}(y = \delta) = 0.99U. \tag{4-39}$$

Although δ is called the boundary layer thickness, other types of thicknesses have been defined. One example is the displacement thickness $\delta*$, which is defined by

$$\delta* = \int_0^{\delta} 1 - \frac{\overline{\rho}_y \mu}{\rho_\infty U} \, dy \tag{4-40}$$

where $\overline{\rho}_y$ is the average density inside the boundary layer at the distance y above the plate. Falkner[16] has proposed a model for turbulent boundary layers with Reynolds numbers between 10^5 and 10^{10}. According to this model, δ and $\delta*$ are given respectively by

$$\delta = \frac{0.1285\ X}{R_x^{1/7}} \tag{4-41}$$

and

$$\delta* = \frac{0.0214\ X}{R_x^{1/7}} = \frac{1}{6}\,\delta. \tag{4-42}$$

Equation (4-41) enables us to estimate the optical path length L through the TBL by setting it equal to δ.

$$L = \delta \tag{4-43}$$

Likewise, Equation (4-42) enables us to estimate the correlation length a. According to Lyon[17] the spatial scale of the fluctuating pressure on the skin of aircraft is approximately equal to the boundary layer displacement thickness $\delta*$. Since the density variations are assumed to be directly related to the pressure variations according to Equation (4-29), the fluctuating-density spatial scale and the fluctuating-refractive-index spatial scale are also approximately equal to $\delta*$. Figure 28, which plots the Gaussian covariance function given by Equation (4-15), shows that the spatial scale is approximately equal to 3a; that is,

$$\delta* = 3a \tag{4-44}$$

or

$$a = \frac{\delta}{18}. \tag{4-45}$$

Now from Equations (2-54), (4-38), (4-41), (4-43), and (4-45) we can write the following equations for L and a.

$$L = 0.0147\ X^{6/7} T_\infty^{\ 3/28} \rho_\infty^{\ -1/7} U^{-1/7} \tag{4-46}$$

$$a = L/18 \tag{4-47}$$

All units are MKS.

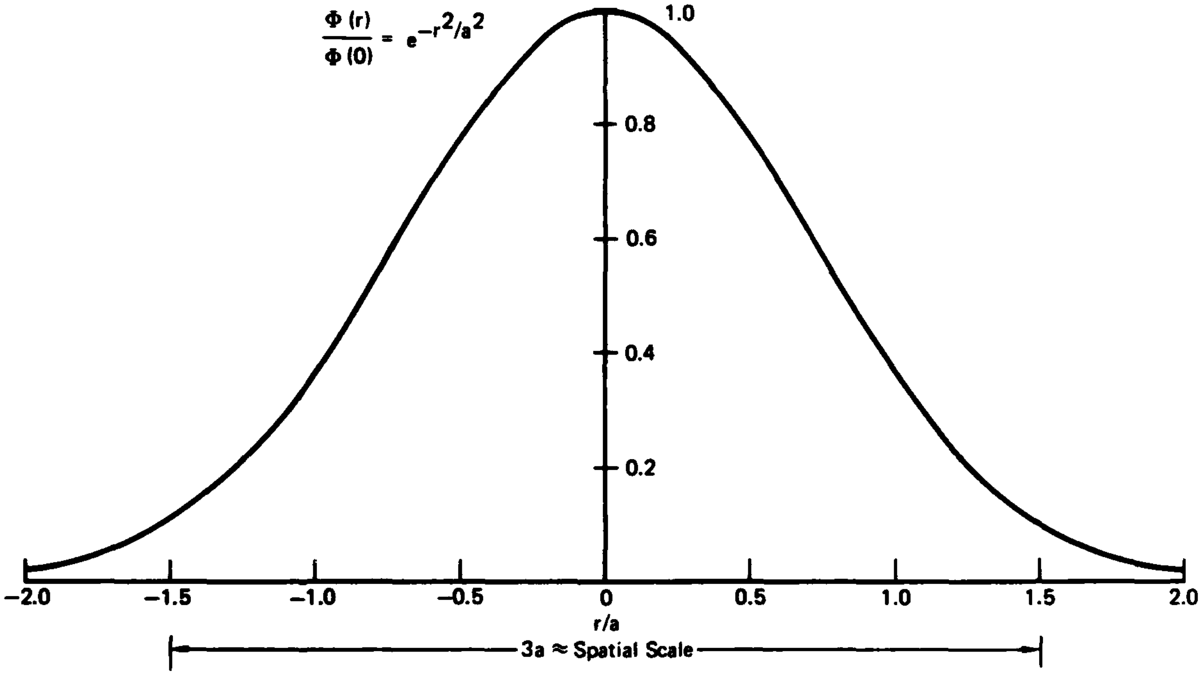

GP74-0200-28

FIGURE 28
GAUSSIAN AUTOCORELATION FUNCTION

It must be remembered here that Equation (4-46) applies only to flat plates, and even so it is only an approximation. Since analyses on other shapes are not available, however, this equation must serve as an estimate for aircraft when no other information about the TBL thickness is available. On shapes other than a flat plate the distance X would be the distance along the skin from the leading edge or point.

Although Equations (4-46) and (4-47) give estimates of L and a, Equation (4-34) shows that C_p is still needed. Fortunately C_p is known to be fairly constant for subsonic aircraft TBL's. The value quoted by Lyon[17] and confirmed by F-4 flight tests is

$$C_p = 0.006. \tag{4-48}$$

Apparently we now have a method of evaluating σ^2 and a by using Equations (4-34), (4-46), (4-47), and (4-48). The results of the Stine-Winovich experiment, which will be described presently, show that this method is essentially correct but that some changes in the equations are necessary. Readers interested in a more detailed description of turbulent boundary layers are referred to Reference 10.

Stine-Winovich Experiment.[5] The purpose of this wind tunnel experiment was to measure the optical effect of the turbulent boundary layers which formed on the wind tunnel walls. The experiment was conducted at the Ames Aeronautical Laboratory, Moffet Field, California in the one-by-three-foot supersonic tunnel No. 1. Figure 29 shows the experimental arrangement. Light from a tungsten-filament source is collected by a lens and passes through a 0.00025-inch diameter source aperture at the focus point. The light is collimated by an f/8.6 Newtonian telescope with a 21.45 inch focal length and projected across the wind tunnel through plane windows. On the other side of the tunnel the light is focused by a second Newtonian telescope, identical to the first. One of several circular collection apertures is placed at the focus point of the second telescope. The radiant power of the light passing through the collection aperture is measured with a photometer and the intensity of the tungsten source is monitored with an electronic photometer. The TBL thickness was found by using a hot wire anemometer. Measurements were made for the normal TBL with a thickness of about 1/10 foot and for an artificially thickened TBL with a thickness of about 2/10 foot. The thickening was accomplished by applying a roughness coating to the side walls of the tunnel to within 40 inches of the windows. Figure 30 shows the positions of the anemometer probe and the roughness coating relative to the window.

The analytic approach taken by Stine and Winovich was, in this writer's opinion, inadequate. However, there is no reason why their experimental data should not be used to examine our model for the average OTF of a TBL.

Appendix F shows that the average theoretical ratio $\overline{Q}$ of the radiant power emerging from the collection aperture to that emerging from the source aperture is given by

$$\overline{Q} = \int_0^{\frac{2\pi D r_b}{f\lambda}} \tau_0\left(\frac{u}{2\pi r_b}\right)\left[\overline{\tau}_R\left(\frac{u}{2\pi r_b}\right)\right]^2 J_1(u)\, \frac{2J_1\left(u\,\frac{r_a}{r_b}\right)}{u\,\frac{r_a}{r_b}}\, du \tag{4-49}$$

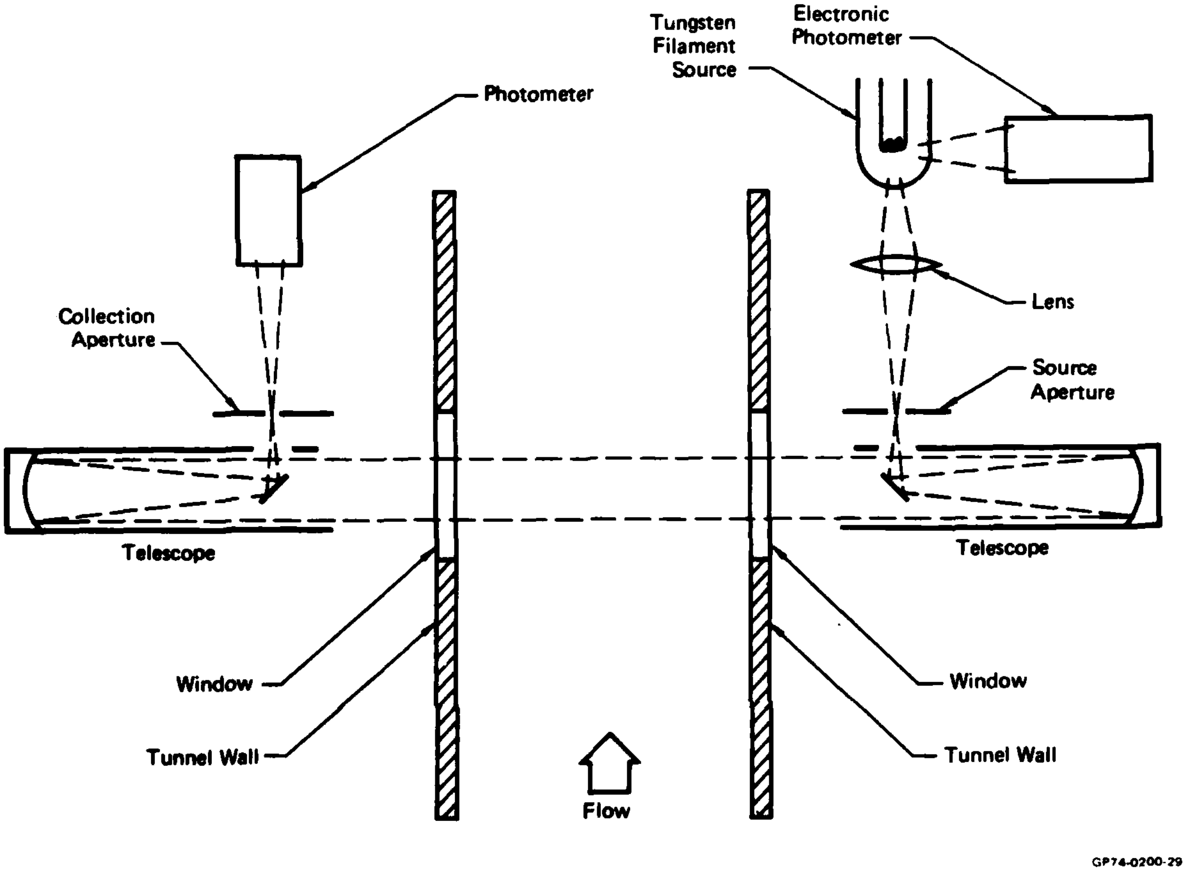

FIGURE 29
STINE-WINOVICH EXPERIMENTAL ARRANGEMENT

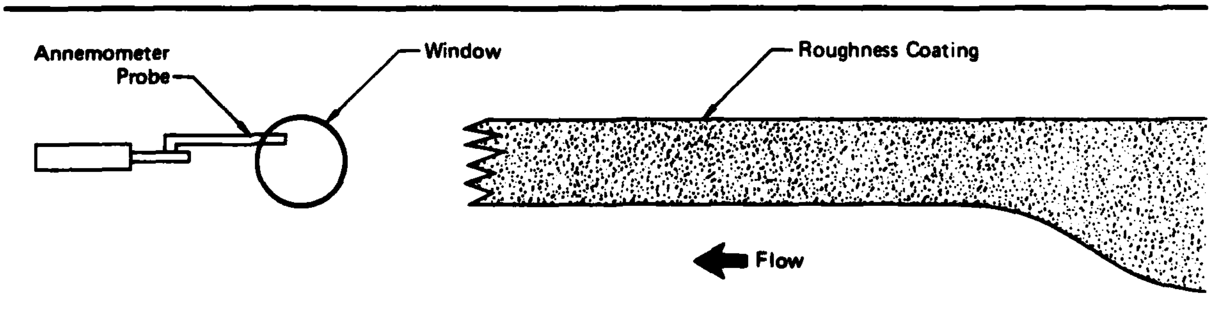

FIGURE 30
VIEW OF WIND-TUNNEL WALL FOR STINE-WINOVICH EXPERIMENT

where

D = telescope aperture diameter

f = telescope focal length

r_a = radius of source aperture

r_b = radius of collection aperture

J_1 = first order Bessel function of first kind

The appendix shows that $\overline{\tau}_R$ is squared because the light beam must traverse two boundary layers.

The problem here is to match values of $\overline{Q}$ computed from Equation (4-49) and our model for $\overline{\tau}_R$ with the values of $\overline{Q}$ measured in the experiment. Values of $\overline{Q}$ were measured for various mach numbers and densities for both the natural boundary layer and the artificially thickened boundary layer. Equation (4-49) was evaluated by using Equations (2-7), (2-35), (4-17), (4-34), (4-43), (4-47), and (4-48). Although the Newtonian telescopes had a central obscuration, the diameter of which was one-tenth the aperture diameter, the diffraction OTF of a circle can be used with negligible error. Figure 31 shows a comparison of the diffraction OTF's for a circular aperture and for the center-blocked circular aperture.

Figure 32 shows both the measured and computed values of $\overline{Q}$ vs r_b for the highest density and mach number. The computed values are represented by the dashed line. Obviously the experimental values are much lower than the corresponding computed values. The implication is that the actual $\overline{\tau}_R$ is much lower than we would predict. A good match can be achieved, however, with only minor changes to our model. Specifically, the coefficient in Equation (3-47) is changed from 1/18 (0.056) to 0.08 and the value of C_p is changed from 0.006 to 0.05.

$$a = 0.08\delta = 0.08L \qquad (4\text{-}50)$$

$$C_p = 0.05 \qquad (4\text{-}51)$$

The solid line shows a plot of $\overline{Q}$ vs. r_b which was computed by using Equations (4-50) and (4-51) instead of Equations (4-47) and (4-48). This plot shows good agreement between the computed and measured values of $\overline{Q}$. Figure 33 shows plots of $\overline{Q}$ vs. r_b using the new Equations for various values of mach number, density and boundary layer thickness.

By substituting Equations (2-7), (4-43), (4-50), and (4-51) into Equation (4-34), the variance σ^2 may now be expressed as

$$\sigma^2 = 4.4 \times 10^{-12} \delta^2 \rho_\infty{}^2 M_\infty{}^4 . \qquad (4\text{-}52)$$

All units are MKS. For a flat plate Equations (4-32), (4-33), (4-43), and (4-46) may be substituted into Equation (4-52) to yield

$$\sigma^2 = 4.04 \times 10^{-16} \rho_\infty{}^{12/7} T_\infty{}^{1/14} M_\infty{}^{26/7} X^{12/7} . \qquad (4\text{-}53)$$

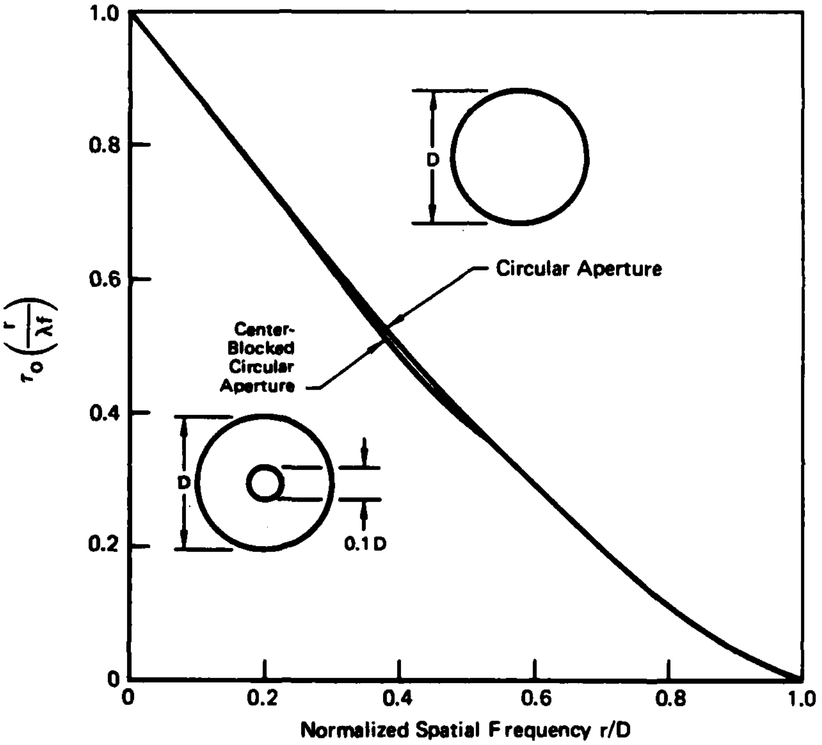

FIGURE 31
COMPARISON OF DIFFRACTION OTF'S FOR A CIRCULAR APERTURE AND FOR A CENTER-BLOCKED CIRCULAR APERTURE

GP74-0200-31

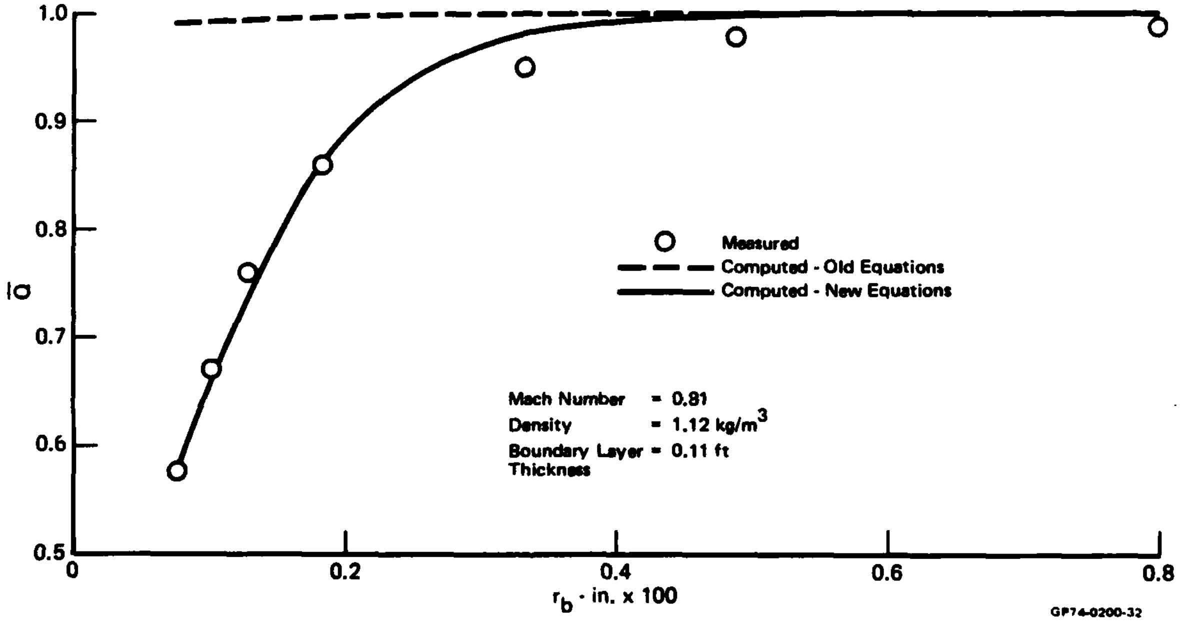

FIGURE 32
MEASURED AND COMPUTED VALUES OF $\overline{Q}$ vs r_b

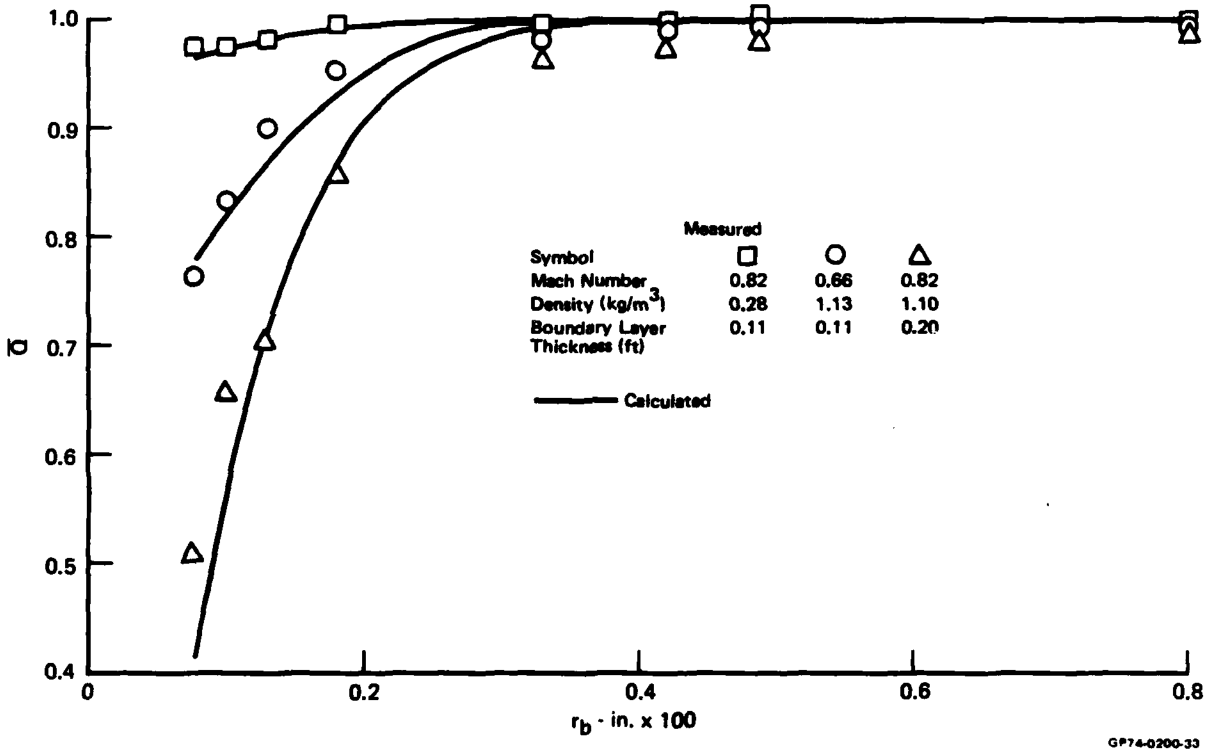

FIGURE 33
MEASURED AND COMPUTED VALUES OF $\bar{Q}$ vs r_b USING NEW EQUATIONS FOR VARIOUS VALUES OF MACH NUMBER, DENSITY, AND BOUNDARY-LAYER THICKNESS

The correlation length from Equation (4-50) becomes

$$a = 7.66 \times 10^{-4} \rho_\infty^{-1/7} T_\infty^{1/28} M_\infty^{-1/7} X^{6/7}. \qquad (4\text{-}54)$$

Again all units are MKS.

Even though the value of C_p had to be changed by an order of magnitude to make our model work, the equations for $\overline{\tau}_R$ (Equation (4-17)) and for σ^2 (Equation (4-34)) are apparently reliable. The original failure of the model should not be judged too harshly. It must be remembered that we were trying to describe density fluctuations inside the wind tunnel boundary layer from pressure fluctuations on the surface of an aircraft.

A valid criticism of the Stine-Winovich experiment is that the measured value of $\overline{Q}$ may be affected by vibration. The fact that the experimental data does agree with the model for changes in mach number, density, and boundary layer thickness indicates that the effect of vibration may well be negligible. Even if vibration did effect the experiment, the model can still be used with the understanding that 0.05 is an upper limit on C_p. Besides the vibration problem, there is the fact that the OTF is valid only for monochromatic light. It is this writer's belief, however, that the model for the turbulent boundary layer OTF presented in this section is the best one available. An accurate model must await direct MTF measurements under controlled test conditions.

Separated Flow

Treatment of separated flow in this subsection is similar to the treatment given TBL's in the last subsection. After a general description of separated flow, data from the RF-4C wind tunnel test is used to evaluate σ^2 and a for the average separated flow MTF.

Description.[10] Consider the surface in Figure 34 which has a steady convex curvature, the surface curving away from the direction of flow. In this situation the mainstream flow is retarded and the pressure increases in the direction of the flow. It can be shown that static pressure is essentially constant across the boundary layer; that is

$$\frac{\partial \overline{P}}{\partial y} = 0 \qquad (4\text{-}55)$$

inside the boundary layer. This condition implies that static pressure inside the boundary layer increases in the direction of flow.

$$\frac{\partial \overline{P}}{\partial x} > 0 \qquad (4\text{-}56)$$

The fluid element ABCD will have an average pressure $\overline{P}$ on the AD side and an average pressure $\overline{P} + (\partial \overline{P}/\partial x)\ \delta x$ on the BC side. The resultant pressure force, in addition to friction, will slow the element. The deceleration is greatest near the surface where the element is remote from the mainstream. The figure shows the change in the average velocity profiles. The deceleration of the fluid implies that the boundary layer must thicken to conserve mass. At some point S on the surface the velocity gradient $\partial \overline{u}/\partial y$ vanishes. Beyond this point reverse flow may occur as shown in the

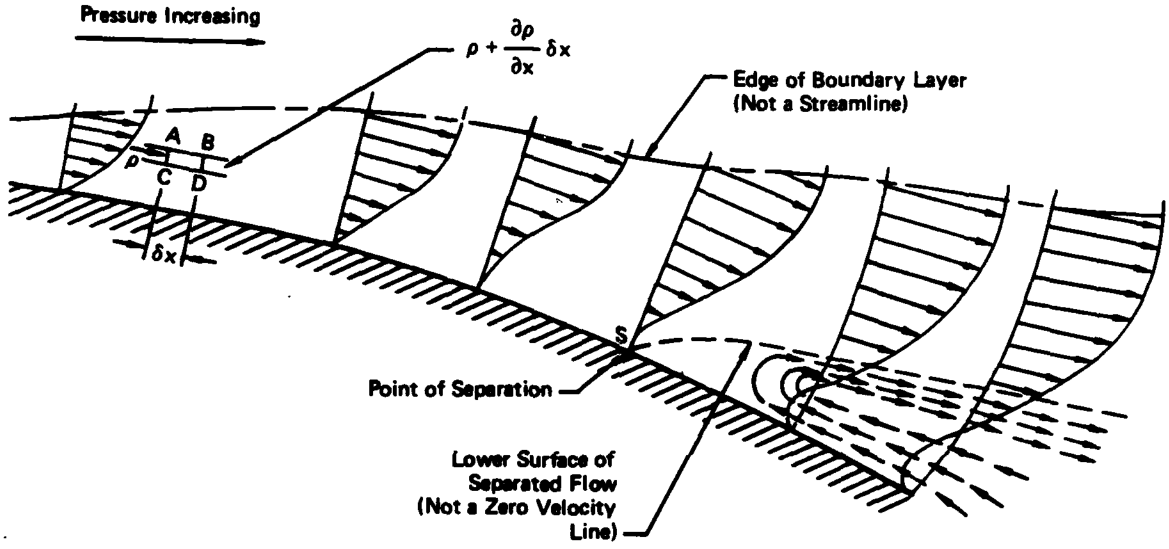

GP74-0200-34

FIGURE 34
FLOW SEPARATION[10]

figure. The dotted line extending from S in the downstream direction is drawn such that the mass flow rate between it and the edge of the boundary layer is equal to the boundary layer mass flow rate upstream of S. The boundary layer actually separates from the surface with the region below the dotted line being the separated-flow region.

RF-4C Wind Tunnel Test. The purpose of this test was to measure the effect of the separated flow field behind the RF-4C nose chin on photographic resolution. The test was conducted in the transonic Propulsion Wind Tunnel 16T at the Arnold Engineering Development Center, Arnold Air Force Station, near Tullahoma, Tenn. Figure 35(a) shows the experimental setup. A model of the bottom half of the RF-4C nose with a Chicago Aerial CA-120 camera, is mounted on a splitter plate. Both full scale and fifth scale models were used. The camera took pictures of a standard Air Force resolution bar target through a collimator mounted in the wind tunnel ceiling. The camera was equipped with a Xenotar 6-inch lens and the film used was Kodak 3414. The target contrast was 1000:1. The external square aperture stop was mounted diagonally with respect to the direction of flow and with respect to the resolution bars as shown in Figure 35(b). Runs were made for various exposure times, aperture settings, air densities, and mach numbers to determine optimum exposure times and aperture settings for different flight conditions.

Although the RF-4C Wind Tunnel Test was not designed for MTF computations, a portion of the image resolution data can be used to develop simple models for σ^2 and a to be used in Equation (4-17).

1. Background. In Section II it was shown that the image of a sinusoidal target of modulation C_0 is a sinusoid of modulation C_1 given by

$$C_1 = C_0 |\tau(\nu)|, 0 \leq C_0 \leq 1 \qquad (4\text{-}57)$$

where $|\tau(\nu)|$ is the MTF of the imaging system. Normally the system would include the boundary flow, aperture, and lens. In this particular case, however, lens degradation is insignificant. We now define system resolution as the largest spatial frequency ν_{max} at which the image can be resolved for the given value of C_0. Becuase the film in the camera and the eye of the individual recording the resolution are not optically perfect, ν_{max} is always less than ν_0, the spatial frequency at which τ vanishes.

$$T(\nu_0) = 0 \qquad (4\text{-}58)$$

$$\nu_{max} < \nu_0 \qquad (4\text{-}59)$$

In order to find ν_{max} threshold modulation (TM) is introduced. The TM is defined as the lowest value of C_1 for which a target of a given spatial frequency can be resolved. Figure 36 shows a typical TM plotted as a function of spatial frequency. The TM is a function of the film and the human recorder. From the definition of TM and Equation (4-57) we see that as long as the product $C_0 |\tau(\nu)|$ is greater than $TM(\nu)$, the image can be resolved. At $\nu = \nu_{max}$ we have

$$TM(\nu_{max}) = C_0 |\tau(\nu_{max})| . \qquad (4\text{-}60)$$

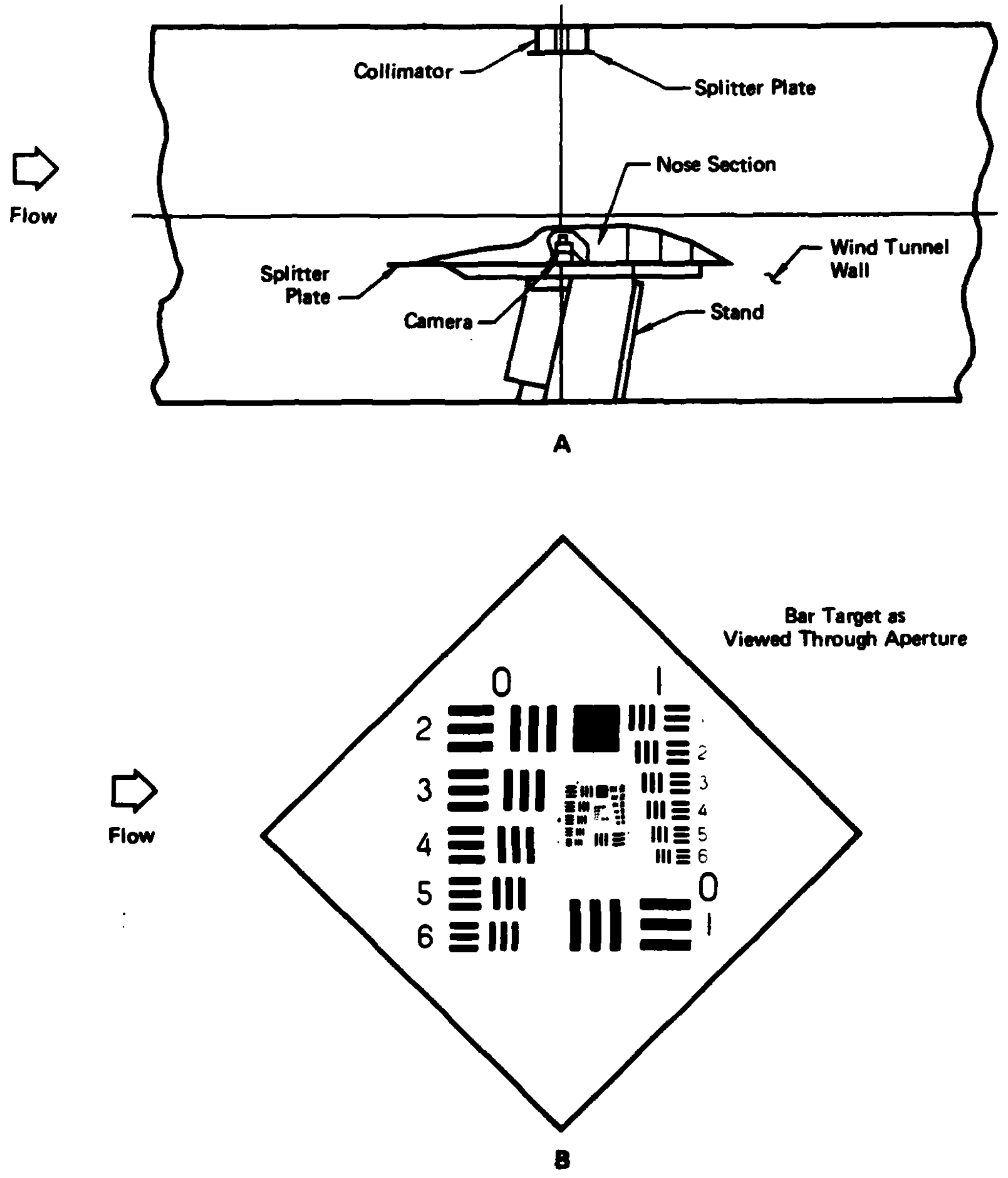

GP74-0200-35

FIGURE 35
EXPERIMENTAL ARRANGEMENT FOR RF-4C WIND-TUNNEL TEST

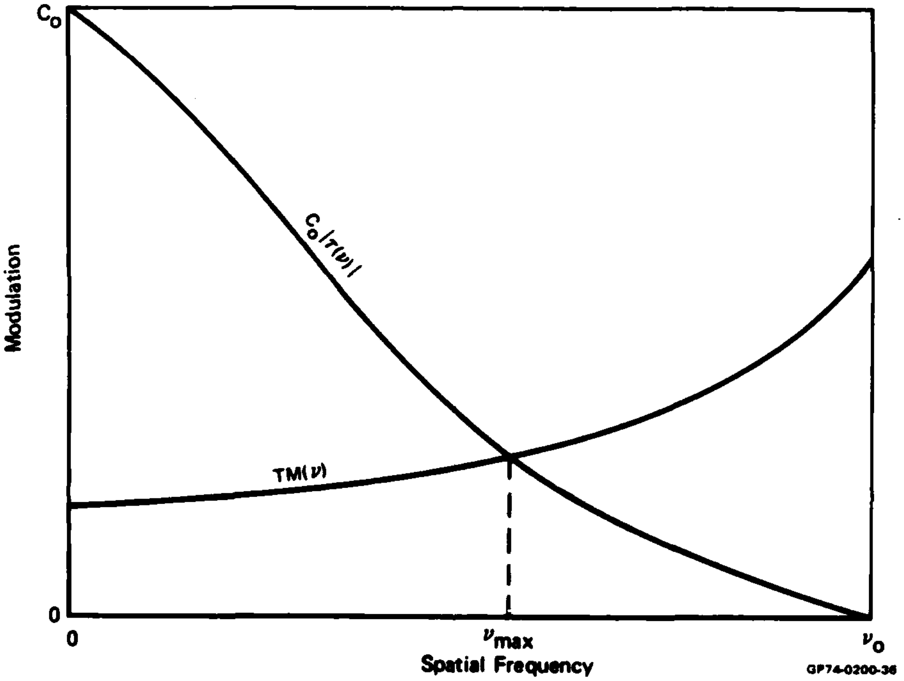

FIGURE 36
RELATIONSHIP BETWEEN MTF, TM, AND SYSTEM RESOLUTION

If the MTF is factored into its diffraction and random parts, Equation (4-60) may be written

$$\bar{\tau}_R(\nu_{max}) = \frac{TM(\nu_{max})}{C_0\tau_0(\nu_{max})} . \tag{4-61}$$

In analyzing the RF-4C test, τ_0 and TM are known as are values of ν_{max} for some particular conditions. For all practical purposes the target modulation for the 1000:1 target is one.

$$C_0 = \frac{1000 - 1}{1000 + 1} \doteq 1 \tag{4-62}$$

Using this information we model σ^2 and a in Equation (4-17) for $\bar{\tau}_R$ such that Equation (4-61) is satisfied. Although the target in the test was a rectangular-bar target instead of a sinusoidal target, it was felt that the accuracy in determining ν_{max} would be sufficient for this analysis.

Equation (4-61) shows that expressions for TM and τ_0 are needed. Lauroesch et al. have found that a good model for the TM is

$$TM(\nu) = b_0 + b_1\nu^2 \tag{4-63}$$

where b_0 and b_1 are constants.[18] The b_0 term is not a function of the film but of the human observer. As spatial frequency increases from zero, the film MTF and grain noise become increasingly important as indicated by the $b_1\nu^2$ term. The value of b_0 is approximately 0.03. The constant b_1 for Kodak 3414 film is found by solving Equation (4-63) for b_1 and using the data point TM = 0.231 for ν = 250 mm^{-1} or lines/mm.[19]

$$b_1 = [TM(\nu) - b_0]/\nu^2 = 3.22 \times 10^{-6} mm^2 \tag{4-64}$$

Equation (4-63) is now

$$TM(\nu) = 0.03 + 3.22 \times 10^{-6}\nu^2 \tag{4-65}$$

where ν is in lines/mm. The expression for τ_0 is found by using Equations (2-32) and (2-25).

$$\tau_0(\nu_x,\nu_y) = \left(1 - \frac{\nu_x\lambda f}{D_x}\right)\left(1 - \frac{\nu_y\lambda f}{D_y}\right), \; 0 \le \nu_x \le \frac{D_x}{\lambda f}, \; 0 \le \nu_y \le \frac{D_y}{\lambda f} \tag{4-66}$$

This equation can be simplified by recognizing that $D_x = D_y$ and defining

$$B = \frac{\lambda f}{D_x} = \frac{\lambda f}{D_y}. \tag{4-67}$$

Equation (4-66) becomes

$$\tau_0(\nu_x,\nu_y) = (1 - B\nu_x)\ (1 - B\nu_y),\ 0 \leq \nu_x,\nu_y \leq \frac{1}{B} \tag{4-68}$$

With the aperture diagonal to the target, the resolution is not a value of either ν_x or ν_y but of ν, the spatial frequency along the diagonal between the x and y directions. Since displacement along the diagonal is given by

$$r = \sqrt{x^2 + y^2} = \sqrt{2}\,x = \sqrt{2}\,y, \tag{4-69}$$

the spatial frequency ν is given by

$$\nu = \sqrt{\nu_x^2 + \nu_y^2} = \sqrt{2}\,\nu_x = \sqrt{2}\,\nu_y \tag{4-70}$$

Substituting Equation (4-70) into Equation (4-68) we have

$$\tau_0(\nu) = 1 - \sqrt{2}\,B\nu + B^2\nu^2/2,\ 0 \leq \nu \leq \frac{\sqrt{2}}{B}. \tag{4-71}$$

The camera aperture setting was f/22,

$$\frac{f}{D_x} = \frac{f}{D_y} = 22. \tag{4-72}$$

Since the source was white light, the wavelength is taken as

$$\lambda = 0.55 \times 10^{-3}\ \mathrm{mm}\ . \tag{4-73}$$

Substituting Equations (4-72) and (4-73) into Equation (4-67) gives B,

$$B = 0.0121\ \mathrm{mm}, \tag{4-74}$$

and Equation (4-71) becomes

$$\tau_0(\nu) = 1 - 0.0171\ \nu + 7.32 \times 10^{-5}\nu^2. \tag{4-75}$$

Equations (4-65) and (4-75) are the expressions needed for TM and τ_0 respectively. Plots of these equations are shown in Figure 37. We are now in a position to look at the test data.

2. <u>Data</u>. Most of the data collected during the test is eliminated from the analysis because of the two following considerations. First, we are interested in the average of the random MTF, and therefore only data related to the longest exposure times for each configuration is considered. Second, it is necessary to know the MTF of the lens if the lens introduces significant degradation. At the f/22 aperture setting, performance was nearly diffraction limited, but at smaller f numbers the lens produced significant degradation. Since the MTF of the lens at the various f numbers is unknown, only data from the f/22 aperture settings

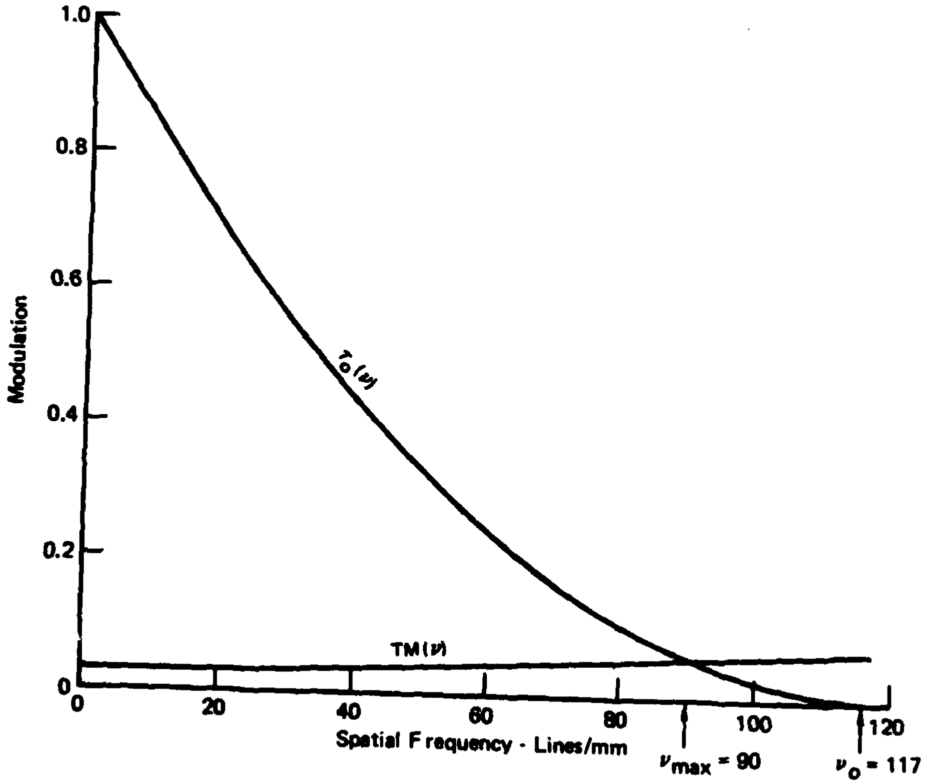

FIGURE 37
DIFFRACTION OTF AND TM FOR THE RF-4C WIND-TUNNEL TEST

GP74-0280-37

are analyzed. Table I below lists the resolution data considered.[1] Each resolution given is the average resolution for ten exposures.

Table I IMAGE RESOLUTION (LINES/MM) FOR RF-4C WIND TUNNEL TEST

Scale	Full	Full	1/5
Pressure altitude (ft)	8,000	40,000	8,000
Exposure time (sec)	0.010	0.010	0.001
Mach Number			
.7	60		56
.8	37		
.85	39		36
.9	40	66	36
.95	35		47

The fifth-scale 40,000 ft data was not used because the random flow degradation was not significant. The data in Table I shows that no strong correlation exists between Mach number and resolution for Mach numbers between .8 and .95. Since optical degradation is greatest in this Mach range, only data from this range was used, and Mach number was excluded as a variable.

A possible explanation for the lack of correlation may be that there was little change in the actual air speed in the vicinity of the flow separation. The shock wave in front of the flow separation shown in Figure 1 indicates that the air has been accelerated to some supersonic speed before reaching the shock wave. A property of shock waves is that the flow deceleration through a shock wave increases with an increase of flow speed into the shock wave. It is therefore reasonable to expect that changes in the actual flow Mach number in the vicinity of separated flow are not as great as the changes in the freestream Mach number.

Table II shows the data used in the analysis.

Table II DATA USED IN ANALYSIS OF RF-4C WIND TUNNEL TEST

Scale	Full	Full	1/5
Pressure Altitude	8,000	40,000	8,000
ν_{max} (mm^{-1})	39	66	36
$\bar{\tau}_0(\nu_{max})$	0.444	0.190	0.479
$TM(\nu_{max})$	0.0305	0.0314	0.0304
$\bar{\tau}_R(\nu_{max})$	0.0687	0.1657	0.0635
L(m)	0.1	0.1	0.02
ρ_∞ (kg/m^3)	0.882	0.221	0.882

The optical path length (flow separation thickness) was determined from Schlieren photographs. The density was found by using Equation (2-3). The pressure used is taken from the ARDC model atmosphere[20] for the given altitude, and the temperature was taken as 297°K.

3. Results. Equation (4-20) shows that σ^2 is a function of L, a, and the variance of refractive index $\overline{\mu^2}$. Unfortunately we do not have a good model for $\overline{\mu^2}$ in a separated flow. It is, however, reasonable to assume that $\overline{\mu^2}$ increases with freestream density. We now have the problem of writing σ^2 and a as functions of ρ_∞ and L such that Equation (4-61) is satisfied for each of the three configurations in Table II. The turbulent boundary layer model in which σ^2 is proportional to $L^2\rho_\infty^2$ does not work. A model which does work, however, is

$$a = 0.067\ L \tag{4-76}$$

$$\sigma^2 = 1.2 \times 10^{-12}\ \rho_\infty L \tag{4-77}$$

All units are MKS. These two equations along with Equation (4-17) consititute our model for the average separated-flow OTF. Figure 38 plots the resulting average OTF's (including both separated flow and diffraction) for the three configurations and the TM. The resolution data points ν_{max} from Table II are also shown.

As with the MTF model for a TBL, there is doubt as to the accuracy of our model for the average separated-flow OTF. But again, it is this writer's belief that the model presented here is the best that can be found. The best hope of achieving accurate models for the TBL and separated flow is to take direct random-flow MTF measurements with a shearing interferometer under controlled conditions. The feasibility of such measurements has already been demonstrated by Kelsall.

The Shearing Interferometer

The purpose of this subsection is to present a description of the shearing interferometer and its use by Kelsall in aircraft flight tests. Although several complications make it impossible to properly analyze the resultant data, the experiment is important because Kelsall has demonstrated the feasibility of making direct measurements of the boundary-flow MTF.

Corner-Cube Shearing Interferometer. The shearing interferometer is an interferometer which can be used to directly measure MTF's. Figure 39 is a simplified diagram of a corner-cube shearing interferometer introduced by Hopkins.[21] After passing through an aperture the incident beam is divided by a beam splitter. The waves are then each reflected by a corner-cube retroreflector and superimposed at the beam splitter with a lateral shear x. The power produced by the superimposed beams is recorded. To guarantee that the two wavefronts are in phase, one of the corner-cubes may be driven forward and back over several wavelengths. The power output will then consist of an ac signal corresponding to the overlapping portion of the wavefronts and a dc signal corresponding to the power that would be received if there were no overlap. When the ac signal is at its maximum, the wavefronts are exactly in phase. Kelsall has shown that the amplitude of the ac signal is proportional to the MTF, $\tau(x/\lambda f)$, associated with the incoming wavefront.[22] The radiant output power pow of the interferometer is given by

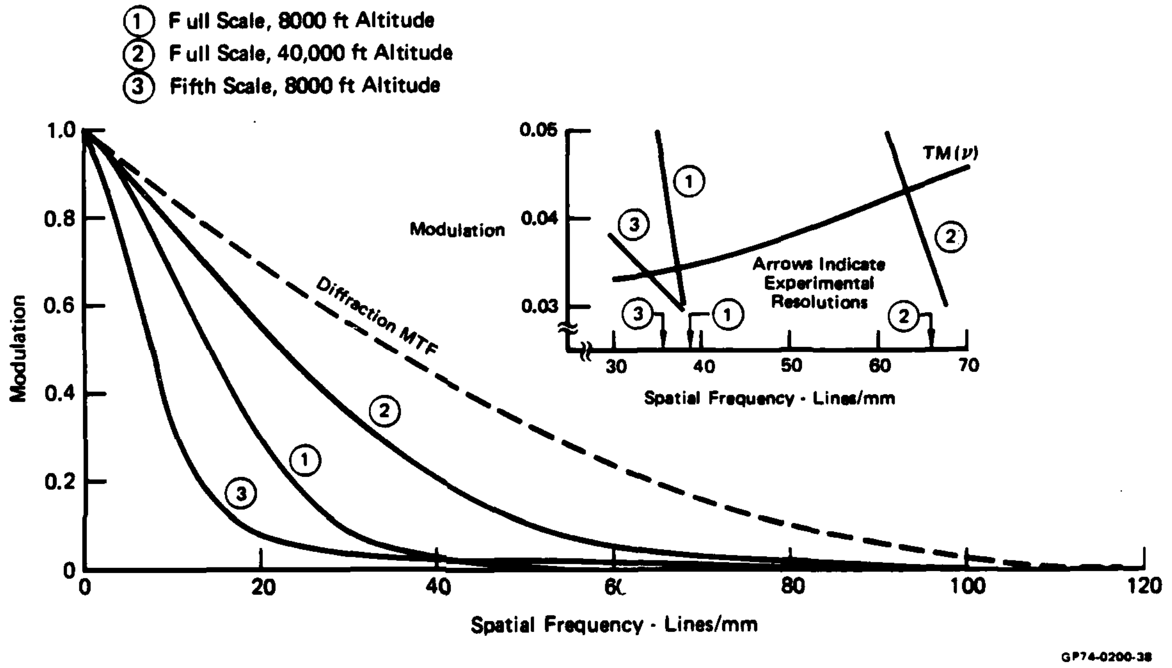

FIGURE 38
AVERAGE OTF'S FOR THE THREE RF-4C-WIND-TUNNEL-TEST CONFIGURATIONS

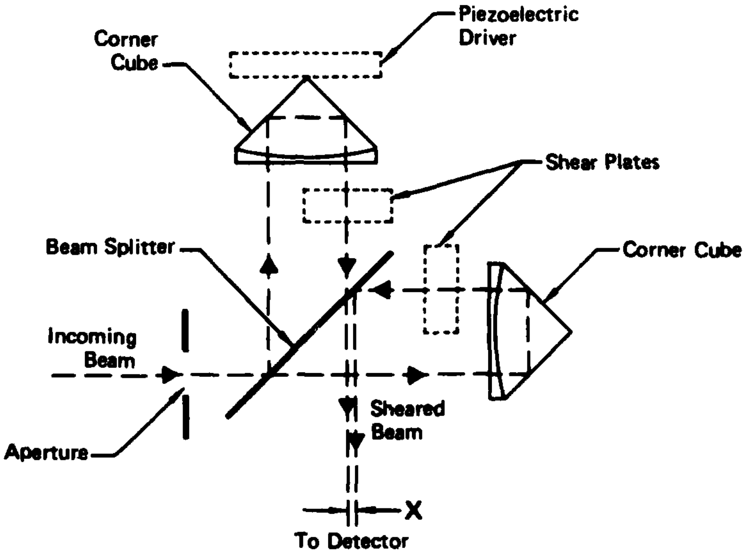

FIGURE 39
BASIC DESIGN OF A CORNER-CUBE SHEARING INTERFEROMETER

GP74-0200-39

$$\text{pow} = \alpha + \beta \left|\tau\left(\frac{x}{\lambda f}\right)\right| \cos\left[\phi(x) + \omega_p t\right] \qquad (4\text{-}78)$$

where α and β are constants ($\beta \leq \alpha$), ϕ is a phase term which includes the OTF phase, and ω_p is the angular frequency of the relative phase of the two wavefronts. Figure 40 shows plots of power vs time for various shear values, x/D, where D is aperture diameter. In Figure 40(a) the wavefront coming into the interferometer is constant in time, and in Figure 40(b) the incoming wavefront varies in time as would a wavefront passing through a TBL or separated flow region.

The average MTF for a particular spatial frequency is found by taking the average ac power amplitude for the corresponding value of x and normalizing it such that the normalized ac power amplitude at x = 0 is unity.

Kelsall's derivation examines the effects of finite bandwidth, inequality of power of the two beams, and partial incoherence caused by unequal beam paths. All of these effects increase the dc power level and decrease the ac power amplitude, but the MTF is still proportional to the ac power amplitude. A simpler derivation which does not examine these effects but deals only with the basic principle of the shearing interferometer is presented in Appendix G.

<u>Kelsall's Experiment</u>. The corner-cube shearing interferometer used by Kelsall is described in Reference 23. The corner-cube which moves forward and back to produce the phase shift between the wavefronts is driven by a piezo-electric device. Two identical glass plates are placed in the return paths from the corner-cubes to the beam splitter. By turning these plates simultaneously through a drum belt coupling, the shear x can be adjusted. These shear plates and the piezo-electric driver are outlined with dotted lines in Figure 39.

Figure 41 shows the experimental arrangement used by Kelsall to measure the turbulent boundary layer MTF of a KC-135 aircraft.[6] The source beam from a He-Ne laser is expanded to 50 mm then reflected through the aircraft window by a plane mirror and a beam splitter. The beam is reflected back through the window by a 31 mm mirror mounted on an external airfoil 25 cm from the window. In this way the beam passes through the same boundary flow region twice. The return beam is then reduced by a 24 mm aperture telescope and passes to the shearing interferometer. A removable air path shield allows MTF measurements to be made without the boundary flow. Figure 42 shows the MTF's for the double pass. The measurements were taken at 40,000 ft altitude at normal cruising speed.

We will not attempt to analyze the results of this experiment, but some comments will be made. Obviously the MTF detected by the interferometer is not the MTF of the boundary flow since the beam makes two passes through the flow. To find the true value of $\bar{\tau}_R$ from the double pass value $\bar{\tau}_{R2}$, Kelsall assumed that $-\ln(\bar{\tau}_R)$ is proportional to the total optical path length. Using our model for $\bar{\tau}_R$, Equation (4-17), which is also used by Kelsall, the assumption implies that σ^2 is proportional to the total optical path length. The relationship between $\bar{\tau}_R$ and $\bar{\tau}_R$ would be

$$\bar{\tau}_{R2} = \bar{\tau}_R^2 \; . \qquad (4\text{-}79)$$

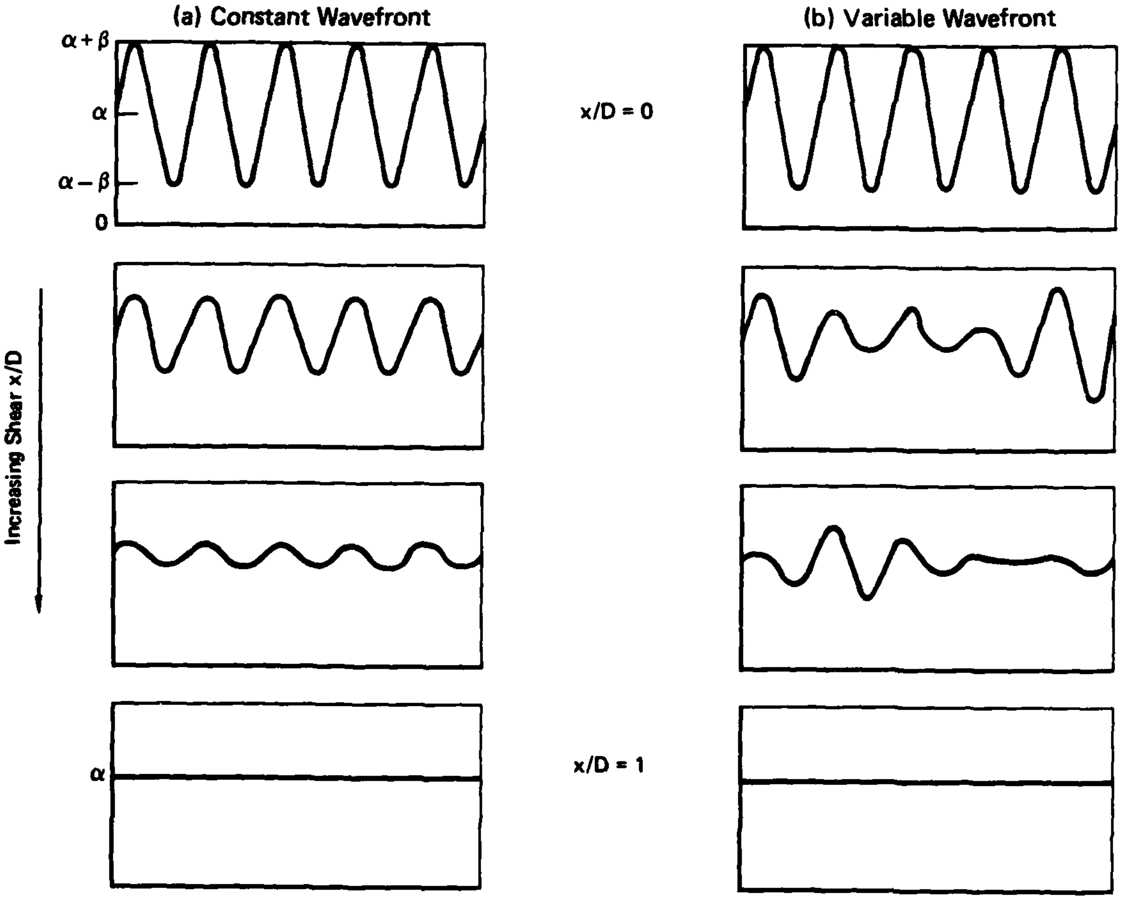

FIGURE 40
POWER vs TIME PLOTS FOR SHEARING INTERFEROMETER AT VARIOUS SHEAR VALUES

GP74-0200-40

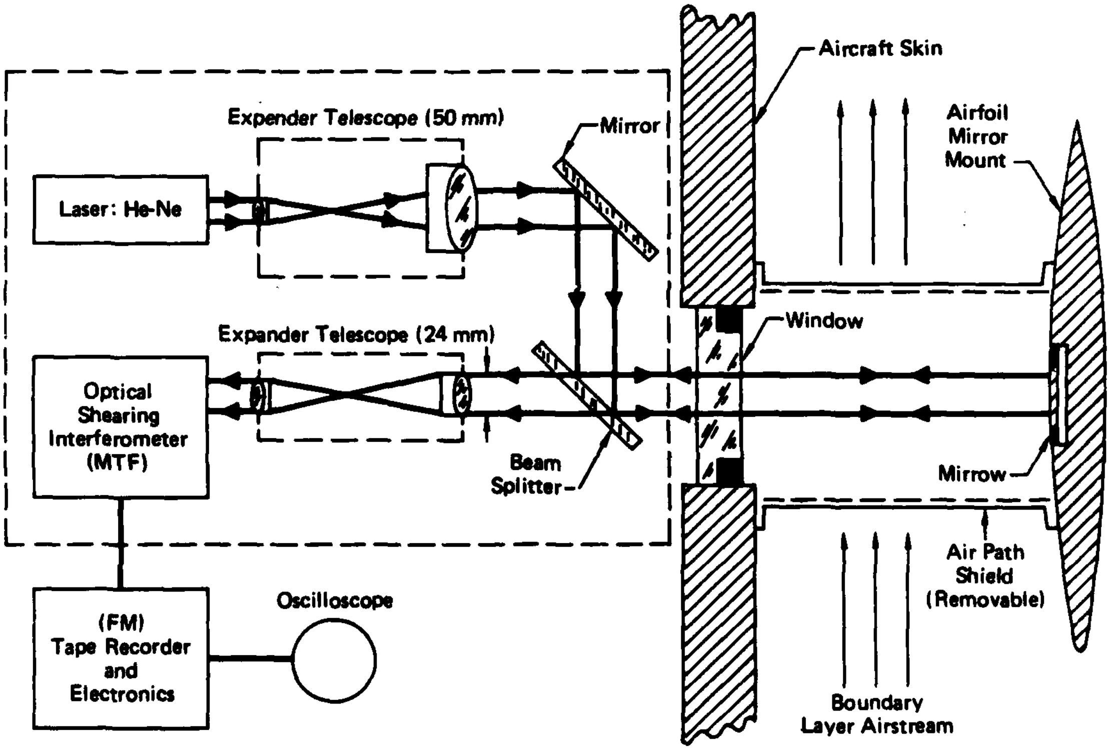

FIGURE 41
KELSALL'S EXPERIMENTAL ARRANGEMENT FOR MEASURING THE TURBULENT-BOUNDARY-LAYER MTF OF A KC-135 AIRCRAFT[6]

GP74-0200-41

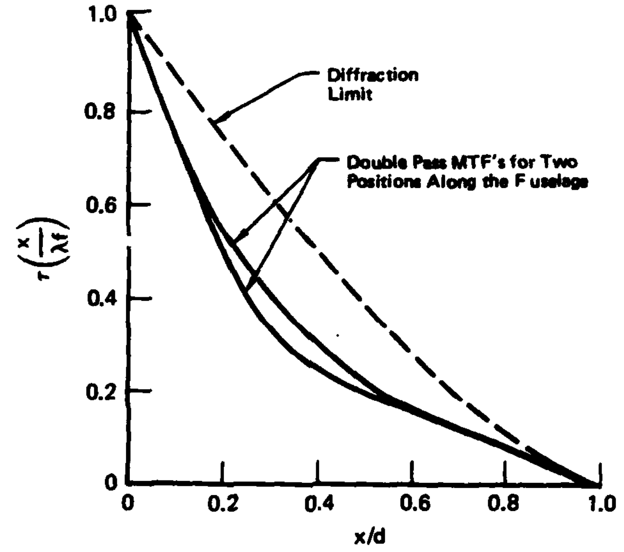

GP74-0200-42

FIGURE 42
AVERAGE MTF'S FOR DOUBLE PASS IN KELSALL'S EXPERIMENT[6]

Kelsall's assumption would be correct if the optical length of the return path of the beam were independent of the optical length of the first path. Then σ^2 for the double pass would be the variance of the sum of two independent values of Δ, a Gaussian variable. Using a law from probability theory, the σ^2 for the double pass would be the sum of the σ^2 for the two separate passes. In other words, Kelsall's assumption would be true. However, the optical lengths are not independent. In fact, if the instrumentation is properly aligned, the two optical lengths are the same, and the value of Δ is twice as large at every point for the double pass. According to Equation (4-8), σ^2 for the double pass would be four times greater than for a single pass. Therefore the relationship between $\bar{\tau}_R$ and $\bar{\tau}_{R2}$ should be

$$\bar{\tau}_{R2} = \bar{\tau}_R^{\,4} . \tag{4-80}$$

By using Kelsall's data and Equation (4-80) one should be able to find $\bar{\tau}_R$ for the KC-135 boundary flow. Kelsall also ran a wind tunnel test which was to duplicate the flight test conditions.[24] The results of the wind tunnel test showed no significant optical degradation. Several factors may be responsible for the discrepancy between the results of the flight and wind tunnel tests.

1. The optical window was mounted flush to the wall in the wind tunnel test; whereas, in the flight test the window was recessed about 1 inch.
2. In the flight test a temperature gradient of about 30°F existed between the skin and the outside air.
3. It is possible that during the flight test warm air from inside the aircraft escaped from openings in the skin forward of the test window and mixed with the boundary flow air.

All three of these factors would tend to increase degradation in the flight test. They also make a proper analysis of the results with regard to a boundary layer MTF very difficult if not impossible.

Although the discrepancy between the flight and wind tunnel test results shows that the flight test results cannot be applied to a general situation, the test is important because it shows the feasibility of making direct measurements of boundary flow MTF's.

Until now our discussion has been confined to the time average MTF. New fast shearing interferometers now make it possible to take MTF measurements almost instantaneously (~ one millisecond).

<u>Fast Shearing Interferometers</u>. There are two types of fast shearing interferometer; the first was developed by Kelsall[25] and the second was developed by workers at MCAIR. Basic designs of the two instruments are shown in Figure 43. The two designs are similar, but because the MCAIR version is easier to describe, it will be discussed first.

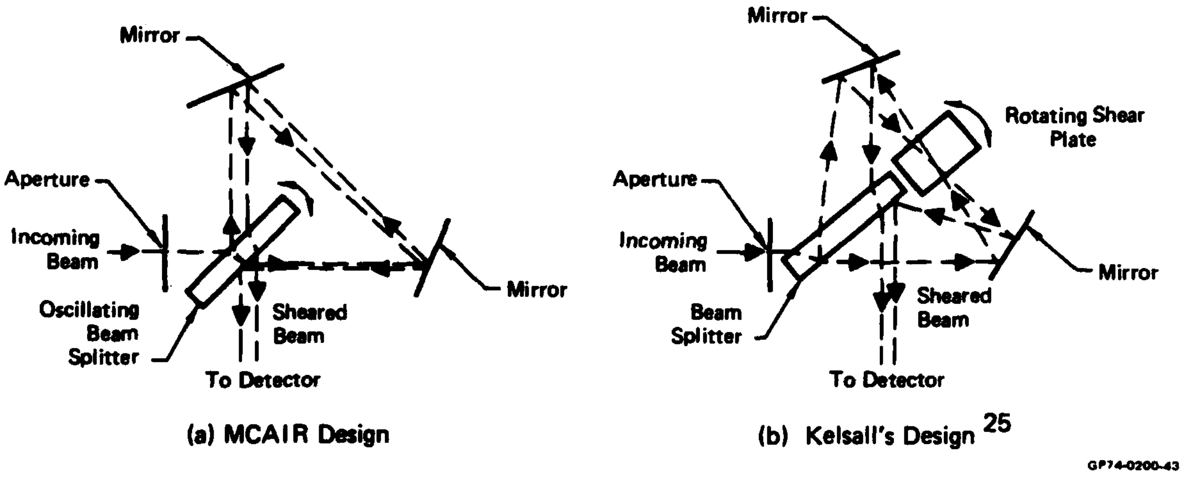

(a) MCAIR Design

(b) Kelsall's Design[25]

FIGURE 43
BASIC DESIGNS OF THE MCAIR AND KELSALL FAST SHEARING INTERFEROMETERS

As shown in the diagram of the MCAIR fast shearing interferometer, the incident beam passes through an aperture and is divided by a beam splitter. The two beams traverse, in opposite directions, the triangular path formed by the splitter and two plane mirrors. The beams are recombined at the splitter with some lateral shear x. For small angular changes, the shear is a linear function of the angle of the beam splitter. In addition, the optical path difference changes rapidly with the splitter angle. These facts make both the shear plates and the piezoelectric driver used in the corner-cube version unnecessary. The splitter is mounted through flexural pivots to the interferometer frame and oscillates from power supplied by an electrodynamic driver. Fortunately, an oscillation amplitude of only a few degrees is necessary when the aperture diameter D is one the order of one inch. A direct MTF reading is obtained from an oscilloscope display by using the radiant power of the sheared beams and the angular displacement of the splitter as the vertical and horizontal scope inputs respectively. Figure 44 shows two traces for a rectangular aperture, one with no degradation and the other with random degradation. Notice that each trace actually produces four MTF's, one in each quadrant.

In principle, Kelsall's interferometer shown in Figure 43 differs from the MCAIR version only slightly. Shear change is produced by rotating a shear plate in the path between the two mirrors at constant angular rate instead of oscillating the beam splitter. Both shear and optical path difference are linear functions of the shear plate angle, therefore, the time trace of the output power yields the MTF.

These two fast shearing interferometers provide a method for measuring directly boundary flow MTF's. The differences between the two approaches are subtile. Kelsall's instrument provides a constant shear rate in contrast to the variable shear rate inherent in the MCAIR design. The MCAIR approach should be capable of producing a faster MTF because of the lower mechanical motion required. The faster the MTF is produced, the less sensitive it is to vibration and acoustic noise. More information on Kelsall's instrument is available in Reference 25. A detailed description of the MCAIR version will be published in a future MDC report.

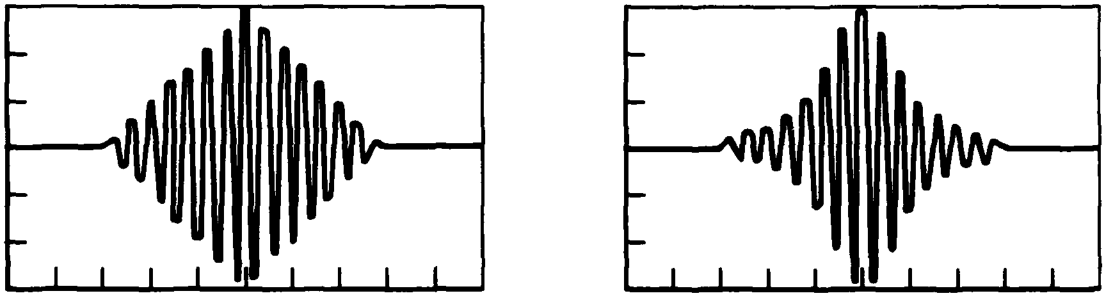

(a) No Degradation (b) Random Degradation

FIGURE 44
SCOPE TRACE OF FAST-SHEARING-INTERFEROMETER OUTPUT POWER
FOR A RECTANGULAR APERTURE

V. Parametric Analysis

The previous sections presented the optical quality of turbulent boundary layers, separated flow, and main flow in terms of either the OTF or phase error Δ. In this section, the OTF s and phase errors will be used to compute the optical effect of boundary flow on propagating and imaging systems. Beam cross-sections and receiving apertures are circles of diameter D. The effect is presented in terms of normalized central power density (NCPD) vs beam diameter for propagating systems and in terms of resolution vs aperture diameter for imaging systems. The following parameter values are considered.

Mach number	0.9
Altitude	8000 ft, 40,000 ft
Wavelengths	0.55μ, 10.6μ

Standard atmospheric conditions at the two altitudes are as follows.[20]

	8000 ft	40,000 ft
Density (kg/m^3)	0.940	0.303
Pressure (nt/m^2)	75,000	18,800
Temperature (°K)	278	217
Speed of sound (m/sec)	334	295

In addition to main flow, turbulent boundary layers, and separated flow, wake flow is also considered. It is treated as a special case of separated flow. Shock waves are not considered because the only quantitative work done here in that area concerns beam direction only, not beam quality.

Often it is desirable to predict the optical effects corresponding to a full scale aircraft by using a scale model. The last subsection derives scaling rules for achieving this objective.

Propagating Systems

The purpose of this subsection is to present the NCPD as a function of beam diameter for main flow, TBL's, separated flow, and wake flow.

In Section II it was shown that the NCPD could be written as a function of either the OTF,

$$\text{NCPD} = \frac{8}{D^2} \int_0^D T\left(\frac{r}{\lambda f}\right) r \, dr, \qquad (5\text{-}1)$$

or the optical phase,

$$\text{NCPD} = \frac{64}{D^4} \left| \int_0^D e^{ik\Delta(r)} r \, dr \right|^2 . \qquad (5\text{-}2)$$

Main Flow. The first step in finding the NCPD for the main flow of a sphere is to find Δ. Equation (3-15) was evaluated for $\theta_0 = 0$, that is, for the beam pointed directly into the flow. The sphere diameter used was one meter and the upper limit of the integral was set at $\ell = 50$, which effectively is the same as $\ell = \infty$. From the symmetry of the geometry, Δ is symmetrical with respect to the origin, $\Delta(x,y) = \Delta(r)$. Figure 45 is a plot of $\Delta(r)$ for altitudes of 8000 ft and 40,000 ft. An approximation to the main flow NCPD can be easily obtained by approximating $\Delta(r)$ with a parabola of the form

$$\Delta_D(r) = w\, r^2. \tag{5-3}$$

Equation (5-3) is plotted as a dotted line in Figure 45 with $\Delta = \Delta_D$ at $r = 0.2$ meters.

Inspection of Equation (3-15) shows that for constant values of $\zeta = x/R$ and $\eta = y/R$, Δ is proportional to $\rho_\infty R$, where ρ_∞ is the freestream density. Equation (5-3) shows that for constant values of r/R, Δ_D is proportional to $w\,R^2$. Therefore if $\Delta(r)$ is approximated by $\Delta_D(r)$, then wR^2 is proportional to $\rho_\infty R$, or w is proportional to ρ_∞/R. If $\Delta(r)$ is set equal to $\Delta_D(r)$ at $r = 0.2$ meters, the equation for w is

$$w = -0.823 \times 10^{-4}\ \rho_\infty/R. \tag{5-4}$$

All units are MKS; w has units of meters^{-1}.

When a wavefront has a phase given by Equation (5-3), it is said to suffer a defect of focus. The resulting NCPD is found by substituting Equation (5-3) into Equation (5-2). The result is

$$\text{NCPD} = \frac{2[1 - \cos(kwD^2/4)]}{(kwD^2/4)^2}. \tag{5-5}$$

Equation (5-5) is plotted in Figure 46. The NCPD for main flow is found by substituting Equation (5-4) into Equation (5-5). Figure 47 plots the NCPD as a function of the beam size D for altitudes of 8000 ft and 40,000 ft and for wavelengths of 0.55μ and 10.6μ. The plots show that the main-flow effect is not serious for 10.6μ at 40,000 ft. For the other conditions, however, the central power may vanish completely, depending on the beam diameter.

Turbulent Boundary Layer. The average OTF for turbulent flow is given by Equations (4-9) and (4-10).

$$\bar{\tau}\left(\frac{r}{\lambda f}\right) = \tau_0\left(\frac{r}{\lambda f}\right) \exp\left\{-k^2\sigma^2\left[1-e^{-(r/a)^2}\right]\right\} \tag{5-6}$$

With the diffraction OTF for a circular aperture, Equation (2-35), Equation (5-6) becomes

$$\bar{\tau}\left(\frac{r}{\lambda f}\right) = \frac{2}{\pi}\left[\cos^{-1}\left(\frac{r}{D}\right)-\left(\frac{r}{D}\right)\sqrt{1-\left(\frac{r}{D}\right)^2}\right] \exp\left\{-k^2\sigma^2\left[1-e^{-(r/a)^2}\right]\right\},\ 0 \le r \le D. \tag{5-7}$$

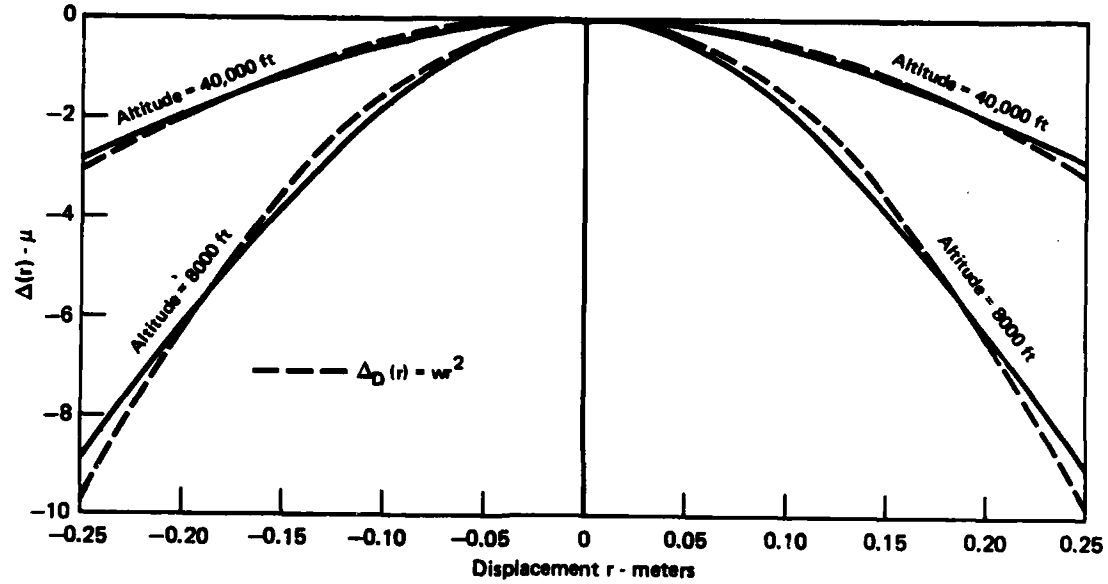

FIGURE 45
PHASE ERROR $\dot{\Delta}(r)$ FOR SPHERE WITH FORWARD-LOOKING BEAM

GP74-0200-46

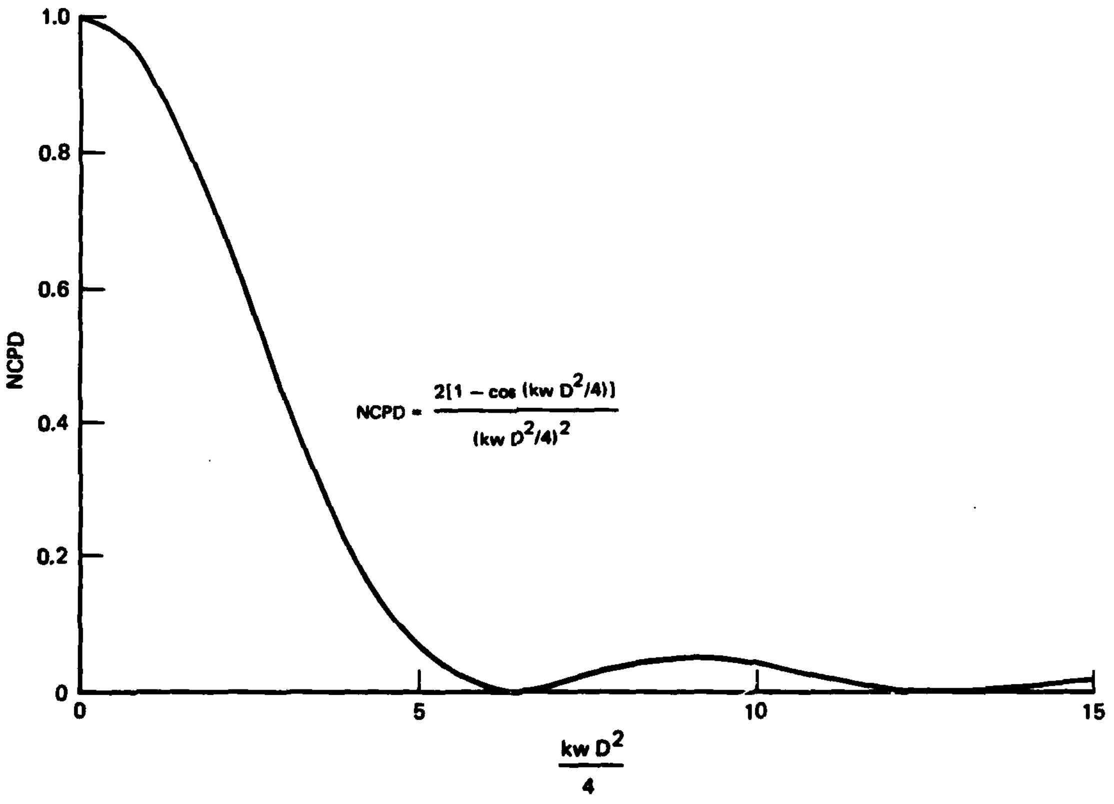

FIGURE 46
NORMALIZED CENTRAL POWER DENSITY (NCPD) FOR A DEFOCUSED SYSTEM

GP74-0200-46

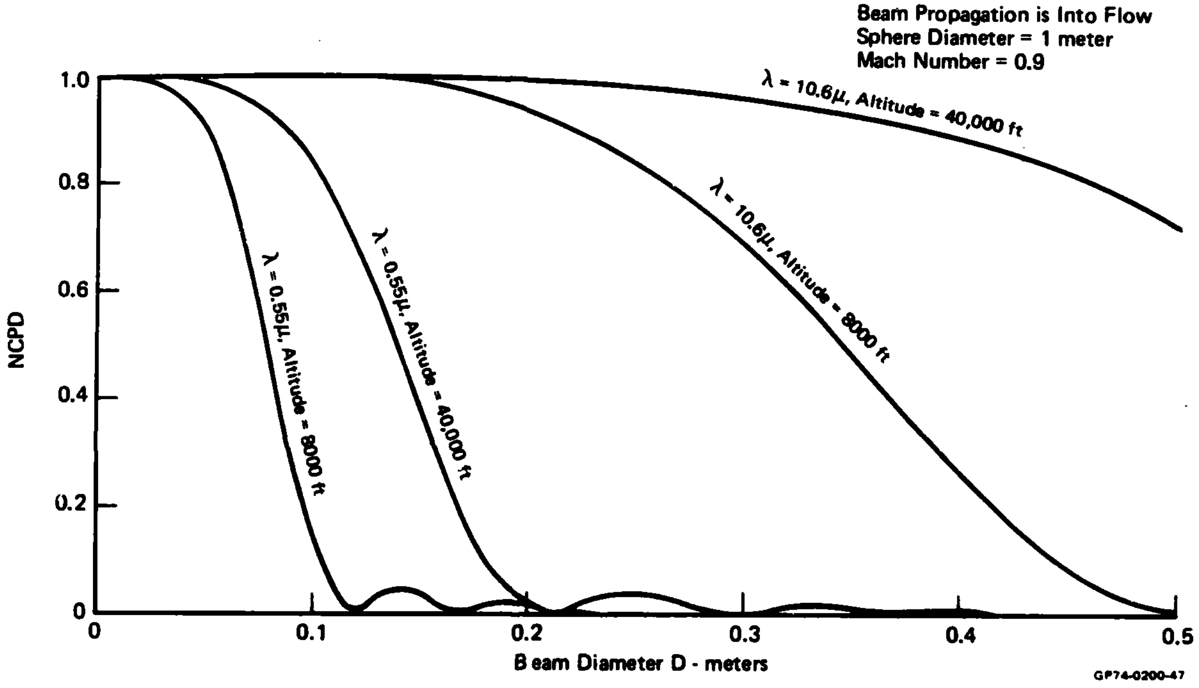

FIGURE 47
MAIN-FLOW NORMALIZED CENTRAL POWER DENSITY (NCPD) vs BEAM DIAMETER FOR MAIN FLOW OF A SPHERE

AD-A122 393 AERODYNAMIC EFFECTS ON AIRBORNE OPTICAL SYSTEMS(U) 2/2
MCDONNELL AIRCRAFT CO ST LOUIS MO D J WOLTERS
14 DEC 73 MDC-A2582

UNCLASSIFIED F/G 20/6 NL

END
DATE
FILMED
1 83
DTIC

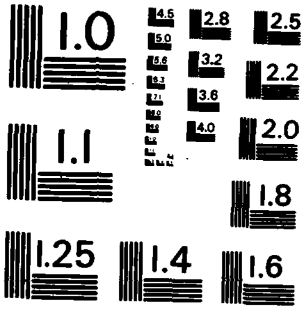

MICROCOPY RESOLUTION TEST CHART
NATIONAL BUREAU OF STANDARDS-1963-A

For the TBL on a flat plate, σ^2 and a are found using Equations (4-53) and (4-54) respectively. Figure 48 plots as a function of D the NCPD found by substituting Equations (5-7), (4-53) and (4-54) into Equation (5-1). The figure shows NCPD plots for altitudes of 8000 ft and 40,000 ft and for wavelengths of 0.55μ and 10.6μ. Distance from the leading edge of the flat plate is two meters. The plots show that the TBL effect is generally weak. In fact it is completely negligible at both altitudes for the 10.6μ wavelength. At the shorter wavelength, the NCPD drops to minimums of 0.85 and 0.98 for altitudes 8000 ft and 40,000 ft respectively. The fact that the NCPD remains constant at its minimum value for all but the smallest aperture sizes is a result of the small spatial scale of the wavefront disturbance.

Separated Flow. The NCPD for separated flow is found by again substituting Equation (5-7) into Equation (5-1). The values of σ^2 and a are found by using Equations (4-76) and (4-77) respectively. Figure 49 plots NCPD as a function of D for altitudes of 8000 ft and 40,000 ft and for wavelengths of 0.55μ and 10.6μ. The separation thickness is 10 cm. The plots show the strong dependence of the separated flow effect on wavelength. At 10.6μ the NCPD drops to only 0.96 and 0.99 for altitude of 8000 ft and 40,000 ft respectively. At 0.55μ, however, the NCPD drops to less than 0.01 for both altitudes. As with the turbulent-boundary-layer NCPD, the small spatial scale of the wavefront disturbance causes the separated-flow NCPD to be constant for all but the smallest values of D.

Wake Flow. In this subsection the NCPD for the wake flow behind a sphere one meter in diameter is considered. The problem is treated as a special case of separated flow. Figure 50 shows the problem geometry. The angle between the polar axis, which points into the flow, and the direction of propagation is θ_0. For purposes of calculating the correlation length, a, the separation thickness is taken to be equal to the sphere radius R. Equation (4-77) becomes

$$a = 0.067R. \qquad (5\text{-}8)$$

The average optical path length through the wake flow is given by

$$L = R\left(\frac{1}{\sin \theta_0} - 1\right). \qquad (5\text{-}9)$$

Since Equation (4-20) implies that σ^2 is proportional to the optical path length, Equation (4-76) becomes

$$\sigma^2 = 1.2 \times 10^{-12}\ \rho_\infty R\left(\frac{1}{\sin \theta_0} - 1\right). \qquad (5\text{-}10)$$

Figure 51 is a plot of the resulting NCPD as a function of beam width for altitudes of 8000 ft and 40,000 ft and for wavelengths of $.55\mu$ and 10.6μ. The sphere radius R is one-half meter, and the polar angle θ_0 is 135°. The NCPD for wake flow is similar to the NCPD for separated flow. The σ^2 value is larger for the wake flow because of the longer optical path. This larger value of σ^2 causes the NCPD to drop to lower values for the 10.6μ wavelength, 0.85 at 8000 ft and 0.95 at 40,000 ft. On the other hand, the value of the correlation length is larger for the wake flow than for the separation flow. The result is that the NCPD reaches its minimum value at larger values of D.

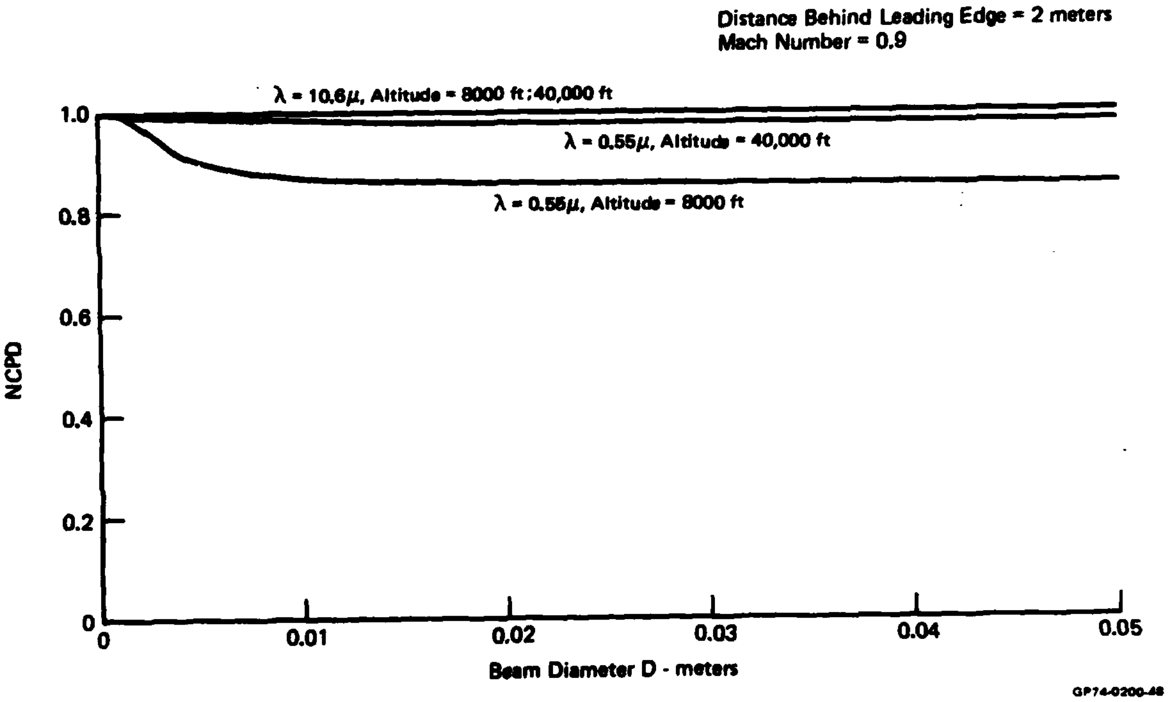

FIGURE 48
NORMALIZED CENTRAL POWER DENSITY (NCPD) vs BEAM DIAMETER FOR THE TURBULENT BOUNDARY LAYER ON A FLAT PLATE

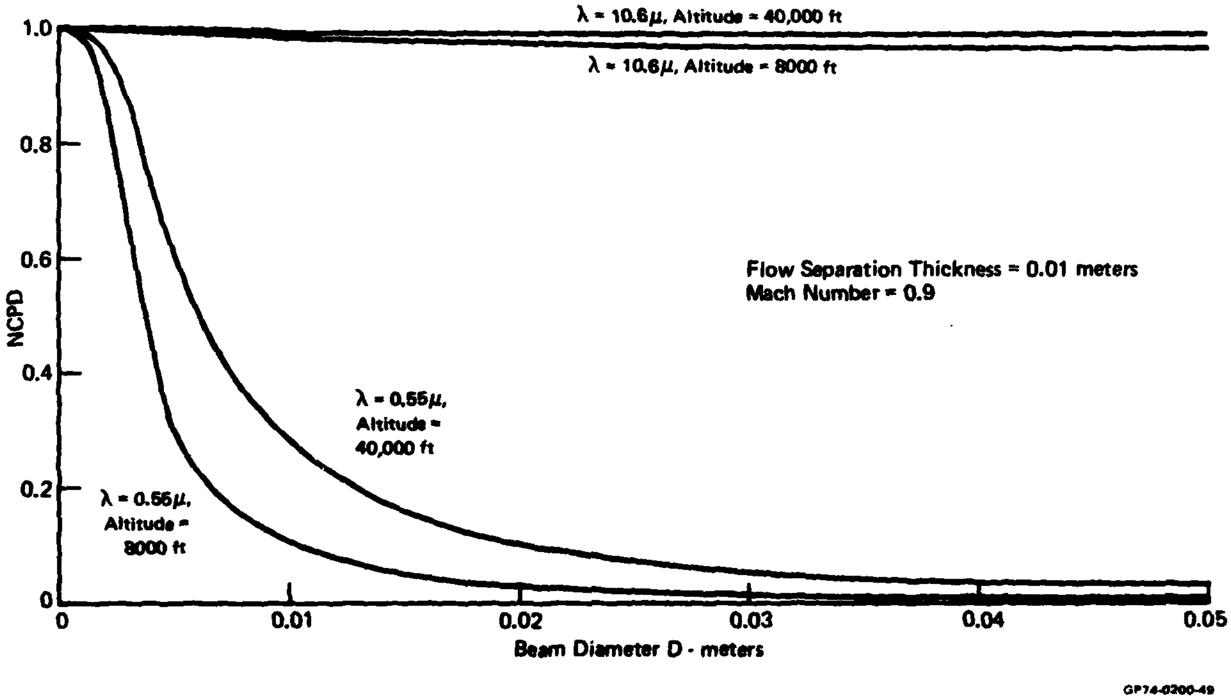

FIGURE 49
NORMALIZED CENTRAL POWER DENSITY (NCPD) vs BEAM DIAMETER
FOR SEPARATED FLOW

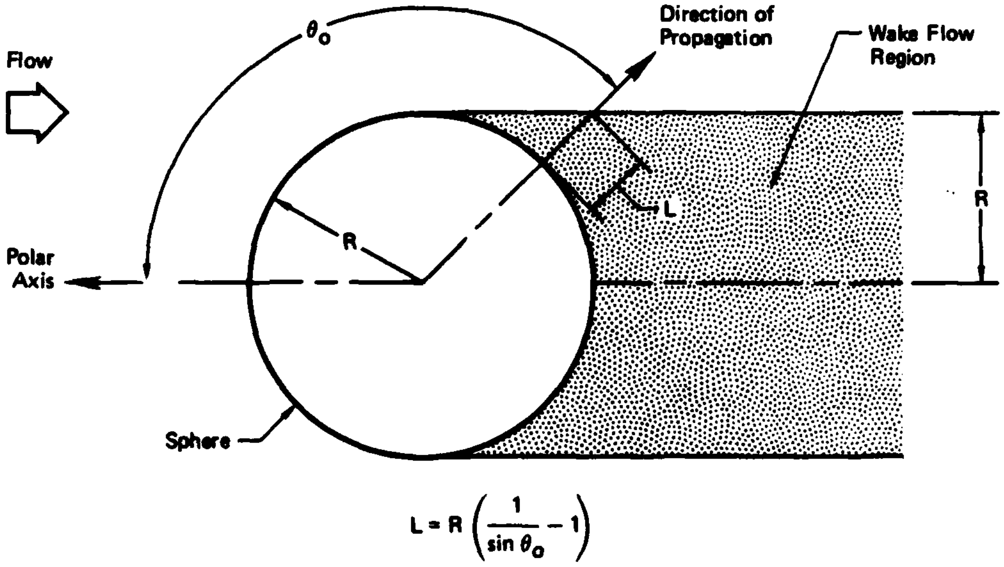

$$L = R\left(\frac{1}{\sin\theta_o} - 1\right)$$

FIGURE 50
WAKE-FLOW PROBLEM GEOMETRY

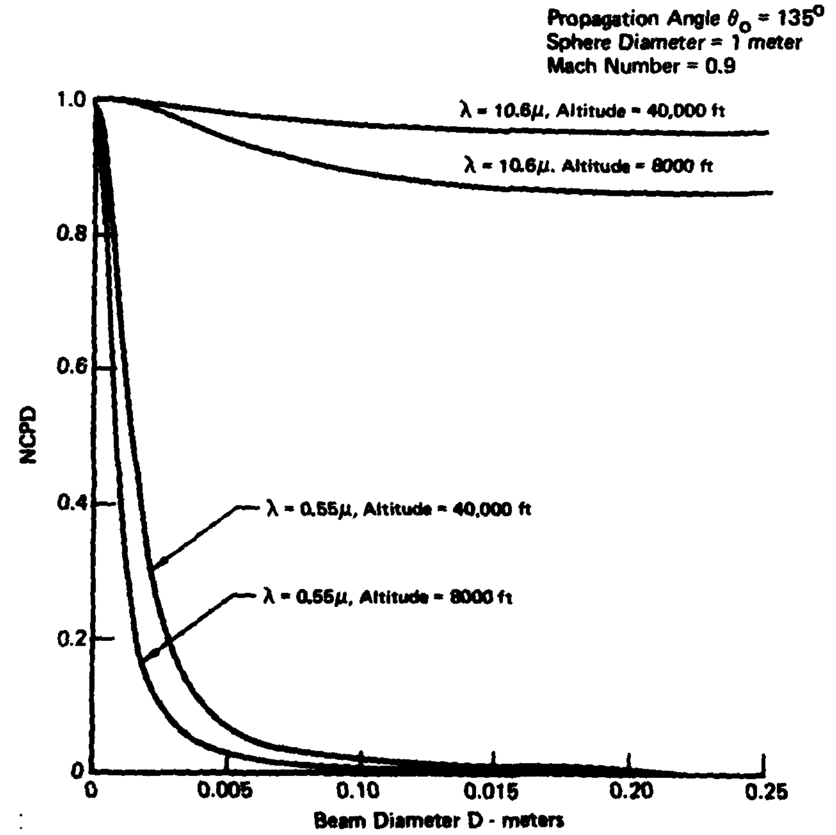

FIGURE 51
NORMALIZED CENTRAL POWER DENSITY (NCPD) vs BEAM DIAMETER FOR THE WAKE FLOW OF A SPHERE

GP74-0200-51

Summary. In general boundary flow has only a slight effect on 10.6μ radiation. The only exception is the effect of main flow at low altitudes in which the NCPD may drop below one percent. At a wavelength of 0.55μ main flow, separated flow, and wake flow can all cause the NCPD to drop below one percent, depending on the beam diameter. Only the TBL effect is not drastic.

Imaging Systems

A common criterion for measuring the performance of an imaging system is system resolution ν_{max}. The units of ν_{max} are inverse distance, for example, mm^{-1} or lines/mm. The value of ν_{max} is found by using Equation (4-57),

$$TM(\nu_{max}) = C_0|\tau(\nu_{max})|, \quad 0 \le C_0 \le 1, \tag{5-11}$$

where $|\tau(\nu_{max})|$ is the MTF of the boundary flow, aperture, and lens, $TM(\nu)$ is the threshold modulation of the film and human recorder, and C_0 is the target modulation.

In an idealized system in which $TM(\nu)$ vanishes and $\tau(\nu)$ is diffraction limited, the resolution ν_{max} is equal to the spatial frequency ν_0 at which the diffraction MTF, $|\tau_0(\nu)|$ vanishes.

$$|\tau_0(\nu_{max})| = |\tau_0(\nu_0)| = 0 \tag{5-12}$$

From Equation (2-35) ν_0 is given by

$$r = \lambda f \nu_0 = D \tag{5-13}$$

or

$$\nu_{max} = \nu_0 = \frac{D}{\lambda f} \tag{5-14}$$

where D is aperture diameter, λ is wavelength, and f is focal length.

To find ν_{max} for a real system, C_0, $\tau(\nu)$, and $TM(\nu)$ must all be specified. However, there is a method of approximating the effect of boundary flow on image resolution by using only the MTF for the aperture and the boundary flow. This method allows us to examine the effect of boundary flow on imaging systems without specifying a particular system. Let $\tau_L(\nu)$ and ν_L be OTF and resolution respectively for the system excluding boundary flow. Let $\tau(\nu)$ and ν_{max} be the OTF and resolution respectively for the system including boundary flow. Figure 52 shows plots of $C_0|\tau_L(\nu)|$ and $C_0|\tau(\nu)|$. We assume that ν_L is small enough so that the TM is fairly constant for $\nu<\nu_L$. This assumption is usually accurate for aerial reconnaissance situations because C_0 is small, say 0.1 to 0.3. Two new linear OTF's, $\tau_L''(\nu)$ and $\tau''(\nu)$, are constructed such that the NCPD's corresponding to τ_L and τ_L'' are equal and the NCPD's corresponding to τ and τ'' are equal. The resolutions corresponding to τ_L'' and τ'' are ν_L'' and ν_{max}'' respectively. The equations for τ_L'' and τ'' are respectively

$$\tau_L''(\nu) = 1 - \nu/h_L = 1 - \frac{r}{\lambda f h_L}, \quad 0 \le \nu = \frac{r}{\lambda f} \le h_L \tag{5-15}$$

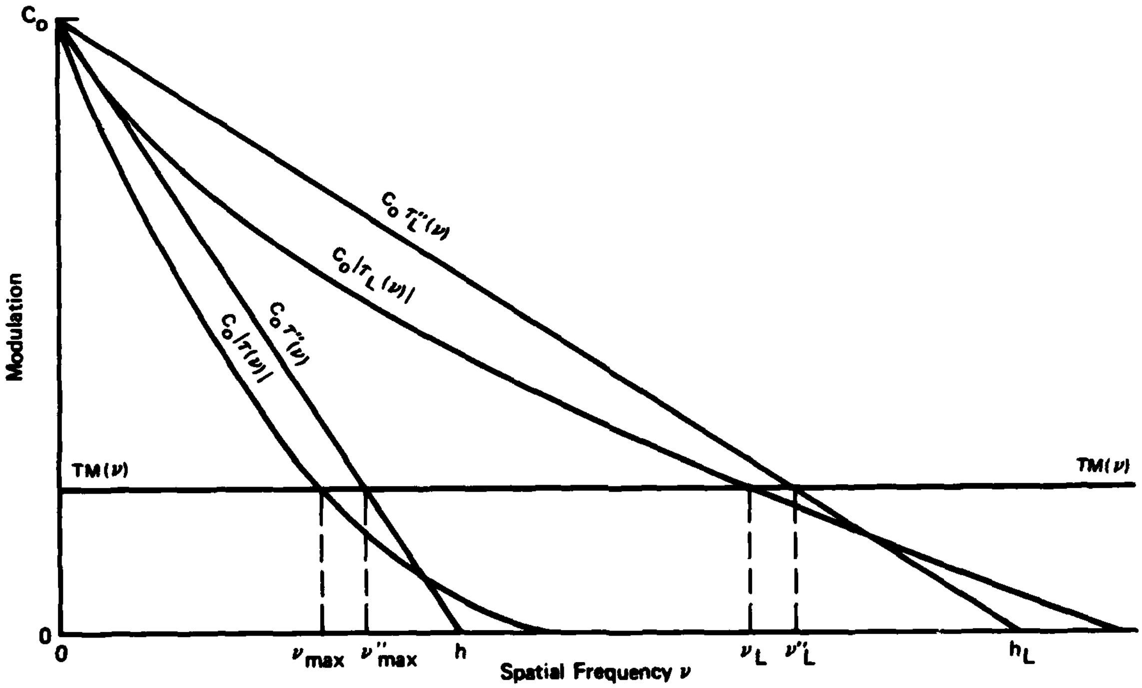

FIGURE 52
APPROXIMATION OF SYSTEM RESOLUTION USING A LINEAR OTF

GP74-0200-52

and

$$\tau''(\nu) = 1 - \nu/h = 1 - \frac{r}{\lambda fh}, \quad 0 \le \nu = \frac{r}{\lambda f} \le h \tag{5-16}$$

where h_L and h are defined by

$$\tau''_L(h_L) = \tau''(h) = 0. \tag{5-17}$$

The values of the NCPD's are found in terms of h_L and h by substituting Equations (5-15) and (5-16) respectively into Equation (5-1).

$$NCPD_L = \frac{8}{D^2} \int_0^{\lambda fh_L} (1 - \frac{r}{\lambda fh_L})\ r\ dr = \frac{4}{3} (\frac{\lambda fh_L}{D})^2 \tag{5-18}$$

$$NCPD = \frac{8}{D^2} \int_0^{\lambda fh} (1 - \frac{r}{\lambda fh})\ r\ dr = \frac{4}{3} (\frac{\lambda fh}{D})^2 \tag{5-19}$$

$NCPD_L$ is the NCPD corresponding to τ_L and τ''_L.

The ratio ν_{max}/ν_L is approximated by ν''_{max}/ν''_L. From the geometry in Figure 52 we have

$$\frac{\nu''_{max}}{\nu''_L} = \frac{h}{h_L}. \tag{5-20}$$

Solving Equations (5-18) and (5-19) for h_L and h respectively and substituting into Equation (5-20) we arrive at the approximation formula,

$$\frac{\nu_{max}}{\nu_L} \approx \frac{\nu''_{max}}{\nu''_L} = \frac{NCPD}{NCPD_L}. \tag{5-21}$$

Let us now work a sample problem with the following input parameters.

Wavelength	.55	Altitude	8000 ft
Focal Length	152.2 mm	Mach No.	0.9
Aperture size	9.5 mm (f/16)	Film	Kodak 3414
Target contrast	2:1	Lens Degradation	None
Type of degradation	10 cm flow separation		

First the resolution ν_{max} is found using Equation (5-11). The TM(ν) for Kodak 3414 film is given by Equation (4-65). From the target contrast of 2:1 and from Equation (2-50), C_0 must satisfy

$$\frac{1 + C_0}{1 - C_0} = \frac{2}{1} \tag{5-22}$$

or

$$C_0 = \frac{1}{3}. \tag{5-23}$$

The MTF is given by Equations (5-7), (4-76) and (4-77). For an altitude of 8000 ft, ρ_∞ is 0.940 nt/m^2. The value of L is 0.01 m. Figure 53 plots both TM(ν) and $C_0\tau(\nu)$ as a function of ν. The resolution is found to be ν_{max} = 30 lines/mm. The function $C_0\tau_0(\nu)$ is also plotted in Figure 53. The corresponding diffraction limit resolution is ν_D = 84 lines/mm. To use the approximation formula, Equation (5-21) we set $\nu_L = \nu_D$ = 84 lines/mm and $NCPD_L$ = 1 since there is no lens degradation. From Figure 49 the value of NCPD is 0.115. Using the approximation

$$\nu_{max} \approx \nu_L \sqrt{\frac{NCPD}{NCPD_L}} = \nu_D \sqrt{NCPD_L} \qquad (5\text{-}24)$$

the system resolution ν_{max} becomes 28 lines/mm. We see that for this case our approximation for ν_{max} is good.

Often it is convenient to express the performance of an imaging system in terms of angular resolution AR or ground resolution GR. Figure 54 shows geometrically how AR and GR are related to ν_{max}. The relationship may be expressed as follows.

$$AR = \frac{1}{f\nu_{max}} \qquad (5\text{-}25)$$

$$GR = SR \cdot AR = \frac{SR}{f\nu_{max}} \qquad (5\text{-}26)$$

The term SR is the slant range from the ground target to the imaging system. In the idealized imaging system corresponding to Equation (5-14), AR and GR become respectively

$$AR = \frac{\lambda}{D} \qquad (5\text{-}27)$$

and

$$GR = SR\,\frac{\lambda}{D}. \qquad (5\text{-}28)$$

Figures 55 and 56 show ν_{max} and the corresponding values of AR and GR as functions of D for the different types of boundary flow. In Figure 55, altitude is 8000 ft, in Figure 56, 40,000 ft. Also shown are the diffraction-limit resolutions ν_D. The system resolution ν_{max} is calculated using the approximation formula, Equation (5-24). Values of wavelength, focal length, target contrast, mach number, and lens degradation are the same as those in the sample problem. Conditions for each type of flow are the same as those used in the Propagation Systems subsection. In calculating GR, vertical imaging was assumed, so that slant range equals the altitude.

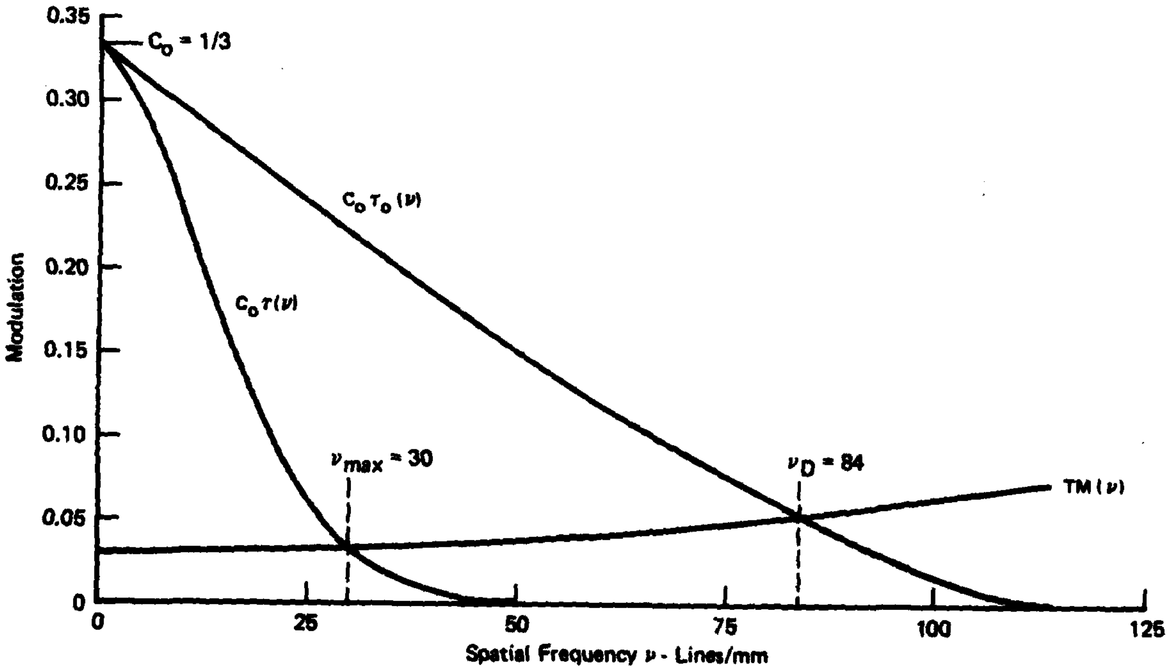

GP74-0200-53

FIGURE 53
MTF AND TM CURVES FOR SAMPLE PROBLEM

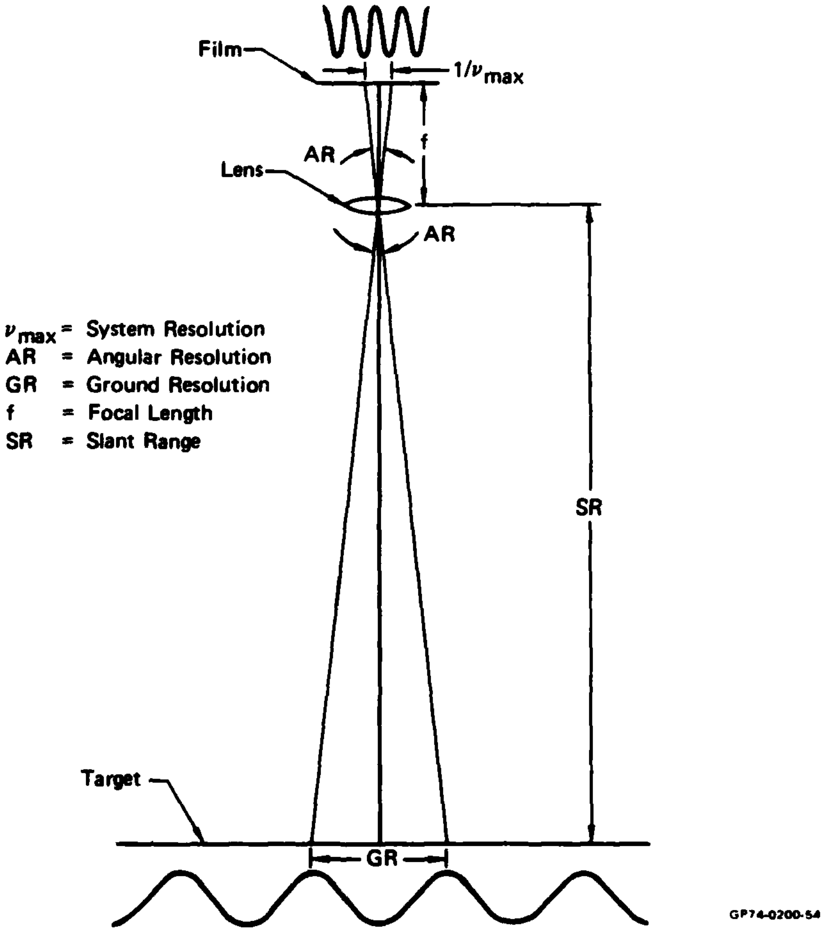

FIGURE 54
RELATIONSHIP BETWEEN RESOLUTION ν_{MAX}, ANGULAR RESOLUTION AR, AND GROUND RESOLUTION GR

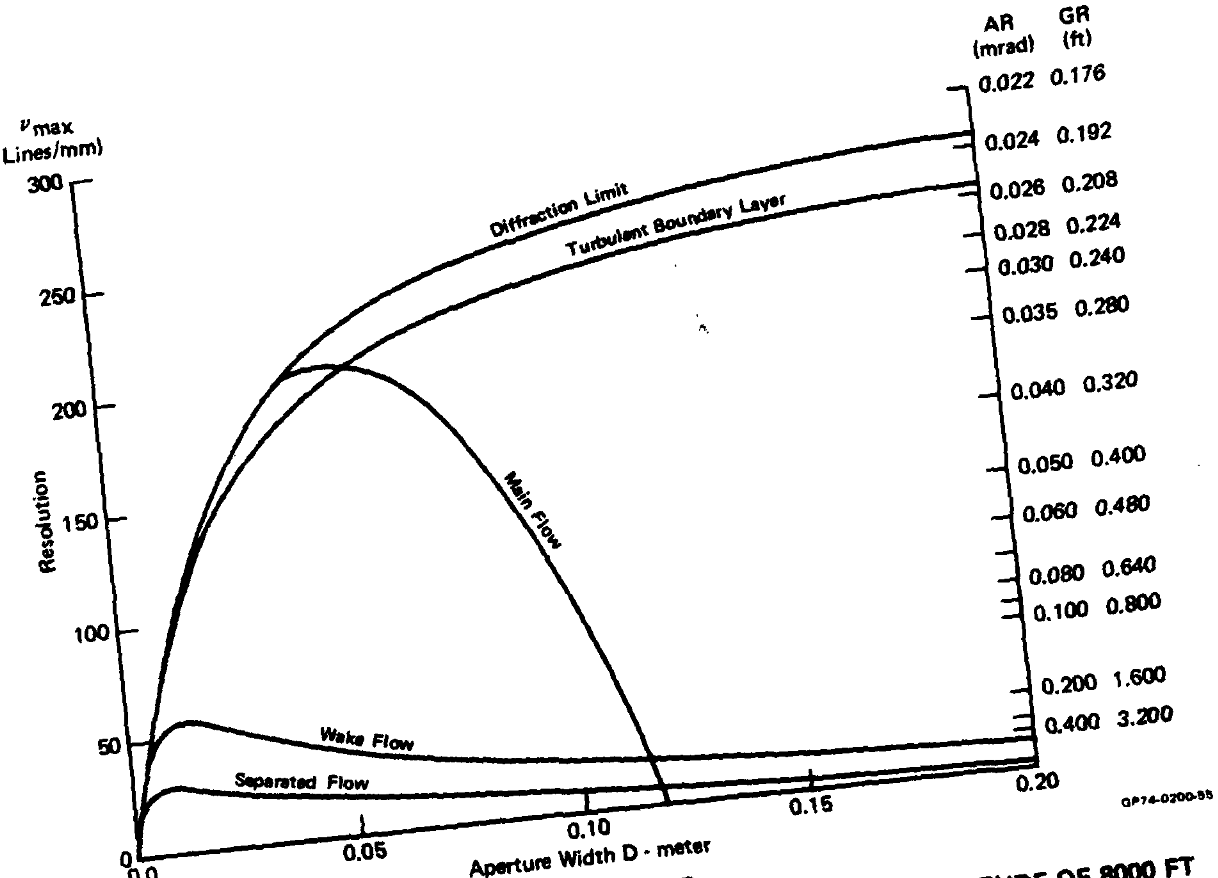

FIGURE 55
RESOLUTIONS ν_{MAX}, AR, AND GR vs APERTURE DIAMETER FOR AN ALTITUDE OF 8000 FT

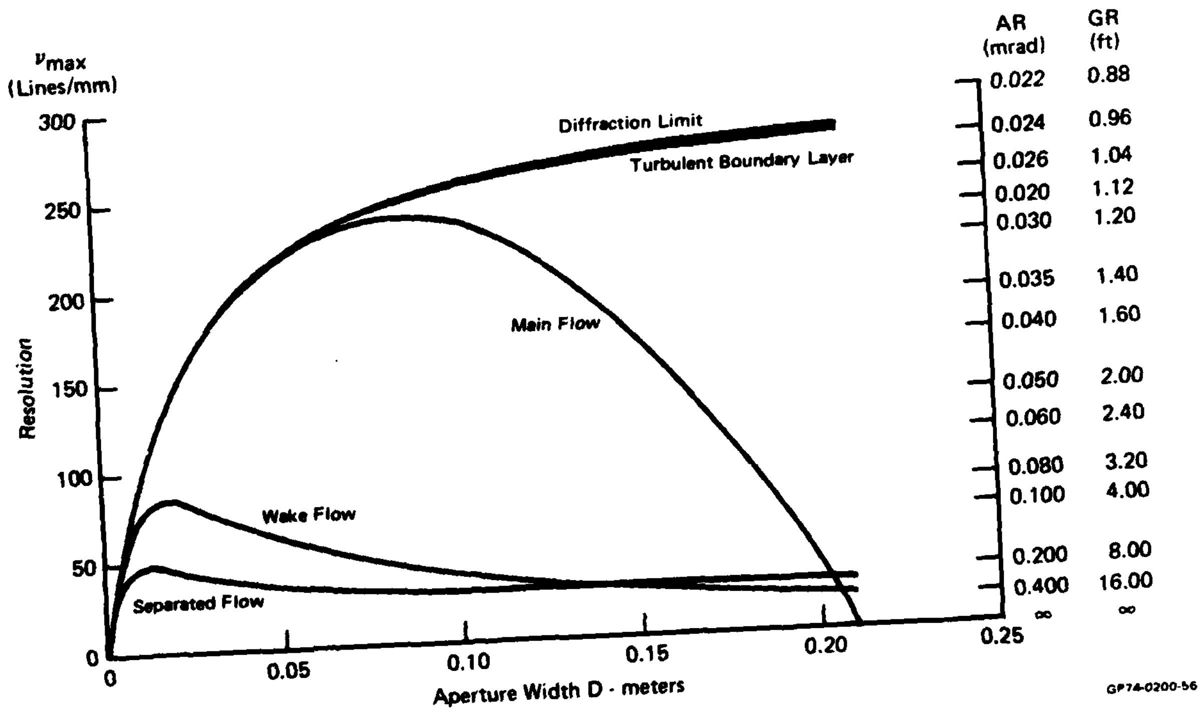

FIGURE 56
RESOLUTIONS ν_{MAX}, AR, AND GR vs APERTURE DIAMETER FOR AN ALTITUDE OF 40,000 FT

Scaling

This subsection derives the scaling rules for predicting the boundary-flow optical effects of a body from a similar body of different scale. The derivation uses the aerodynamic scaling rules from Section II.

We specify here that when the body is scaled, the aperture area or beam cross-section area Σ is scaled by the same factor. For the moment we assume that all linear dimensions of the boundary flow are also scaled by the same factor. Let the aerodynamic system containing the original body be defined as System 1, and let the system containing the scaled body be System 2. Let S be the scale of Body 2 relative to Body 1. If the two bodies are the same size, S is one. Given the temperature T_1, Mach number M_1, density ρ_1, and wavelength λ_1 of System 1 and the scale S, we wish to find the appropriate temperature T_2, Mach number M_2, density ρ_2, and wavelength λ_2 for System 2 such that the two systems produce similar optical effects. Similar optical effects are produced if the pupil functions are similar.

$$G_1(x,y) = G_2(Sx,Sy) \tag{5-29}$$

Since the amplitude part of the pupil function is constant, Equation (5-29) is satisfied if the phases are similar,

$$k_1\Delta_1(x,y) = k_2\Delta_2(Sx,Sy) \tag{5-30}$$

or

$$\Delta_1(x,y)/\lambda_1 = \Delta_2(Sx,Sy)/\lambda_2. \tag{5-31}$$

Given T_1, M_1, ρ_1, λ_1, and S the problem is to find T_2, M_2, ρ_2, and λ_2 such that Equation (5-31) is satisfied. The equation relating the two areas, Σ_1 and Σ_2,

$$\Sigma_2 = S^2\Sigma_1 \tag{5-32}$$

and Equation (2-28) show that if Equation (5-31) is satisfied, then the OTF's of the two systems are similar.

$$\tau_1\left(\frac{x}{\lambda_1 f_1}, \frac{y}{\lambda_1 f_1}\right) = \tau_2\left(\frac{Sx}{\lambda_2 f_2}, \frac{Sy}{\lambda_2 f_2}\right) \tag{5-33}$$

Likewise Equation (2-51) show that if Equation (5-31) is satisfied, then the NCPD's of the two systems are equal.

$$NCPD_1 = NCPD_2 \tag{5-34}$$

General Case. Rules are now derived for finding appropriate values of T_2, M_2, ρ_2, and λ_2. These rules may be applied to all types of boundary flow.

The relationship between Δ and density ρ is given by Equation (3-3).

$$\Delta(x,y) = K \int_0^L [\rho(x,y,z) - \rho(0,0,z)]\, dz \tag{5-35}$$

Substituting Equation (5-35) into Equation (5-31) yields

$$\frac{K}{\lambda_1} \int_0^{L1} [\rho_1(x,y,z) - \rho(0,0,z)]\, dz = \frac{K}{\lambda_2} \int_0^{SL_1} [\rho_2(Sx,Sy,z) - \rho_2(0,0,z)]\, dz \tag{5-36}$$

or

$$\frac{\rho_{\infty 1}}{\lambda_1} \int_0^{L_1} \frac{\rho_1(x,y,z) - \rho(0,0,z)}{\rho_{\infty 1}}\, dz = \frac{S\rho_{\infty 2}}{\lambda_2} \int_0^{L_1} \frac{\rho_2(Sx,Sy,Sz) - \rho_2(0,0,Sz)}{\rho_{\infty 2}}\, dz \tag{5-37}$$

where $\rho_{\infty 1}$ and $\rho_{\infty 2}$ are the freestream densities.

Examination of Equation (5-37) shows that if the equations

$$\frac{\rho_{\infty 1}}{\lambda_1} = \frac{S\rho_{\infty 2}}{\lambda_2} \tag{5-38}$$

and

$$\frac{\rho_1(x,y,z)}{\rho_{\infty 1}} = \frac{\rho_2(Sx,Sy,Sz)}{\rho_{\infty 2}} \tag{5-39}$$

are satisfied, then Equation (5-31) is satisfied. Equations (5-38) and (5-39) are, therefore, the general optical scaling rules. Generally $\rho_{\infty 2}$ and λ_2 can be adjusted so that Equation (5-38) holds. Equation (5-39) will hold if the aerodynamic flows for the two systems are similar. Section II shows that similarity of the flows is guaranteed if the Mach numbers and Reynolds numbers are equal.

$$M_1 = M_2 \tag{5-40}$$

$$\frac{\rho_1 V_1}{\mu_1} = S\, \frac{\rho_2 V_2}{\mu_2} \tag{5-41}$$

For equal temperatures

$$T_1 = T_2 \tag{5-42}$$

and Mach numbers, Equation (5-41) becomes

$$\rho_1 = S\rho_2. \tag{5-43}$$

Substituting Equation (5-43) with freestream values of ρ_1 and ρ_2 into Equation (5-38) yields

$$\lambda_1 = \lambda_2. \tag{5-44}$$

In terms of freestream values the general optical scaling laws may be summarized as follows

$$T_{\infty 1} = T_{\infty 2},\ M_{\infty 1} = M_{\infty 2},\ \rho_{\infty 1} = S\rho_{\infty 2},\ \lambda_1 = \lambda_2 \tag{5-45}$$

If Equations (5-45) are satisfied, the two systems produce similar flows and similar optical effects and Equations (5-31), (5-33), and (5-34) all hold.

In scale model testing it is often difficult or impossible to meet the requirement for density. Approximately similar optical effects can be produced, however, even if the requirements in Equation (5-45) are relaxed as shown below.

Main Flow. We have shown that if Equations (5-38) and (5-39) are satisfied the two systems produce similar optical effects. Using Equation (3-4), which is based on the Karman-Tsien approximation for subsonic main flow, we can now show that Equation (5-39) is automatically satisfied for subsonic main flow if freestream temperatures and Mach numbers for the two systems are equal.

Substituting Equations (3-5), (3-6), and (3-9) into Equation (3-4) yields

$$\frac{\rho(x,y,z)}{\rho_\infty} = \left(1 + \frac{\gamma-1}{2} M_\infty^2\right)^{\frac{1}{\gamma-1}} \frac{2(\gamma-1)M_\infty^2 + 4 - V^2(x,y,z)/a_\infty^2}{2(\gamma-1)M_\infty^2 + 4 + V^2(x,y,z)/a_\infty^2}. \tag{5-46}$$

where V is the potential-flow velocity field. It is a property of potential flow that similar bodies of different scales produce similar velocity fields

$$\frac{V_1(x,y,z)}{U_1} = \frac{V_2(Sx,Sy,Sz)}{U_2}. \tag{5-47}$$

The U's are freestream speeds. If the freestream Mach numbers and temperatures are equal, then the freestream speeds are equal.

$$U_1 = U_2 \tag{5-48}$$

Equations (5-46), (5-47), and (5-48) show that Equation (5-39) is satisfied. The optical scaling rules for subsonic main flow may be summarized as follows

$$T_{\infty 1} = T_{\infty 2},\ M_{\infty 1} = M_{\infty 2},\ \frac{\rho_{\infty 1}}{\lambda_1} = S\,\frac{\rho_{\infty 2}}{\lambda_2} \tag{5-49}$$

Turbulent Boundary Layers. Although we have no equations for Δ or ρ in a random flow, we do have equations for the average OTF. For this reason Equation (5-33) is used as the similarity condition to be met rather than Equation (5-31).

Assuming that freestream temperatures and Mach numbers are equal for the two systems, Equations (2-34), (4-9), (4-16), (4-53), and (4-54) yield

$$\overline{\tau}_1\left(\frac{x}{\lambda_1 f_1}, \frac{y}{\lambda_1 f_2}\right) = \tau_{01}\left(\frac{x}{\lambda_1 f_1}, \frac{y}{\lambda_1 f_1}\right)\ \exp\left\{ -c_3 \frac{(\rho_{\infty 1} X_1)^{12/7}}{\lambda_1^2} \times \left[1 - \exp\left(- \frac{x^2 + y^2}{c_4 \rho_{\infty 1}^{-2/7} X_1^{12/7}}\right)\right]\right\} \tag{5-50}$$

and

$$\overline{\tau}_2\left(\frac{Sx}{\lambda_2 f_2}, \frac{Sy}{\lambda_2 f_2}\right) = \tau_{02}\left(\frac{Sx}{\lambda_2 f_2}, \frac{Sy}{\lambda_2 f_2}\right)\ \exp\left\{ -c_3 \frac{(\rho_{\infty 2} S X_1)^{12/7}}{\lambda_2^2} \times \left[1 - \exp\left(- \frac{S^2 x^2 + S^2 y^2}{c_4 \rho_{\infty 2}^{-2/7} S^{12/7} X_1^{12/7}}\right)\right]\right\} \tag{5-51}$$

where c_3 and c_4 are constants and where τ_{01} and τ_{02} are the diffraction-limit OTF's corresponding to Systems 1 and 2 respectively. Note that the T_0's are always equal. For $\overline{\tau}_1$ and $\overline{\tau}_2$ to be equal, the following equations must be satisfied.

$$\frac{\rho_{\infty 1}^{12/7}}{\lambda_1^2} = \frac{(S\rho_{\infty 2})^{12/7}}{\lambda_2^2} \tag{5-52}$$

$$\rho_{\infty 1}^{2/7} = \rho_{\infty 2}^{2/7}\, S^{2/7} \tag{5-53}$$

These equations imply

$$\rho_{\infty 1} = S\rho_{\infty 2} \tag{5-54}$$

and

$$\lambda_1 = \lambda_2. \tag{5-55}$$

These are the optical scaling rules for the general case. However, it is possible to relax Equations (5-54) and (5-55) and still obtain approximately similar optical effects if the wavelength is properly adjusted. Equation (5-51) shows that the exponential term varies according to the two-sevenths power of $\rho_{\infty 2}S$ and according to the second power of x. Equation (5-53) can, therefore, be ignored without too much error provided that $S\rho_{\infty 2}$ is within a factor of two or three of $\rho_{\infty 1}$. Then only Equation (5-52) must be satisfied. This equation, however, is approximately the same as Equation (5-38). The following scaling rules may, therefore, be used to obtain approximately similar optical effects for a TBL.

$$T_{\infty 1} = T_{\infty 2},\ M_{\infty 1} = M_{\infty 2},\ \frac{\rho_{\infty 1}}{\lambda_1} = S\,\frac{\rho_{\infty 2}}{\lambda_2} \tag{5-56}$$

These are the same equations that were derived for subsonic main flow.

<u>Separated</u> <u>Flow</u>. The rules for separated flow are found in the same way as the rules for the TBL.

Assuming that Mach numbers for both systems are in the 0.8 - 0.95 range, Equations (2-34), (4-9), (4-16), (4-76), and (4-77) yield

$$\bar{\tau}_1\left(\frac{x}{\lambda_1 f_1},\frac{y}{\lambda_2 f_2}\right) = \tau_{01}\left(\frac{x}{\lambda_1 f_1},\frac{y}{\lambda_1 f_1}\right)\exp\left\{-c_5\frac{\rho_{\infty 1}L_1}{\lambda_1{}^2}\left[1 - \exp\left(-\frac{x^2 + y^2}{c_6 L_1{}^2}\right)\right]\right\} \tag{5-57}$$

and

$$\bar{\tau}_2\left(\frac{Sx}{\lambda_2 f_2},\frac{Sy}{\lambda_2 f_2}\right) = \tau_{02}\left(\frac{Sx}{\lambda_2 f_2},\frac{Sy}{\lambda_2 f_2}\right)\exp\left\{-\ c_5\ \frac{\rho_{\infty 2}SL_1}{\lambda_2{}^2}\left[1 - \exp\left(-\ \frac{S^2x^2 + S^2y^2}{c_6 S^2 L_1{}^2}\right)\right]\right\} \tag{5-58}$$

where c_5 and c_6 are constants. For these two average OTF's to be equal the following equation must be satisfied.

$$\frac{\rho_{\infty 1}}{\lambda_1^2} = S\,\frac{\rho_{\infty 2}}{\lambda_2^2} \qquad (5\text{-}59)$$

The scaling rules for separated flow may be summarized as follows.

$$0.8 \le M_{\infty 1},\ M_{\infty 2} \le 0.95,\quad \frac{\rho_{\infty 1}}{\lambda_1^2} = S\,\frac{\rho_{\infty 1}}{\lambda_2^2} \qquad (5\text{-}60)$$

Since wake flow is a special case of separated flow, these rules also apply to wake flow.

Summary and Comments. Figure 57 summarizes the optical similarity rules for the general, main-flow, TBL, and separated-flow cases. It must be remembered that the rules for main flow, TBL, and separated flow were derived from models which are only approximately correct. Even so, all of the scaling rules are consistant, since satisfaction of the general rules implies satisfaction of the other scaling rules.

The rules for most of the cases include the equality of the freestream temperatures. It should be noted that even if these temperatures vary from each other by several degrees, they may differ by only a few percent on an absolute scale.

Rules for General Case	Approximations for Various Flow Types		
	Subsonic Main Flow	Turbulent Boundary Layer	Separated and Wake Flow
$T_{\infty 1} = T_{\infty 2}$ $M_{\infty 1} = M_{\infty 2}$ $\rho_{\infty 1} = S\rho_{\infty 2}$ $\lambda_1 = \lambda_2$	$T_{\infty 1} = T_{\infty 2}$ $M_{\infty 1} = M_{\infty 2}$ $\frac{\rho_{\infty 1}}{\lambda_1} = S\frac{\rho_{\infty 2}}{\lambda_2}$	$T_{\infty 1} = T_{\infty 2}$ $M_{\infty 1} = M_{\infty 2}$ $\frac{\rho_{\infty 1}}{\lambda_1} = S\frac{\rho_{\infty 2}}{\lambda_2}$	$0.8 \le M_{\infty 1}, M_{\infty 2} \le 0.95$ $\frac{\rho_{\infty 1}}{\lambda_1^2} = S\frac{\rho_{\infty 2}}{\lambda_2^2}$

GP74-0200-57

FIGURE 57
OPTICAL SCALING RULES

Appendix A

Notations, Symbols, and Important Equations

This appendix is divided into five parts:

- Acronyms
- Abbreviations for Units
- Notation for Operations
- Symbols
- Important Equations

Acronyms

MTF	Modulation Transfer Function
NCPD	Normalized Central Power Density
OTF	Optical Transfer Function
TM	Threshold Modulation
TBL	Turbulent Boundary Layer

Abbreviations for Units

°K	Degrees Kelvin
kg	Kilogram
m	Meter
mm	Millimeter
nt	Newton
μ	Micron

Notation for Operations

E	Expected value
ϵ	Is an element of
$\not\epsilon$	Is not an element of
*	(superscript) Complex conjugate
—	(overbar) Time average

Symbols

A	Optical-wave amplitude
AR	Angular resolution
B	Constant (Equations (4-67) and (4-68))
C	Radiant power emerging from an aperture
C_0	Target modulation
C_1	Image modulation
C_p	Fluctuating pressure coefficient
D	Diameter of circular aperture
D_x	Dimension of rectangular aperture
D_y	Dimension of rectangular aperture
F	Optical-wave function
G	Pupil function
G_0	Diffraction - limit pupil function
G_1	Pupil function for System 1
G_2	Pupil function for System 2
GR	Ground resolution
H	Working variable (Equations (3-7) and (3-8))
I	Image irradiance or power density in the focal plane
I_0	Diffraction limit of I
J_0	Zero-order Bessel function of the first kind
J_1	First-order Bessel function of the first kind
J_i	ith-order Bessel function of the first kind
K	Gladstone - Dale constant
L	Physical length of optical path
L_1	Physical length of optical path for System 1
M	Mach number
M_1	Mach number for System 1
M_2	Mach number for System 2
M_∞	Free-stream Mach number
$M_{\infty 1}$	Free-stream Mach number for System 1
$M_{\infty 2}$	Free-stream Mach number for System 2
N	Refractive modulus
NCPD	Normalized central power density
$NCPD_L$	Normalized central power density with no boundary-flow effect

$NCPD_1$	Normalized central power density for System 1
$NCPD_2$	Normalized central power density for System 2
O	Object radiance
P	Pressure
P_{wv}	Water-vapor pressure
P_∞	Freestream pressure
Q	Normalized output power for Stine-Winovich experiment
R	Radial coordinate $(\sqrt{X^2 + Y^2})$
R	Radius of sphere
R_x	Reynolds number
S	Scale
S_i	Fourier transform of image radiance
S_o	Fourier transform of object irradiance
SR	Slant range
T	Temperature
T_1	Temperature for System 1
T_2	Temperature for System 2
T_∞	Freestream temperature
$T_{\infty 1}$	Freestream temperature for System 1
$T_{\infty 2}$	Freestream temperature for System 2
TM	Threshold Modulation
U	Complex amplitude of optical wave in the focal plane
U	Freestream airspeed
U_1	Freestream airspeed for System 1
U_2	Freestream airspeed for System 2
V	Speed of fluid (air)
V_1	Air speed for System 1
V_2	Air speed for System 2
W	Optical wavefront
X	Characteristic linear dimension
X	Distance from leading edge of a flat plate
X	Cartesian coordinate in the focal plane
X'	Cartesian coordinate in the object plane
Y	Cartesian coordinate in the focal plane
Y'	Cartesian coordinate in the object plane

a	Speed of sound in a fluid (air)
a	Correlation length of wave phase Δ
a_0	Stagnation or reservoir speed of sound
a_c	Critical speed of sound
a_x	Correlation length of wave phase Δ in the x-direction
a_y	Correlation length of wave phase Δ in the y-direction
a_∞	Freestream speed of sound
b_0	Constant in threshold modulation model
b_1	Constant in threshold modulation model
c	Speed of light
c_1	Working variable (Equations (3-15) and (3-16))
c_2	Working variable (Equations (3-15) and (3-17))
c_3	Constant (Equations (5-50) and (5-51))
c_4	Constant (Equations (5-50) and (5-51))
c_5	Constant (Equations (5-57) and (5-58))
c_6	Constant (Equations (5-57) and (5-58))
c_p	Specific heat at constant pressure
c_v	Specific heat at constant volume
f	Focal length
f_1	Focal length for System 1
f_2	Focal length for System 2
g	Acceleration of gravity
h	Spatial frequency at which τ'' vanishes
h_L	Spatial frequency at which τ_L'' vanishes
k	Wave number ($2\pi/\lambda$)
k_1	Wave number for System 1
k_2	Wave number for System 2
ℓ	Physical length of optical path normalized by sphere radius
m	Integer
n	Refractive index
n_1	Refractive index ahead of shock wave
n_2	Refractive index behind shock wave
p	Point spread function
pow	Radiant output power of a shearing interferometer
q	Working variable (Equations (3-15) and (3-18))

r	Radial coordinate $(\sqrt{x^2 + y^2})$
r_a	Radius of source aperture in Stine-Winovich experiment
r_b	Radius of collection aperture in Stine-Winovich experiment
s	Distance along optical path
t	Time
u	Fluid velocity component in the x-direction
u	Dummy variable in Equation (4-49)
u_1	Horizontal velocity component ahead of shock wave
u_2	Horizontal velocity component behind shock wave
u_1'	Normalized value of u_1 (u_1/a_c)
u_2'	Normalized value of u_2 (u_2/a_c)
v	Fluid velocity component in the y-direction
v_2	Vertical velocity component behind shock wave
v_2'	Normalized value of v_2 (v_2/a_c)
w	Spherical abberation parameter (Equation (5-3))
w'	Working variable (Equations (3-7) and (3-10))
x	Cartesian coordinate
x'	Cartesian coordinate
y	Cartesian coordinate
y'	Cartesian coordinate
z	Cartesian coordinate
z'	Cartesian coordinate
Δ	Optical-wave phase
Δ'	Optical-wave phase in terms of normalized coordinates ζ and η
Δ_1	Optical-wave phase for System 1
Δ_2	Optical-wave phase for System 2
Δ_D	Optical-wave phase for defocused system
ΔP	Variation of pressure from its mean $(P-\bar{P})$
Δn	Refractive index change across shock wave (n_2-n_1)
Δ_ρ	Variation of density from its mean $(\rho-\bar{\rho})$
Δ_ρ	Density change across a shock wave $(\rho_2-\rho_1)$
$\Delta\phi$	Refraction angle for a beam crossing a shock wave
Σ	Aperture area or beam cross-section area
Σ_1	Aperture area or beam cross-section area for System 1
Σ_2	Aperture area or beam cross-section area for System 2

Φ	Covariance function of wave phase Δ
α	The dc component of pow
β	The ac amplitude of pow
β	Shock wave angle
γ	Ratio of specific heats (c_p/c_v)
δ	Delta function
δ	Boundary layer thickness
$\delta*$	Boundary layer displacement thickness
ζ	Cartesian coordinate x normalized by sphere radius
η	Cartesian coordinate y normalized by sphere radius
θ	Polar coordinate (Equations (3-15), (3-18), and (3-19))
θ	Ramp angle in plane oblique shock wave problem
θ_{max}	Maximum ramp angle capable of producing a plane oblique shock wave
θ_0	Angle between polar axis (direction pointing into flow) and direction of propagation
κ	Coefficient of thermal conductivity
λ	Optical wavelength
λ_1	Optical wavelength in System 1
λ_2	Optical wavelength in System 2
μ	Variation of refractive index from its mean $(n-\bar{n})$
μ	Coefficient of viscosity
μ_∞	Freestream coefficient of viscosity
ν	Spatial frequency
ν_0	Spatial frequency at which OTF vanishes
ν_x	Spatial frequency in the x-direction
ν_y	Spatial frequency in the y-direction
ν_{max}	System resolution
ν_D	System resolution with diffraction OTF and nonzero TM
ν_L	Resolution corresponding to τ_L
ν''_{max}	Resolution corresponding to τ''
ν''_L	Resolution corresponding to τ_L''
ξ	Cartesian coordinate z normalized by sphere radius
ρ	Density
ρ_0	Stagnation or reservoir density
ρ_1	Density ahead of shock wave

ρ_1	Density for System 1
ρ_2	Density behind shock wave
ρ_2	Density for System 2
ρ_∞	Freestream density
$\rho_{\infty 1}$	Freestream density for System 1
$\rho_{\infty 2}$	Freestream density for System 2
σ	Standard deviation of wave phase Δ
σ^2	Variance of wave phase Δ (Square of σ)
τ	Optical transfer function (OTF)
τ_0	Diffraction-limit OTF
τ_1	OTF for System 1
τ_2	OTF for System 2
τ_{01}	Diffraction-limit OTF for System 1
τ_{02}	Diffraction-limit OTF for System 2
τ_C	OTF for controlled wavefront aberrations
τ_L	OTF of system with no boundary-flow effect
τ_R	*OTF degradation caused by random wavefront aberration* (τ/τ_C)
τ_{R2}	Measured value of τ_R for double pass through boundary layer in Kelsall tes
τ''	Linear OTF with same NCPD as τ
τ_L''	Linear OTF with same NCPD as τ_L
τ_{min}	Minimum value of τ_R
ϕ	Phase factor
ϕ	Angle between beam crossing a shock wave and the normal to the shock wave
ψ	Normalized radial coordinate ($\sqrt{\zeta^2 + \eta^2 + \xi^2}$)
ω	Angular frequency of optical wave ($2\pi c/\lambda$)
ω_p	Angular frequency of relative phase of the two wavefronts in a shearing interferometer

Important Equations

All units are MKS unless otherwise noted. Optical scaling rules are listed in Figure 57.

Relationships Between the Aerodynamics Parameters ρ, P, T, γ, and a (Speed of Sound).

$$P = 287\ \rho\ T \qquad (2\text{-}3)$$

$$\gamma = 1.4$$

$$a = \sqrt{\frac{\gamma P}{\rho}} = \sqrt{287\gamma T} \qquad (2\text{-}53)$$

Relationships Between Δ, n, K, and ρ.

$$n = 1 + K\rho \qquad (2\text{-}5)$$

$$K = 0.223 \times 10^{-3}\left(1 + \frac{7.52 \times 10^{-15}}{\lambda^2}\right) n^3/\text{kg} \qquad (2$$ [illegible]

$$K \approx 0.223 \times 10^{-3} \qquad (2\text{-}7)$$

$$\Delta(x,y) = \int_0^L n(x,y,z)\, dz \pm m\lambda \qquad (2\text{-}13)$$

If Δ is normalized according to $\Delta(0,0) = 0$, then the equation for Δ is

$$\Delta(x,y) = \int_0^L [n(x\ ,y,z) - n(0,0,z)]\, dz. \qquad (3\text{-}2)$$

Likewise,

$$\Delta(x,y) = \int_0^L [n(x,y,z) - \overline{n}]\, dz = \int_0^L \mu(x,y,z)\, dz \qquad (E\text{-}5)$$

is used if Δ is normalized according to $\overline{\Delta(x,y)} = 0$.

Relationships Between the Optics Functions Δ, I, τ, and NCPD.

$$\tau\left(\frac{x}{\lambda f},\frac{y}{\lambda f}\right) = \frac{1}{\Sigma}\iint_{-\infty}^{\infty} G_0(x',y')G_0(x'+x,y'+y) \times \exp\{i[\Delta(x'+x,y'+y) - \Delta(x',y')]\}\, dx'\, dy' \tag{2-28}$$

$$G_0(x,y) = \begin{cases} 1, (x,y) \in \Sigma \\ 0, (x,y) \notin \Sigma \end{cases} \tag{2-29}$$

$$\tau\left(\frac{x}{\lambda f},\frac{y}{\lambda f}\right) = \frac{1}{C}\iint_{-\infty}^{\infty} I(X,Y)\ \exp\left[\frac{ik}{f}\ (xX + yY)\right]\ dX\ dY \tag{2-21}$$

$$I(X,Y) = \frac{C}{(\lambda f)^2}\iint_{-\infty}^{\infty} \tau\left(\frac{x}{\lambda f},\frac{y}{\lambda f}\right)\exp\left[-\frac{ik}{f}(xX + yY)\right]\ dx\ dy \tag{2-43}$$

$$I_0(0,0) = \frac{C\Sigma}{(\lambda f)^2} \tag{2-48}$$

$$C = A^*A\Sigma = \iint_{-\infty}^{\infty} I(X,Y)\ dX\ dY \tag{2-22),(2-23}$$

$$\text{NCPD} = \frac{1}{\Sigma}\iint_{-\infty}^{\infty} \tau\left(\frac{x}{\lambda f},\frac{y}{\lambda f}\right)\ dx\ dy \tag{2-49}$$

$$\text{NCPD} = \frac{1}{\Sigma^2}\left|\iint_{-\infty}^{\infty} G_0(x,y)e^{ik\Delta(x,y)}\ dx\ dy\ \right|^2 \tag{2-51}$$

The following equations apply to systems with rotational symmetry.

$$\text{NCPD} = \frac{8}{D^2}\int_0^D \tau\left(\frac{r}{\lambda f}\right)\ r\ dr \tag{2-50}$$

$$\text{NCPD} = \frac{64}{D^4}\left|\int_0^{D/2} e^{ik\Delta(r)}\ r\ dr\right|^2 \tag{2-52}$$

If

$$\Delta(r) = \Delta_D(r) = wr^2, \tag{5-3}$$

then

$$\mathrm{NCPD} = \frac{2[1 - \cos(kwD^2/4)]}{(kwD^2/4)^2}. \tag{5-5}$$

Wave-Phase Equations for Subsonic Main Flow.

$$\Delta(x,y) = H\int_0^L \frac{1 - w'(x,y,z)}{1 + w'(x,y,z)} - \frac{1 - w'(0,0,z)}{1 + w'(0,0,z)}\, dz \tag{3-7}$$

$$H = K\,\rho_\infty \left(1 + \frac{\gamma-1}{2} M_\infty^2\right)^{\frac{1}{\gamma-1}} \tag{3-8}$$

$$w'(x,y,z) = \frac{V^2(x,y,z)/a_\infty^{\,2}}{2(\gamma-1)M_\infty^{\,2} + 4} \tag{3-10}$$

The following equations apply to a sphere of radius R.

$$\zeta = x/R \quad \eta = y/R \quad \xi = z/R \tag{3-13}$$

$$\Psi = \zeta^2 + \eta^2 + \xi^2 \qquad \ell = L/R \tag{3-14}$$

$$\Delta(x,y) = \Delta'(\zeta,\eta) = K\rho_\infty R c_2 \int_0^\ell \frac{c_1 - q(\theta,\psi)}{c_1 + q(\theta,\psi)} - \frac{c_1 - q\ (\theta_0,\xi)}{c_1 + q\ (\theta_0,\xi)}\, d\xi \tag{3-15}$$

$$c_1 = [2(\gamma-1)M_\infty^{\,2} + 4]/M_\infty^{\,2} \tag{3-16}$$

$$c_2 = \left(1 + \frac{\gamma-1}{2} M_\infty^{\,2}\right)^{\frac{1}{\gamma-1}} \tag{3-17}$$

$$q(\theta,\psi) = 1 + (1 - 3\cos^2\theta)/\psi^3 + 1/4(1 + 3\cos^2\theta)/\psi^6 \tag{3-18}$$

$$\cos\theta = (\xi\cos\theta_0 - \eta\sin\theta_0)/\psi \tag{3-19}$$

Diffraction Angle for a Beam Crossing a Plane Shock Wave.

$$\Delta\phi = -2K\rho_1 \frac{M_\infty^2 \sin^2\beta - 1}{(\gamma-1)M_\infty^2 \sin^2\beta + 2} \tan\phi \tag{3-39}$$

Equation for $\overline{\tau}$, σ^2, and a for Random Flow.

$$\overline{\tau}\left(\frac{x}{\lambda f},\frac{y}{\lambda f}\right) = \tau_0\left(\frac{x}{\lambda f}\ \frac{y}{\lambda f}\right)\overline{\tau}_R\left(\frac{x}{\lambda f}\ \frac{y}{\lambda f}\right) \tag{4-9}$$

$$\overline{\tau}_R\left(\frac{x}{\lambda f},\frac{y}{\lambda f}\right) = \overline{\tau}_R\ \left(\frac{r}{\lambda f}\right) = \exp\{-k^2\sigma^2[1-e^{-(r/a)^2}]\} \tag{4-16}$$

For a TBL

$$\sigma^2 = 4.4 \times 10^{-12}\delta^2{\rho_\infty}^2{M_\infty}^2 \tag{4-52}$$

$$a = 0.08\delta \tag{4-50}$$

For a TBL on a flat plate

$$\sigma^2 = 4.04 \times 10^{-16}{\rho_\infty}^{12/7}{T_\infty}^{1/14}{M_\infty}^{26/7}X^{12/7} \tag{4-53}$$

$$a = 7.66 \times 10^{-4}{\rho_\infty}^{-1/7}{T_\infty}^{1/28}{M_\infty}^{-1/7}X^{6/7} \tag{4-54}$$

For a separated flow

$$\sigma^2 = 1.2 \text{ X } 10^{-12}\rho_\infty L \tag{4-76}$$

$$a = 0.067L \tag{4-77}$$

For a wake flow behind a sphere of radius R

$$\sigma^2 = 1.2 \text{ X } 10^{-12}\rho_\infty R\left(\frac{1}{\sin\theta_0} - 1\right) \tag{5-10}$$

$$a = 0.067R \tag{5-8}$$

Equations for Imaging Systems.

$$\nu_x = \frac{x}{\lambda f} \qquad \nu_y = \frac{y}{\lambda f} \tag{2-25}$$

$$\nu = \frac{r}{\lambda f} \tag{4-18}$$

Threshold modulation model

$$TM(\nu) = b_0 + b_1 \nu^2 \qquad (4\text{-}63)$$

For Kodak 3414 film

$$TM(\nu) = 0.3 + 3.22 \times 10^{-6} \nu^2 \qquad (4\text{-}65)$$

where ν is in mm^{-1} or lines/mm.

Resolution condition

$$TM(\nu_{max}) = C_0 |\tau(\nu_{max})| \qquad (4\text{-}60)$$

Resolution approximation

$$\frac{\nu_{max}}{\nu_L} \approx \sqrt{\frac{NCPD}{NCPD_L}} \qquad (5\text{-}21)$$

Relationships between system resolution, angular resolution and ground resolution

$$AR = \frac{1}{f_{\nu_{max}}} \qquad (5\text{-}25)$$

$$GR = SR \cdot AR = \frac{SR}{f_{\nu_{max}}} \qquad (5\text{-}26)$$

For an idealized system in which $TM(\nu)$ vanishes and $\tau(\nu)$ is diffraction limited.

$$\nu_{max} = \frac{D}{\lambda f} \qquad (5\text{-}14)$$

$$AR = \frac{\lambda}{D} \qquad (5\text{-}27)$$

$$GR = SR \frac{\lambda}{D} \qquad (5\text{-}28)$$

Appendix B

Derivation of $\Delta(x,y)$ for the Main-Flow Sphere Problem

Equations (3-7) through (3-11) give the general solution for $\Delta(x,y)$.

$$\Delta(x,y) = H\int_0^L \frac{1 - w'(x,y,z)}{1 + w'(x,y,z)} - \frac{1 - w'(0,0,z)}{1 + w'(0,0,z)}\, dz \qquad \text{(B-1)}$$

$$H = K\rho_\infty\left(1 + \frac{\gamma-1}{2} M_\infty^2\right)^{\frac{1}{\gamma-1}} \qquad \text{(B-2)}$$

$$M_\infty = U/a_\infty \qquad \text{(B-3)}$$

$$w'(x,y,z) = \frac{V^2(x,y,z)/a_\infty^2}{2(\gamma-1)M_\infty^2 + 4} \qquad \text{(B-4)}$$

$$V^2(x,y,z) < a_\infty^2 \qquad \text{(B-5)}$$

The purpose of this appendix is to find V for a sphere (of radius R from which $\Delta(x,y)$ may then be found. The problem geometry is shown in Figure 15. The quantity V is the air velocity calculated from potential flow theory.

The velocity potential Ψ must satisfy the Laplace equation,

$$\nabla^2\Psi = 0, \qquad \text{(B-6)}$$

and the problem boundary conditions. The velocity V is the gradient of Ψ. The radial and polar velocity components, V_r and V_θ respectively, are given in terms of Ψ by

$$V_r = \frac{\delta\Psi}{\delta r} \qquad \text{(B-7)}$$

and

$$V_\theta = \frac{1}{r}\frac{\delta\Psi}{\delta\theta}. \qquad \text{(B-8)}$$

From the symmetry of the problem geometry the azimuthal component V_ϕ is zero. The boundary conditions are as follows.

1. For r >> R

$$V_r = -U\cos\theta \qquad V_\theta = U\sin\theta \tag{B-9}$$

2. For r = R

$$V_r = 0$$

For our problem ($V_\phi = 0$) Equation (B-6) becomes

$$\frac{1}{r^2}\frac{\delta}{\delta r}\left(r^2\frac{\delta\Psi}{\delta r}\right) + \frac{1}{r^2\sin\theta}\frac{\delta}{\delta\theta}\left(\sin\theta\,\frac{\delta\Psi}{\delta\theta}\right) = 0. \tag{B-11}$$

An expression for Ψ is needed such that the boundary conditions and Equation (B-11) are satisfied. Such an expression is

$$\Psi = -U\left(r + \frac{R^3}{2r^2}\right)\cos\theta. \tag{B-12}$$

The velocity components are

$$V_r = -U(1 - R^3/r^3)\cos\theta \tag{B-13}$$

and

$$V_\theta = U\left(1 + \frac{R^3}{2r^3}\right)\sin\theta. \tag{B-14}$$

In order to calculate the integral in Equation (B-1), the coordinates r and θ must be related to the coordinates x, y and z in Figure 15.

$$r^2 = x^2 + y^2 + z^2 \tag{B-15}$$

An expression for θ in terms of x, y and z is found by taking a vector from the sphere center to the point (x,y,z), and then expressing the projection of this vector on the polar axis in both coordinate systems. Equating the two expressions yields

$$r\cos\theta = z\cos\theta_0 - y\sin\theta_0. \tag{B-16}$$

For simplicity the following normalized coordinates are used throughout the rest of this appendix.

$$\zeta = x/R \quad \eta = y/R \quad \xi = z/R$$
$$\psi^2 = r^2/R^2 = \zeta^2 + \eta^2 + \xi^2 \quad \ell = L/R \tag{B-17}$$

The normalized velocity-square function, $q(\theta,\psi) = V^2/U^2$ becomes

$$q(\theta,\psi) = \frac{V_r^{\,2} + V_\theta^{\,2}}{U^2} = 1 + (1 - 3\cos^2\theta)/\psi^3 + 1/4(1 + 3\cos^2\theta)/\psi^6, \tag{B-18}$$

and Equation (B-16) may be written

$$\cos\theta = (\xi\cos\theta_0 - \eta\sin\theta_0)/\psi. \tag{B-19}$$

Equation (B-4) becomes

$$w'(x,y,z) = q(\theta/\psi)/c_1 \tag{B-20}$$

where

$$c_1 = [2(\gamma-1)M_\infty^{\,2} + 4]/M_\infty^{\,2}. \tag{B-21}$$

Finally Equation (B-1) becomes

$$\Delta(x,y) = \Delta'(\theta,\psi) = K\rho_\infty c_2 \int_1^\ell \frac{c_1 - q(\theta,\psi)}{c_1 + q(\theta,\psi)} - \frac{c_1 - q(\theta_0,\xi)}{c_1 + q(\theta_0,\xi)}\, d\xi \tag{B-22}$$

where

$$c_2 = \left(1 + \frac{\gamma-1}{2} M_\infty^{\,2}\right)^{\frac{1}{\gamma-1}} \tag{B-23}$$

Notice that the lower limit is now one instead of zero. It is assumed that the beam is plane parallel at $z = R$ or $\xi = 1$, and the integral between $\xi = 0$ and $\xi = 1$, therefore, vanishes.

To satisfy the Inequality (B-5),

$$M_\infty < \sqrt{1/q(\theta,\psi)} \tag{B-24}$$

must be satisfied for all $q(\theta,\psi)$, $0 \leq \theta \leq \pi$ and $\psi \geq 1$. Because q is symmetric about $\theta = \pi/2$, the limits on θ may be reduced to $0 \leq \theta \leq \pi/2$. It is necessary to find the upper limit of q. Suppose that the ψ^{-3} term in Equation (B-18) is non-positive. The maximum value of the ψ^{-3} term is zero, the maximum value of the ψ^{-6} term is one, and therefore q must be less than or equal to two. However, $q(\pi/2,1)$ is equal to 2 1/4. The ψ^{-3} term must, therefore, be positive when q is at its maximum. Since all terms in Equation (B-18) are positive, ψ must equal its minimum value of one for q to equal its maximum. The value of θ which maximizes q is found by differentiating $q(\theta,1)$ and setting it equal to zero.

$$\frac{dq(\theta,1)}{d\theta} = \frac{15}{2} \cos\theta \sin\theta = 0 \tag{B-25}$$

The pertinent solutions are $\theta = 0$ and $\theta = \pi/2$. If $\theta = 0$, however, the ψ^{-3} term is negative. The maximum value of $q(\theta,\psi)$ is, therefore, given by

$$\max[q(\theta,\psi)] = q(\pi/2,1) = 9/4. \tag{B-26}$$

The Inequality (B-24) becomes

$$M_\infty < \sqrt{1/q(\theta,\psi)} \leq \sqrt{1/q(\pi/2,1)} = \frac{2}{3}. \tag{B-27}$$

Appendix C

Derivation of the Density Change Across a Plane Oblique Shock Wave When the Shock-Wave Angle β is Known

Reference 11 gives the following conservation equations for flow across a plane oblique shock wave.

Mass

$$\rho_1 u_1 \sin\beta = \rho_2(u_2 \sin\beta - v_2 \cos\beta) \tag{C-1}$$

Momentum normal to shock wave

$$P_1 + \rho_1 u_1{}^2 \sin^2\beta = P_2 + \rho_2(u_2 \sin\beta - v_2 \cos\beta)^2 \tag{C-2}$$

Momentum parallel to shock wave

$$\rho_1 u_1{}^2 \sin\beta\cos\beta = \rho_2(u_2 \sin\beta - v_2 \cos\beta)(u_2 \cos\beta + v_2 \sin\beta) \tag{C-3}$$

Energy

$$1/2\ u_1{}^2 + \frac{\gamma}{\gamma-1}\frac{P_1}{\rho_1} = 1/2(u_2{}^2 + v_2{}^2) + \frac{\gamma}{\gamma-1}\frac{P_2}{\rho_2} \tag{C-4}$$

The symbols u, v, ρ, and P represent respectively the horizontal and vertical velocity components, density, and pressure. Subscripts 1 and 2 denote respectively values upstream and downstream of the shock wave. Equations (C-1) through (C-4) are a system of four equations with four unknowns, u_2, v_2, P_2, and ρ_2. The problem here is to find ρ_2. This task is accomplished by successively solving an equation for one of the unknowns (not ρ_2) and substituting the resulting expression into the remaining equations. The system is thus repeatedly reduced by one equation and one unknown until there is only one remaining equation with ρ_2 as the unknown.

First Equation (C-1) is solved for v_2.

$$v_2 = \tan\beta\ (u_2 - u_1\rho_1/\rho_2) \tag{C-5}$$

The following Equations are obtained by substituting the expression above into Equations (C-2) through (C-4).

$$P_1 + \rho_1 u_1{}^2 \sin^2\beta = P_2 + \sin^2\beta\ u_1{}^2 \rho_1{}^2/\rho_2 \tag{C-6}$$

$$u_1 \cos^2\beta = u_2 - \sin^2\beta\ u_1\rho_1/\rho_2 \tag{C-7}$$

$$u_1{}^2 - u_2 + \frac{2\gamma}{\gamma-1}\left(\frac{P_1}{\rho_1} - \frac{P_2}{\rho_2}\right) = \tan^2\beta \ (u_2 - u_1\rho_1/\rho_2)^2 \tag{C-8}$$

Equation (C-7) is solved for u_2.

$$u_2 = u_1(\cos^2\beta + \sin^2\beta \ \rho_1/\rho_2) \tag{C-9}$$

The system is reduced to two equations and two unknowns by substituting Equation (C-9) into Equation (C-8). Equation (C-6) is unchanged since it does not contain u_2.

$$u_1{}^2\sin^2\beta\left[\frac{\rho_1{}^2}{\rho_2{}^2} - 1\right] = \frac{2\gamma}{\gamma-1}\left(\frac{P_1}{\rho_1} - \frac{P_2}{\rho_2}\right) \tag{C-10}$$

The system now includes Equation (C-6) and (C-10). Equation (C-6) is solved for P_2.

$$P_2 = P_1 + \rho_1 u_1{}^2\sin^2\beta \ (1 - \frac{\rho_1}{\rho_2}) \tag{C-11}$$

Substituting Equation (C-11) into (C-10) yields

$$\begin{aligned}&\rho_2{}^2(\rho_1 u_1{}^2\sin^2\beta - \gamma\rho_1 u_1{}^2\sin^2\beta - 2\gamma P_1) + \\ &\rho_2(2\gamma\rho_1 P_1 + 2\gamma\rho_1{}^2 u_1{}^2\sin^2\beta) - \rho_1{}^3 u_1{}^2\sin^2\beta - \gamma\rho_1{}^3 u_1{}^2\sin^2\beta = 0.\end{aligned} \tag{C-12}$$

The two solutions to this quadratic equation are

$$\rho_2 = \rho_1 \tag{C-13}$$

and

$$\rho_2 = \rho_1 \frac{\rho_1 u_1{}^2\sin^2\beta \ (\gamma+1)}{2\gamma P_1 + \rho_1 u_1{}^2\sin^2\beta \ (\gamma-1)}. \tag{C-14}$$

Equation (C-13) is an extraneous solution. Since Mach number is given by

$$M_\infty{}^2 = u_1{}^2/a_\infty{}^2 = \frac{u_1^2 \ \rho_1}{\gamma P_1}, \tag{C-15}$$

Equation (C-14) may be written

$$\rho_2 = \rho_1 \frac{(\gamma+1)M_\infty^{\;2}\sin^2\beta}{(\gamma-1)M_\infty^{\;2}\sin^2\beta + 2} . \tag{C-16}$$

Equation (C-16) is the desired expression for ρ_2.

Appendix D

Derivation of the Average OTF for Random Wavefront Aberrations

Consider the wave phase $\Delta(x,y)$ given by

$$\Delta(x,y) = \Delta_C(x,y) + \Delta_R(x,y) \tag{D-1}$$

where Δ_C is time-invariant or controlled and Δ_R defines a spatially-stationary Gaussian random process. The purpose of this appendix is to find an expression for the expected value of the OTF corresponding to the wave phase Δ given by Equation (D-1).

From Equation (2-28) the OTF for the Δ of Equation (D-1) is given by

$$\begin{aligned}\tau\left(\frac{x}{\lambda f},\frac{y}{\lambda f}\right) = \frac{1}{\Sigma}\iint_{-\infty}^{\infty} & G_0(x',y')G_0(x'+x,y'+y)\\ & \times \exp\{ik[\Delta_C(x'+x,y'+y) - \Delta_C(x',y')]\}\\ & \times \exp\{ik[\Delta_R(x'+x,y'+y) - \Delta_R(x',y')]\}\, dx'\, dy'.\end{aligned} \tag{D-2}$$

Taking the expected value of both sides of Equation (D-2) yields

$$\begin{aligned}E\left[\tau\left(\frac{x}{\lambda f},\frac{y}{\lambda f}\right)\right] = \frac{1}{\Sigma}\iint_{-\infty}^{\infty} & G_0(x',y')G_0(x'+x,y'+y)\exp\{ik[\Delta_C(x'+x,y'+y) - \Delta_C(x',y')]\}\\ & \times E\left(\exp\{ik[\Delta_R(x'+x,y'+y) - \Delta_R(x',y')]\}\right)dx'\, dy'.\end{aligned} \tag{D-3}$$

Because Δ_R is spatially stationary the expected value in the right side of Equation (D-3) is a function of neither x' nor y' and may be extracted from the integral.

$$E\left[\tau\left(\frac{x}{\lambda f},\frac{y}{\lambda f}\right)\right] = \tau_C\left(\frac{x}{\lambda f},\frac{y}{\lambda f}\right)E\left(\exp\{ik[\Delta_R(x'+x,y'+y) - \Delta_R(x',y')]\}\right) \tag{D-4}$$

$$\begin{aligned}\tau_C\left(\frac{x}{\lambda f},\frac{y}{\lambda f}\right) = \frac{1}{\Sigma}\iint_{-\infty}^{\infty} & G_0(x',y')G_0(x'+x,y'+y)\\ & \times \exp\{ik[\Delta_C(x'+x,y'+y) - \Delta_C(x',y')]\}\, dx'\, dy'\end{aligned} \tag{D-5}$$

The OTF τ_C is the OTF which would be obtained if Δ were completely controlled. To simplify notation the following terms are introduced.

$$U = \Delta_R(x',y') \qquad V = \Delta_R(x'+x,y'+y) \tag{D-6}$$

Equation (D-4) becomes

$$E[\tau(\frac{x}{\lambda f},\frac{y}{\lambda f})] = \tau_C(\frac{x}{\lambda f},\frac{y}{\lambda f})E[e^{ik(V-U)}]. \qquad \text{(D-7)}$$

U and V are dependent random variables with a joint probability density function given by

$$f(\mu,v) = \frac{1}{2\pi\sigma_u\sigma_v\sqrt{1-\rho^2}} \exp\left\{-\frac{1}{2(1-\rho^2)}\left[\left(\frac{u-\mu_u}{\sigma_u}\right)^2 - 2\rho\,\frac{(u-\mu_u)(v-\mu_v)}{\sigma_u\sigma_v} + \left(\frac{v-\mu_v}{\sigma_v}\right)^2\right]\right\} \qquad \text{(D-8)}$$

where

$$\rho = [E(UV) - \mu_u\mu_v]/\sigma_u\sigma_v \qquad \text{(D-9)}$$

and where μ_u, μ_v, σ_u^2, and σ_v^2 are respectively the expected values of U and V and the variances of U and V. The bivariate normal density function given by Equation (D-8) is implied by the assumption that Δ_R defines a Guassian random process. The numerator of the right side of Equation (D-9) is the convariance function $\Phi(x,y)$. Since the process is spatially-stationary, $\Phi(x,y)$ is not a function of x' or y', the variances of U and V are equal, and the expected values of U and V are equal.

$$\sigma_u^2 = \sigma_v^2 = \sigma^2 \qquad \text{(D-10)}$$

$$\rho = \Phi(x,y)/\sigma^2 \qquad \text{(D-11)}$$

Without loss of generality it is assumed the mean wave phase is zero.

$$\mu_u = \mu_v = 0 \qquad \text{(D-12)}$$

Substituting Equations (D-10), (D-11), and (D-12) into Equation (D-8) yields

$$f(u,v) = \frac{1}{2\pi\sqrt{\sigma^4-\Phi^2}} \exp\left[-\frac{\sigma^2u^2-2\Phi uv+\sigma^2v^2}{2(\sigma^4-\Phi^2)}\right]. \qquad \text{(D-13)}$$

The expected value in the right side of Equation (D-7) may now be expressed as

$$E\left[e^{ik(V-U)}\right] = EX = \iint_{-\infty}^{\infty} e^{ik(v-u)} f(u,v)\; du\; dv \qquad \text{(D-14)}$$

or

$$EX = \frac{1}{2\pi\sqrt{\sigma^4-\Phi^2}} \iint_{-\infty}^{\infty} \exp\left[-\frac{\sigma^2u^2-2\Phi uv+\sigma^2v^2+2ik(\sigma^4-\Phi^2)(v-u)}{2(\sigma^4-\Phi^2)}\right] du\; dv. \qquad \text{(D-15)}$$

The term $[\phi v + ik(\sigma^4 - \Phi^2)]^2/\sigma^2$ is added and subtracted from the numerator to yield

$$EX = \frac{1}{2\pi\sqrt{\sigma^4-\Phi^2}} \iint_{-\infty}^{\infty} \exp\left\{-\frac{\sigma^2u^2-2[\Phi v+ik(\sigma^4-\Phi^2)]u+[\Phi v+ik(\sigma^4-\Phi^2)]^2/\sigma^2}{2\ (\sigma^4-\Phi^2)}\right\} du \tag{D-16}$$

$$x\ \exp\left\{-\frac{\sigma^2v^2+2ik(\sigma^4-\Phi^2)v-[\Phi v+ik(\sigma^4-\Phi^2)]^2/\sigma^2}{2(\sigma^4-\Phi^2)}\right\} dv$$

Notice that the numerator in the inner integral is a perfect square. With the variable substitution

$$W = \frac{\sigma u-[\Phi v+ik(\sigma^4-\Phi^2)]/\sigma}{\sqrt{2(\sigma^4-\Phi^2)}} \tag{D-17}$$

Equation (D-16) becomes

$$EX = \frac{1}{\sqrt{2\pi}\sigma} \int_{-\infty}^{\infty} e^{-W^2} dW \tag{D-18}$$

$$X \int_{-\infty}^{\infty} \exp\left\{-\frac{\sigma^2v^2+2ik(\sigma^4-\Phi^2)v-[\sigma v+ik(\sigma^4-\Phi^2)]^2/\sigma^2}{2(\sigma^4-\Phi^2)}\right\} dv.$$

The value of the first integral is $\sqrt{\pi}$ and the exponential term in the second integral may be simplified.

$$EX = \frac{1}{\sqrt{2\pi}\sigma} \int_{-\infty}^{\infty} e^{-[v^2+2ik(\sigma^2-\Phi)v]/2\sigma^2} dv\ e^{-k^2(\sigma^4-\Phi^2)/2\sigma^2} \tag{D-19}$$

With the variable substitution

$$Z = \frac{v+ik(\sigma^2-\Phi)}{\sqrt{2}\sigma} \tag{D-20}$$

Equation (D-19) becomes

$$EX = \frac{1}{\sqrt{\pi}} \int_{-\infty}^{\infty} e^{-Z^2} dZ\ \exp\left[-\frac{k^2(\sigma^2-\Phi)^2+k^2(\sigma^4-\Phi^2)}{2\sigma^2}\right] \tag{D-21}$$

or

$$EX = \exp[-k^2(\sigma^2-\Phi)]. \tag{D-22}$$

Finally Equations (D-22) and (D-14) are substituted into Equation (D-7).

$$E[\tau(\frac{x}{\lambda f},\frac{y}{\lambda f})] = \tau_C(\frac{x}{\lambda f},\frac{y}{\lambda f}) \exp\{-k^2[\sigma^2-\Phi(x,y)]\} \qquad \text{(D-23)}$$

Equation (D-23) is the desired expression for the expected value of the OTF.

Appendix E

Derivation of Equation for σ^2

The covariance function and variance of the spatially-stationary wave phase Δ are given respectively by

$$\Phi(x,y) = \overline{\Delta(x',y')\Delta(x'+x,y'+y)} \tag{E-1}$$

and

$$\sigma^2 = \Phi(0,0) = \overline{\Delta^2(x',y')}. \tag{E-2}$$

The average phase is defined to be zero, and it is assumed that refractive index changes in the optical path are small.

$$\overline{\Delta(x',y')} = 0 \tag{E-3}$$

$$n(x',y',z') - \overline{n} = \mu(x',y',z') << 1 \tag{E-4}$$

The above conditions imply that Δ is given by

$$\Delta(x',y') = \int_0^L \mu(x',y',z')\, dz'. \tag{E-5}$$

In this appendix expressions are derived for $\Phi(x,y)$ and σ^2. It is assumed that the refractive index variation μ has a Gaussian covariance function.

$$\overline{\mu(x',y',z')\mu(x'+x,y'+y,z'+z)} = \overline{\mu^2} \exp\left[-\left(\frac{x^2}{a_x^2} + \frac{y^2}{a_y^2} + \frac{z^2}{a_z^2}\right)\right] \tag{E-6}$$

From Equations (E-1) and (E-5) the covariance function Φ is given by

$$\Phi(x,y) = \overline{\int_0^L \mu(x',y',z')dz' \int_0^L \mu(x'+x,y'+y,z_2)dz_2} \tag{E-7}$$

or

$$\Phi(x,y) = \int_0^L\int_0^L \overline{\mu(x',y',z')\mu(x'+x,y'+y,z_2)}\,dz_2dz'. \tag{E-8}$$

With the variable substitution

$$z = z_2 - z' \tag{E-9}$$

Equation (E-8) becomes

$$\Phi(x,y) = \int_0^L \int_{-z'}^{L-z'} \overline{\mu(x',y',z')\mu(x'+x,y'+y,z'+z)}\ dz\ dz'. \qquad \text{(E-10)}$$

Substituting Equation (E-6) into Equation (E-10) yields

$$\Phi(x,y) = \overline{\mu^2}\ \exp\left[-\left(\frac{x^2}{a_x^2} + \frac{y^2}{a_z^2}\right)\right]\int_0^L \int_{-z'}^{L-z'} \exp(-z^2/a_z^2)\ dz\ dz' \qquad \text{(E-11)}$$

or

$$\Phi(x,y) = I a_z^2\overline{\mu^2}\ \exp\left[-\left(\frac{x^2}{a_x^2} + \frac{y^2}{a_y^2}\right)\right] \qquad \text{(E-12)}$$

where I is defined by

$$I = \frac{1}{a_z^2}\int_0^L \int_{-z'}^{L-z'} \exp(-z^2/a_z^2)\ dz\ dz'. \qquad \text{(E-13)}$$

With the normalized variables

$$u = z/a_z \qquad v = z'/a_z \qquad w = L/a_z \qquad \text{(E-14)}$$

Equation (E-13) becomes

$$I = \int_0^w \int_{-v}^{w-v} e^{-u^2} du\ dv. \qquad \text{(E-15)}$$

To evaluate I, Equation (E-15) is expressed in terms of the error function, erf, and the error function complement, erfc. These functions are given by

$$\mathrm{erf}(v) = \frac{2}{\sqrt{\pi}}\int_0^v e^{-u^2} du = \frac{2}{\sqrt{\pi}}\int_{-v}^0 e^{-u^2} du \qquad \text{(E-16)}$$

$$\mathrm{erfc}(v) = 1 - \mathrm{erf}(v) = \frac{2}{\sqrt{\pi}}\int_v^\infty e^{-\mu^2} du = \frac{2}{\sqrt{\pi}}\int_{-\infty}^{-v} e^{-u^2} du \qquad \text{(E-17)}$$

$$\mathrm{erf}(0) = 1 - \mathrm{erfc}(\infty) = 0 \qquad \text{(E-18)}$$

$$\mathrm{erf}(\infty) = \mathrm{erfc}(0) = 1 \qquad \text{(E-19)}$$

The inner integral in Equation (E-15) may be written

$$\int_{-v}^{w-v} e^{-u^2} du = \int_{-\infty}^{0} e^{-u^2} du + \int_{0}^{\infty} e^{-u^2} du - \int_{w-v}^{\infty} e^{-u^2} du - \int_{-\infty}^{-v} e^{-u^2} du$$

$$= \frac{\sqrt{\pi}}{2} \left[2 - \mathrm{erfc}\,(w-v) - \mathrm{erf}(v)\right] \qquad \text{(E-20)}$$

Substituting Equation (E-20) into (E-15) yields

$$I = \frac{\sqrt{\pi}}{2}\ 2w - \int_{0}^{w} \mathrm{erfc}(w-v)\ dv - \int_{0}^{w} \mathrm{erfc}(v)\ dv$$

$$= \sqrt{\pi} \left[w - \int_{0}^{w} \mathrm{erfc}(v)\ dv\right]. \qquad \text{(E-21)}$$

The error function complement has the property[26]

$$\int_{w}^{\infty} \mathrm{erfc}(v) dv = \frac{2}{\sqrt{\pi}} \int_{w}^{\infty} (v-w) e^{-v^2} dv. \qquad \text{(E-22)}$$

Equation (E-21) becomes

$$I = \sqrt{\pi} w - 2\int_{0}^{\infty} v e^{-v^2} dv = 2\int_{w}^{\infty} (v-w) e^{-v^2} dv$$

$$= \sqrt{\pi} w - 1 + e^{-w^2} - \sqrt{\pi} w \int_{w}^{\infty} e^{-v^2} dv \qquad \text{(E-23)}$$

$$= \sqrt{\pi} w\ \mathrm{erf}(w) - 1 + e^{-w^2}.$$

Substituting Equations (E-14) and (E-23) into Equation (E-12) yields the general expression for Φ.

$$\Phi(x,y) = \left[\sqrt{\pi}\ (L/a_z)\mathrm{erf}(L/a_z) - 1 + e^{-(L/a_z)^2}\right] a_z^{2} \mu^2 \exp\left[-\left(\frac{x^2}{a_x^2} + \frac{y^2}{a_y^2}\right)\right] \qquad \text{(E-24)}$$

If $a_z \ll L$, then Equation (E-24) becomes

$$\Phi(x,y) = \sqrt{\pi}\, a_z\, L\, \overline{\mu^2} \exp\left[-\left(\frac{x^2}{a_x^{\,2}} + \frac{y^2}{a_y^{\,2}}\right)\right]. \qquad \text{(E-25)}$$

Finally, if μ is isotropic, then the a's are all equal,

$$a_x = a_y = a_z = a, \qquad \text{(E-26)}$$

and the covariance function and variance of Δ are given respectively by

$$\Phi(x,y) = \sqrt{\pi}\, a\, L\, \mu^2 \exp[-(x^2 + y^2)/a^2] \qquad \text{(E-27)}$$

and

$$\sigma^2 = \sqrt{\pi}\, a\, L\, \overline{\mu^2}. \qquad \text{(E-28)}$$

Appendix F

Derivation of $\overline{Q}$ for the Stine-Winovich Experiment

The purpose of this appendix is to find the average theoretical ratio $\overline{Q}$ of the radiant power emerging from the collection aperture to that emerging from the source aperture for the Stine-Winovich experiment.

From the problem geometry and the assumption of an isotropic boundary layer disturbance both the radiant emittance of the source aperture $O(r)$ and the image irradiance $I(R)$ are rotationally symmetric. The ratio $\overline{Q}$ is therefore given by

$$\overline{Q} = \frac{2\pi \int_0^{r_b} \overline{I}(R)\ R\ dR}{2\pi \int_0^{r_a} O(r)\ r\ dr}. \qquad \text{(F-1)}$$

It is assumed that $O(r)$ is constant over the source aperture, and for simplicity the total radiant power through the source aperture is taken to be unity. $O(r)$ and $\overline{Q}$ are, therefore, given respectively by

$$O(r) = \begin{cases} \dfrac{1}{\pi r_a^2}, & 0 \leq r \leq r_a \\ 0 \text{ otherwise} \end{cases} \qquad \text{(F-2)}$$

and

$$\overline{Q} = 2\pi \int_0^{r_b} \overline{I}(R)\ R\ dR. \qquad \text{(F-3)}$$

In the spatial-frequency domain $I(R)$ and $O(r)$ are related by

$$S_i(\nu) = S_o(\nu)\tau(\nu) \qquad \text{(F-4)}$$

where S_i and S_o are the Fourier transforms of I and O respectively and τ is the system OTF. Since the system is rotationally symmetric, S_i, S_o, and τ are all real. The Fourier transform pairs I, S_i, and O, S_o have the following relationships.

$$I(R) = 2\pi \int_0^{\infty} S_i(\nu) J_0(2\pi\nu R)\ \nu\ d\nu \qquad \text{(F-5)}$$

$$S_0(\nu) = 2\pi \int_0^{\infty} O(r) J_0(2\pi\nu r)\ r\ dr$$

$$= \frac{2}{r_a^{2}} \int_0^{r_a} J_0(2\pi\nu r)\ r\ dr \qquad \text{(F-6)}$$

The following equation is obtained by substituting Equations (F-4), (F-5), and (F-6) into Equation (F-3).

$$\overline{Q} = \frac{8\ ^{2}}{r_a^{2}} \int_0^{r_b}\int_0^{\infty}\int_0^{r_a} J_0(2\pi\nu r)\ r\ dr\ \overline{\tau}(\nu) J_0(2\pi\nu R)\ \nu\ d\nu\ R\ dR \qquad \text{(F-7)}$$

By changing the order of integration, Equation (F-7) may be written

$$\overline{Q} = \frac{8\pi^{2}}{r_a^{2}} \int_0^{\infty}\int_0^{r_b} J_0(2\pi\nu R)\ R\ dR \int_0^{r_a} J_0(2\pi\nu r)\ r\ dr\ \overline{\tau}(\nu)\ \nu\ d\nu \qquad \text{(F-8)}$$

Bessel functions have the property[27]

$$\frac{1}{x}\frac{d}{dx}\left[xJ_1(x)\right] = J_0(x). \qquad \text{(F-9)}$$

In integral form Equation (F-9) may be written

$$\int_0^{x} rJ_0(r)dr = xJ_1(x). \qquad \text{(F-10)}$$

With the formula above, Equation (F-8) becomes

$$\overline{Q} = \frac{2r_a}{r_b}\int_0^{\infty} \frac{\overline{\tau}(\nu)}{\nu}\ J_1(2\pi\nu r_b)\ J_1(2\pi\nu r_a)\ d\nu. \qquad \text{(F-11)}$$

The upper limit of the integral may be changed to $D/\lambda f$ since

$$\tau(\nu) = \tau\left(\frac{r}{\lambda f}\right) = 0,\ r > D \qquad \text{(F-12)}$$

where D is the telescope diameter.

With the variable substitution

$$u = 2\pi\nu r_b \qquad \text{(F-13)}$$

Equation (F-11) becomes

$$\overline{Q} = \int_0^{\frac{2\pi D r_b}{\lambda f}} \overline{\tau}\left(\frac{u}{2\pi r_b}\right) J_1(u) \frac{2J_1\left(u\frac{r_a}{r_b}\right)}{u\frac{r_a}{r_b}}\, du. \tag{F-14}$$

The average OTF $\overline{\tau}$ is now examined. In terms of its random and diffraction-limit components τ is given by

$$\overline{\tau}\left(\frac{r}{\lambda f}\right) = \overline{\tau}_{R2}\left(\frac{r}{\lambda f}\right)\tau_0\left(\frac{r}{\lambda f}\right) \tag{F-15}$$

where a "2" is included in the subscript of $\overline{\tau}_R$ to indicate that two TBL's are crossed by the optical beams. It is assumed that the two TBL's are independent but statistically identical. The random optical phase for a beam crossing both TBL's is given by

$$\Delta_{R2} = \Delta_{Ra} + \Delta_{Rb} \tag{F-16}$$

where Δ_{Ra} and Δ_{Rb} are the random phases caused by the first and second TBL's respectively. Since Δ_{Ra} and Δ_{Rb} are independent Gaussian random variables, the variance of Δ_{R2} is equal to the sum of the variances of Δ_{Ra} and Δ_{Rb}. If the variances of Δ_{Ra} and Δ_{Rb} are equal to σ^2, then the variance of Δ_{R2} is given by

$$\sigma_2{}^2 = \sigma^2 + \sigma^2 = 2\sigma^2 \tag{F-17}$$

The equation for $\overline{\tau}_{R2}$ is therefore

$$\overline{\tau}_{R2}\left(\frac{r}{\lambda f}\right) = \exp\{-2k^2\sigma^2[1-e^{-(r/a)^2}]\} = \left[\overline{\tau}_R\left(\frac{r}{\lambda f}\right)\right]^2 \tag{F-18}$$

where $\overline{\tau}_R$ is the random OTF for a beam crossing only one TBL. Substituting Equation (F-15) and (F-18) into Equation (F-14) leads to the final expression for $\overline{Q}$.

$$\overline{Q} = \int_0^{\frac{2\pi D r_b}{\lambda f}} \tau_0\left(\frac{u}{2\pi r_b}\right)\left[\overline{\tau}_R\left(\frac{u}{2\pi r_b}\right)\right]^2 J_1(u) \frac{2J_1\left(u\frac{r_a}{r_b}\right)}{u\frac{r_a}{r_b}}\, du \tag{F-19}$$

Appendix G

Derivation of the Radiant Output Power of a Shearing Interferometer as a Function of the MTF

Figure 58 shows the superimposed beams for a shearing interferometer. It is assumed that the beams are monochromatic and perfectly coherent. The beam Σ is displaced from the beam Σ_1 by (x,y), and the relative phase of the two beams is Λ In general Λ is a function of either (x,y) or time t or both depending on the interferometer design.

The pupil functions for Σ and Σ_1 are given respectively by

$$G(x',y') = \begin{cases} Ae^{ik\Delta(x',y')}, & (x',y')\epsilon\Sigma \\ 0 \text{ otherwise} \end{cases} \tag{G-1}$$

and

$$G_1(x',y') = \begin{cases} Ae^{ik[\Delta(x'+x,\, y'+y)+\Lambda]}, & (x',y')\epsilon\Sigma_1 \\ 0 \text{ otherwise.} \end{cases} \tag{G-2}$$

Since the condition $(x',y')\epsilon\Sigma_1$ implies the condition $(x'+x, y'+y)\epsilon\Sigma$, the pupil function G_1 may be written

$$G_1(x',y') = G(x'+x,\, y'+y)e^{ik\Lambda} \,. \tag{G-3}$$

The pupil function for the interferometer output G_2 is the sum of G and G_1,

$$G_2(x',y') = G(x',y') + G_1(x',y') \tag{G-4}$$

or

$$G_2(x',y') = G(x',y') + G(x'+x, y'+y)e^{ik\Lambda}. \tag{G-5}$$

The radiant power density of the interferometer output is

$$I(x',y') = G_2^*(x',y')G_2(x',y') \tag{G-6}$$

From Equation (G-5) Equation (G-6) becomes

$$\begin{aligned} I(x',y') = {} & G^*(x',y')G(x',y') + G^*(x'+x,y'+y)G(x'+x,y'+y) \\ & + G^*(x',y')G(x'+x,y'+y)e^{ik\Lambda} + G^*(x'+x,y'+y)G(x',y')e^{-ik\Lambda}. \end{aligned} \tag{G-7}$$

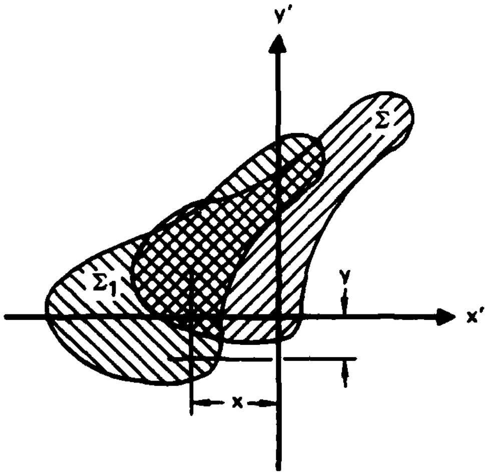

FIGURE 58
CROSS SECTION OF SUPERIMPOSED BEAMS FOR A SHEARING INTERFEROMETER

GP74-0200-61

The total radiant output power is found by integrating I(x′,y′) over all space.

$$\text{pow} = \iint_{-\infty}^{\infty} I(x',y')\ dx'dy' \tag{G-8}$$

Upon substitution of Equations (G-1) and (G-7) Equation (G-8) becomes

$$\text{pow} = 2\Sigma A^{*}A + 2\text{Re}\left[e^{ik\Lambda} \iint_{-\infty}^{\infty} G^{*}(x',y')G(x'+x,y'+y)\,dx'dy'\right] \tag{G-9}$$

where Re denotes "the real part of." Equations (2-24) and (2-27) imply that Equation (G-9) may be written

$$\text{pow} = 2\Sigma A^{*}A\left\{1 + \text{Re}\left[\tau\left(\frac{x}{\lambda f},\frac{y}{\lambda f}\right)e^{ik\Lambda}\right]\right\}. \tag{G-10}$$

Denoting the phase of τ by $\Omega(x,y)$,

$$\tau\left(\frac{x}{\lambda f},\frac{y}{\lambda f}\right) = \left|\tau\left(\frac{x}{\lambda f},\frac{y}{\lambda f}\right)\right| e^{i\Omega(x,y)} \tag{G-11}$$

Equation (G-10) becomes

$$\text{pow} = 2\Sigma A^{*}A\left\{1 + \left|\tau\left(\frac{x}{\lambda f},\frac{y}{\lambda f}\right)\right| \cos[\Omega(x,y)+k\Lambda]\right\}. \tag{G-12}$$

In a real system finite bandwidth, inequality of power of the two beams, and partial incoherence of the beams prevent Equation (G-12) from being realized. It can be shown, however, that even with the error sources mentioned above, pow is still directly proportional to the amplitude of the cosine term. Equation (G-12) is modified to

$$\text{pow} = \alpha + \beta\left|\tau\left(\frac{x}{\lambda f},\frac{y}{\lambda f}\right)\right| \cos[\phi_i+\Omega(x,y) + k\Lambda] \tag{G-13}$$

where α and β are constants ($\beta<\alpha$), and ϕ_i is the phase change caused by partial incoherence.

For the corner-cube design the phase term $k\Lambda$ is directly proportional to time. With the x-axis as the direction of shear, Equation (G-13) becomes

$$\text{pow} = \alpha + \beta\left|\tau\left(\frac{x}{\lambda f},0\right)\right| \cos[\phi(x) + \omega_p t] \tag{G-14}$$

where

$$\phi(x) = \phi_i + \Omega(x,0) \tag{G-15}$$

and ω_p is the angular frequency of the relative phase of the two beams.

References

1. Private Communication, D. Groening, Avionics Laboratory, Wright-Patterson Air Force Base, Dayton, Ohio.

2. Fisher, Ralph W., "RF-4C Modernization Flight Test Program," McDonnell Aircraft Company Report No. G493, 15 May 1969, CONFIDENTIAL, Control No. C-200996.

3. Mazurowski, M. J., Cornell Aeronautical Laboratory, Inc., "A Wind Tunnel Investigation of the Performance of RF-4C Optical Sensors," AFAL-TR-70-176, Air Force Avionics Laboratory, Wright-Patterson Air Force Base, Ohio, October 1970.

4. Probst, G. B. and D. J. Wolters, "RF-4C Refaired Nose Program Technical Report Vol II Analysis and Evaluation of Camera Performance," MDC A1469, McDonnell Aircraft Company, St. Louis, 29 September 1972.

5. Stine, H. A. and W. Winovich, Ames Aeronautical Laboratory, "Light Diffusion Through High Speed Turbulent Boundary Layers," NACA RM A56B21, National Advisory Committee for Aeronautics, Washington, May 1956.

6. Kelsall, D., "Interferometric Imaging Techniques," Optics Research (1972:1), ESD-TR-72-195, Lincoln Laboratory, Massachusetts Institute of Technology, Lexington, Massachusetts, December 1972, pp 62-68.

7. Campen, C. F., R. M. Cunningham, and V. G. Plank, "Electromagnetic Wave Propagation in the Lower Atmosphere," Handbook of Geophysics for Air Force Designers, Chapter 13, Section 1, Air Force Cambridge Research Center, 1957.

8. O'Neill, E. L., Introduction to Statistical Optics, Addison-Wesley Publishing Company, Inc., Reading Massachusetts, 1963.

9. Oswatitsch, K. and G. Kuerti, Gas Dynamics, Academic Press Inc., New York, 1956.

10. Houghton, E. L. and R. P. Boswell, Further Aerodynamics for Engineering Students, St. Martin's Press, New York, 1969.

11. Liepmann, H. W. and A. E. Puckett, Introduction to Aerodynamics of a Compressible Fluid, John Wiley and Sons, Inc., New York, 1947.

12. Taylor, G. I. and J. W. Maccoll, "The Mechanics of Compressible Fluids", Aerodynamic Theory, Vol III, W. F. Durand, ed., Guggenheim Fund for the Promotion of Aerodynamics, 1934.

13. Barakat, R., "The Influences of Random Wavefront Errors on the Imaging Characteristics of an Optical System," Optica Acta, 18, 9, 1971 pp 683-694.

14. Chernov, L. A., Wave Propagation in a Random Medium, translated by R. A. Silverman, Dover Publications, Inc., New York, 1967.

15. Tatarski, V. I., Wave Propagation in a Turbulent Medium, translated by R. A. Silverman, Dover Publications, Inc., New York, 1967.

16. Falkner, V. M., "A New Law for Calculating Drag - The Resistance of a Smooth Flat Plate with Turbulent Bounding Layer," Aircraft Engineering, 15, March 1943, pp 65-69.

17. Lyon, R. H., Bolt Beranek and Newman Inc., Random Noise and Vibration in Space Vehicles, The Shock and Vibration Information Center, U.S. Department of Defence, Washington, D.C., 1967.

18. Lauroesch, T. J., G. G. Fulmer, J. R. Edinger, G. T. Keene, and T. F. Kerwick, "Threshold Modulation Curves for Photographic Films," Appl. Opt., 9, 4, April 1970, pp 875-887.

19. "Kodak Data for Aerial Photography," 3rd ed., Eastman Kodak Company Rochester, New York, 1971.

20. Minzner, R. A. and W. S. Ripley, "Model Atmospheres," Handbook of Geophysics for Air Force Designers, Chapter 1, Section 2, Air Force Cambridge Research Center, 1957.

21. Hopkins, H. H., "Interferometric Methods for the Study of Diffraction Images," Optica Acta, 2, 1, April 1955, pp 23-29.

22. Kelsall, D., "Optical Frequency Response Characteristics in the Presence of Spherical Aberation Measured by an Automatically Recording Interferometric Instrument," Proc. Phys. Soc., 73, 3, March 1959, pp 465-479.

23. Kelsall, D., "Interferometric Techniques for Image Evaluation," Optics Research (1970:3), ESD-TR-70-417, Lincoln Laboratory, Massachusetts Institute of Technology, Lexington, Massachusetts, March 1971, pp 35-38.

24. Private Communication, D. Kelsall, Lincoln Laboratory, Massachusetts Institute of Technology, Lexington, Massachusetts.

25. Kelsall, D., "Rapid Interferometric Technique for MTF Measurements in the Visible or Infrared Region," Applied Optics, 12, 7, July 1973, pp 1398-1399.

26. Gautschi, W., "Error Function and Fresnel Integrals," Handbook of Mathematical Functions with Formulas, Graphs and Mathematical Tables, Chapter 7, National Bureau of Standards, June 1964.

27. Oliver, F. W. J., "Bessel Functions of Integer Order," Handbook of Mathematical Functions with Formulas, Graphs, and Mathematical Tables, Chapter 9, National Bureau of Standards, June 1964.

END

DATE
FILMED

1 83

DTIC